FZD-532

Terahertz studies on semiconductor quantum heterostructures in the low and high field regime

Martin Wagner

April 2010

Wissenschaftlich-Technische Berichte
FZD-532 2010· ISSN 1437-322X

WISSENSCHAFTLICH-TECHNISCHE BERICHTE

Forschungszentrum
Dresden Rossendorf

Terahertz studies on semiconductor quantum heterostructures in the low and high field regime

DISSERTATION

zur Erlangung des akademischen Grades
doctor rerum naturalium (Dr. rer. nat.)

durchgeführt am Forschungszentrum Dresden-Rossendorf

eingereicht an der Fakultät Mathematik und
Naturwissenschaften der Technischen Universität Dresden

von Dipl.-Phys. Martin Wagner

Forschungszentrum
Dresden Rossendorf

TECHNISCHE
UNIVERSITÄT
DRESDEN

Gutachter:

1. Prof. Dr. Manfred Helm (Technische Universität Dresden)
2. Prof. Dr. Thomas Dekorsy (Universität Konstanz)

eingereicht im Dezember 2009

Abstract

In this thesis we investigate experimentally certain aspects of the interaction of terahertz (THz) radiation with intersubband transitions and excitonic transitions in semiconductor quantum wells.
The first part deals with a more fundamental view on an intersubband transition in a symmetric, undoped GaAs/AlGaAs multiple quantum well. After optical excitation of carriers, the considered electronic conduction intersubband transition is probed in the low-intensity linear regime using broadband THz pulses. These pulses are detected via field-resolved electro-optic sampling. While the sample's terahertz absorption shows the expected single peak of the resonant intersubband transition, the differential transmission spectra, i.e. the photoexcitation-induced changes in transmission, display strong *Fano signatures*. On the basis of a microscopic theory, we show that they originate from a phase-sensitive *superposition of THz current and ponderomotive current*. The latter one results from the wiggling motion of carriers induced by the accelerating THz field. Our findings demonstrate for the first time that the ponderomotive contribution has to be taken into account also at the lowest THz intensities.
The following issues consider the interaction with THz pulses of higher intensity from the free-electron laser (FEL) of the Forschungszentrum Dresden-Rossendorf.
In one experiment we investigate efficient second-order *sideband generation* in the GaAs/AlGaAs multiple quantum well mentioned above. To this end a near-infrared laser tuned to excitonic interband transitions is mixed inside the sample with the in-plane polarized FEL beam to create the sum- and difference-frequencies between them. We compare the sideband efficiencies for the THz beam tuned to the interexcitonic heavy-hole light-hole transition and to the intraexcitonic heavy-hole 1s-2p transition. In the latter case we achieve a ten times higher n=+2 low-temperature efficiency around 0.1%. This value is comparable to previous studies in the literature, but our approach involves different transitions in a much simpler geometry. At room temperature the efficiency drops only by a factor of 7 for low THz powers.
The last part of this thesis addresses another fundamental quantum-mechanical phenomenon: the splitting of an absorption line in a strong THz field. In the same above-mentioned quantum well sample the FEL wavelength is tuned near the intraexcitonic 1s-2p heavy-hole transition. The THz radiation induces a power-dependent splitting of the heavy-hole 1s exciton absorption line which manifests itself in the transmitted spectrum of a broadband near-infrared probe beam. The FEL-wavelength-dependent strength of this so-called *Autler-Townes splitting* is discussed on the basis of a simple two-level model. Compared to previous work, this is the first clear observation of such a splitting induced by an intraexcitonic resonance.

Zusammenfassung

Gegenstand dieser Arbeit ist die experimentelle Untersuchung bestimmter Aspekte der Wechselwirkung von Terahertz (THz)-Strahlung mit Intersubband- und exzitonischen Übergängen in Halbleiter-Quantentöpfen (quantum wells).
Der erste Teil befasst sich mit einer grundlegenderen Sichtweise auf einen Intersubband-Übergang in symmetrischen, undotierten GaAs/AlGaAs Mehrfachquantentöpfen (multiple quantum well). Nach optischer Anregung von Ladungsträgern wird der betrachtete elektronische Intersubband-Übergang im Leitungsband abgefragt mittels breitbandiger THz-Pulse im linearen Regime niedriger Intensitäten. Diese Pulse werden feldaufgelöst durch elektro-optisches Abtasten detektiert. Während nun die THz-Absorption einzig das erwartete Maximum des resonanten Intersubband-Übergangs aufweist, zeigt das differentielle Transmissionsspektrum, d.h. die durch die optische Anregung bewirkte Transmissionsänderung, ausgeprägte *Fano-artige Signaturen*. Wir zeigen anhand unserer mikroskopischen Theorie, dass diese aus der phasenrichtigen *Superposition von THz- und ponderomotivem Strom* entstehen. Letzterer resultiert aus der oszillierenden Bewegung von Ladungsträgern im beschleunigenden THz-Feld. Unsere Ergebnisse demonstrieren zum ersten Mal, dass der ponderomotive Beitrag auch für niedrigste THz-Intensitäten Berücksichtigung finden muss.
Die folgenden Punkte beleuchten die Wechselwirkung mit starken THz-Pulsen des Freie-Elektronen Lasers (FEL) am Forschungszentrum Dresden-Rossendorf.
In einem Experiment untersuchen wir effiziente *Seitenband-Erzeugung* zweiter Ordnung in den oben erwähnten Mehrfachquantentöpfen. Dazu wird ein Nahinfrarot-Laser auf einen exzitonischen Interbandübergang eingestellt und mit dem in Quantentopf-Ebene polarisierten FEL-Strahl in der Probe gemischt, um die Summen- und Differenzfrequenzen zwischen beiden zu erzeugen. Wir stellen den FEL auf den inter-exzitonischen Schwerloch-Leichtloch-Übergang oder auf den intra-exzitonischen $1s$-$2p$ Schwerloch-Übergang ein, und vergleichen die Seitenband-Effizienz. Letztere Einstellung liefert eine zehnmal höhere $n{=}{+}2$ Seitenbandeffizienz um 0.1% für niedrige Temperaturen. Dieser Wert ist vergleichbar mit früheren Experimenten aus der Literatur, wohingegen unser Ansatz andere Übergänge und eine einfachere Geometrie ausnutzt. Bei Raumtemperatur sinkt die Effizienz nur um einen Faktor 7 für niedrige THz-Leistungen.
Zum Schluss dieser Arbeit wird ein anderer grundlegender quanten-mechanischer Effekt behandelt: das Aufspalten einer Absorptionslinie in einem starken THz-Feld. In obengenannter Quantentopfprobe wird die FEL-Strahlung nahe des intra-exzitonischen $1s$-$2p$ Schwerloch-Übergangs eingestellt. Sie verursacht ein leistungsabhängiges Aufspalten der exzitonischen $1s$ Schwerloch-Linie, welches sich im Transmissionsspektrum eines breitbandigen nahinfraroten Lasers zeigt. Die Stärke dieser sogenannten *Autler-Townes Aufspaltung* wird für verschiedene FEL-Wellenlängen diskutiert anhand eines einfachen Zweiniveausystems. Verglichen mit früheren Arbeiten ist dies die erste eindeutige Messung einer Aufspaltung, die durch eine intra-exzitonische Resonanz verursacht wird.

Contents

List of Figures

1. Introduction

Semiconductor heterostructures show interesting quantization effects that have become very important both in science and technology during the last decades. Their applications nowadays can be found in a broad range from sensing and spectroscopy utilizing miniaturized quantum cascade lasers (QCLs) [1, 2] and far-infrared light detectors like QWIPs [3], over telecommunication and information technology [4] to light-emitting diodes (LEDs) [5] and laser diodes [6] for everyday life. An important representative amongst heterostructures are semiconductor quantum wells. First realized in 1974 [7], this simple system consists of layers of two different semiconductor materials that are alternately grown onto each other. Due to their similar lattice constants GaAs wells and $Al_xGa_{1-x}As$ barriers (with $x > 0$) are the most important semiconductor material combination. Due to different band offsets, electrons and holes are confined spatially in the growth direction while their motion is still free in the remaining other two directions. This confinement gives rise to a quantization of states with a resulting subband structure. Besides quantum wells also other quantized systems can be tailored that differ in the degree of freedom for the carriers. Quantum dots (e.g. [8]) as artifical atoms are one extreme where the carriers are confined in all directions, resulting in discrete atom-like energy levels. Epitaxial growth with single atomic-layer precision and high degree of purity utilizing different semiconductor materials renders it possible to adjust the energy scales at wish, providing a perfect playground for the study of fundamental physical concepts in condensed matter.
Valuable tools to investigate those structures are optical experiments and spectroscopy. Most bulk semiconductors show *interband transitions* between valence- and conduction band in the range of 1 eV (1 eV $\widehat{=}$ 242 THz $\widehat{=}$ 1240 nm). Consequently, visible and near-infrared light were the natural sources for their optical investigation. However, below this energy scale there are various fundamental excitations. Bulk semiconductors reveal phonon resonances in the range of several tens of meV, for instance 36 meV (8.7 THz) for the GaAs LO-phonon. Also internal excitonic transitions are found in the few meV range, e.g. the $1s$-$2p$ transition in GaAs/AlGaAs quantum wells [9]. In semiconductor heterostructures the so-called *intersubband transitions* between the confined states occur within a broad region from 1.1 μm [10] to 200 μm [11] (273 THz - 1.5 THz). Obviously, the far- and mid-infrared part of the electromagnetic spectrum, the THz range between approximately 0.3 THz and 30 THz (1 THz $\widehat{=}$ 300 μm $\widehat{=}$ 4.14 meV), is very important when those structures are investigated. Unfortunately, experimentalists have gained access to THz frequencies only during the last decades when THz science itself has evolved to a very active area of research [12, 13]. The most com-

mon techniques for THz emission and detection are based on ultrafast photoconductive switches [14] and difference-frequency mixing [15]. Additionally, the free-electron laser (FEL) provides a powerful and widely tunable THz source [16], but at the expense of compactness. Such a large user facility is also located at the Forschungszentrum Dresden-Rossendorf.

Optical experiments in the mid- and far-infrared spectral region support the ongoing fundamental research that is necessary to improve current devices. Recent THz pump-probe studies on quantum dots, for instance, have explained the long relaxation times of excited carriers under certain conditions [8]. This knowledge might prove valuable for future THz laser designs on the basis of these structures, since in general, the upper laser level requires a long-lived state.

Since the first observation of a quantum well intersubband transition in 1985 [17], there have been countless studies on this type of transition. For their theoretical description the part of the light-matter interaction Hamiltonian that is quadratic in the vector potential $\mathbf{A}$ is usually neglected. Only recent experiments [18, 19] with strong THz fields showed rather indirect evidences for the role of the so-called *ponderomotive contribution* that results from this $\mathbf{A}^2$-Hamiltonian as a THz-induced wiggling motion of the carriers. In this thesis we will demonstrate that this part of the light-matter interaction has to be taken into account also at the lowest THz intensities under certain conditions. To this end we utilize broadband THz pulses to probe the electronic intersubband transition in the conduction band of undoped GaAs/AlGaAs quantum wells after optical excitation of carriers. The measured field-resolved THz response directly reveals the ponderomotive contribution. These experimental findings are unambiguously explained on the basis of a microscopic theory.

The other issues addressed in this thesis employ relatively strong THz fields and therefore make use of the on-site free-electron laser FELBE. Its THz pulses are mixed with near-infrared laser pulses in a quantum well structure to generate new frequencies via nonlinear optical sum- and difference-frequency generation. First observed in 1997 rather by chance [20], this *sideband generation* has been performed in various quantum well heterostructures with a possible future application in telecommunication or in a transport of THz signals on near-infrared carriers within optical fibers. We investigate an efficient way of this nonlinear mixing in a quite simple quantum well geometry.

Finally, we concentrate on a more fundamental quantum mechanical effect, i.e. the dressing of energy states in a strong electric field. Using NIR probe light we will study the wavelength-dependent splitting of an excitonic state in a multiple quantum well sample when illuminated with a strong THz field from the FEL. Such a so-called *Autler-Townes splitting* was observed in 2005 for the first time in quantum wells [21], whereas it is known in atomic spectroscopy since the 1950s [22]. Differently from the literature, our study is based on an intraexcitonic transition instead of an excitonic one. Possible future applications could be optical modulators.

In summary, this thesis will investigate experimentally certain THz-field induced fundamental phenomena concerning intersubband transitions and excitonic transitions in semiconductor heterostructures.

2. Fundamentals

This chapter deals with the basic concepts. We will introduce semiconductor quantum wells, intersubband transitions, waveguide geometries and nonlinear optics. The latter one is necessary to understand phase-matched difference-frequency mixing which is also summarized here, and which is the basis of our THz setup. Apart from that nonlinear optics is required to describe sideband generation, which is why the nonlinear susceptibilities are treated in more detail.

2.1. Two-dimensional quantum wells and intersubband transitions

Semiconductor quantum well

A quantum well is the conceptually simplest semiconductor heterostructure and is described in various textbooks, for instance [23]. A several nanometer thin layer of a low-bandgap material like GaAs is sandwiched in between two layers of higher-bandgap material like $Al_{0.33}Ga_{0.67}As$. Because of the bandgap discontinuity in growth (z-) direction, rectangular potential wells result in the conduction and valence bands for the electrons and holes, as sketched in Fig. 2.1(a). The corresponding Schrödinger equation for a periodic crystal potential $U(\mathbf{r})$ with the superimposed confinement potential $V(\mathbf{r}) = V(z)$ reads:

$$\left[-\frac{\hbar^2}{2m}\left(\frac{\partial^2}{\partial x^2}+\frac{\partial^2}{\partial y^2}+\frac{\partial^2}{\partial z^2}\right)+U(\mathbf{r})+V(z)\right]\Psi_{\nu,n}(\mathbf{r}) = E_{\nu,n}\Psi_{\nu,n}(\mathbf{r}). \tag{2.1}$$

We assume that the total wave function $\Psi_{\nu,n}(\mathbf{r})$ can be factorized into a lattice periodic Bloch function $u_\nu(\mathbf{r})$ and a slowly varying envelope function $f_n(\mathbf{r})$ (*envelope function approximation*). Furthermore, we assume that the Bloch function is identical in both materials. Then the Schrödinger equation for the envelope function in the effective mass approximation is given by

$$\left[-\frac{\hbar^2}{2m^*}\left(\frac{\partial^2}{\partial x^2}+\frac{\partial^2}{\partial y^2}+\frac{\partial^2}{\partial z^2}\right)+V(z)\right]f_n(\mathbf{r}) = E_n f_n(\mathbf{r}). \tag{2.2}$$

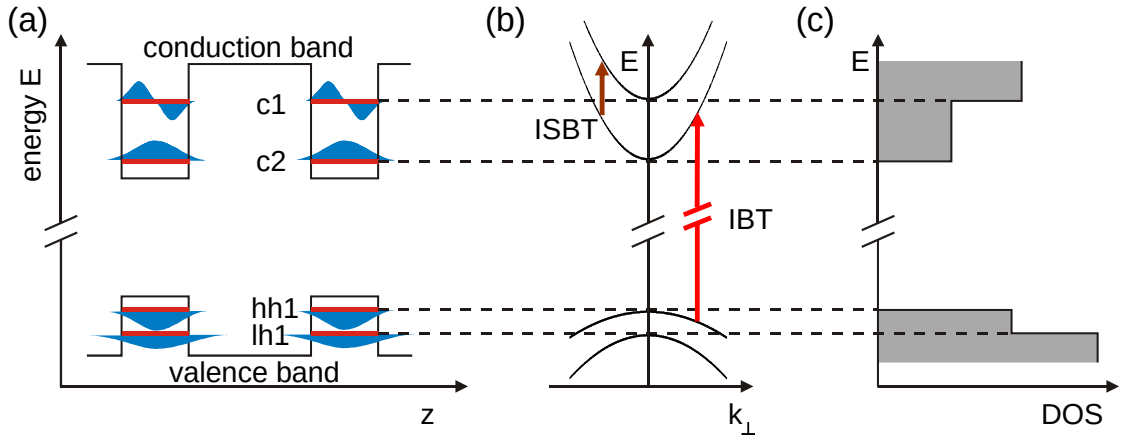

Figure 2.1.: (a) Scheme of two quantum wells. Due to the confinement in z-direction, discrete electronic energy levels c1 and c2 in the conduction band and hole levels hh1 and lh1 in the valence band result. The absolute values of the wave functions are sketched (blue shaded areas). (b) Subband dispersion in x- and y-direction. Interband (IBT) and intersubband (ISBT) transitions are indicated. (c) Corresponding density of states (DOS).

While confined in z-direction, the carriers are still free to move in the x- and y-direction. Hence, we try the ansatz $f_n = \frac{1}{\sqrt{S}} \exp[i(k_x x + k_y y)]\phi_n(z)$ (normalized to the sample area S) and end up with the one-dimensional Schrödinger equation:

$$\left(-\frac{\hbar^2}{2m^*}\frac{\partial^2}{\partial z^2} + V(z)\right)\phi_n(z) = \left(E_n + \frac{\hbar^2(k_x^2+k_y^2)}{2m^*}\right)\phi_n(z). \tag{2.3}$$

The energy dispersion $E(\mathbf{k}) = E_n + \frac{\hbar^2(k_x^2+k_y^2)}{2m^*}$ is composed of the discrete energy E_n in the n-th level and a continuous free-carrier like dispersion for in-plane wavevectors $\mathbf{k}_\perp$. This leads to the formation of *subbands*, as can be seen from Fig. 2.1(b). For an infinitely deep rectangular well with a width l the energy scales as $E_n \propto n^2/(m^* l^2)$.
Another important characteristic is the density of states (DOS) that defines the number of states N for electrons or holes in an energetic interval E. For a d-dimensional heterostructure (d=1,2,3)[1] it reads:

$$\mathrm{DOS}(E) = \frac{dN}{dE} = \frac{dN}{dk}\frac{dk}{dE} \propto E^{\frac{d}{2}-1}. \tag{2.4}$$

Consequently, the square-root shaped 3-dimensional DOS for a bulk semiconductor reduces to a constant DOS for a single band in a 2-dimensional quantum well. This is plotted in Fig. 2.1(c), where a step-like density of states is formed from the individual subband contributions according to $\mathrm{DOS}(E) = \sum_n \frac{m^*}{\pi\hbar^2}\Theta(E - E_n)$ with the Heaviside function Θ.
Successive growth of single quantum wells onto each other with barriers in between leads to a multiple quantum well as long as the wave functions of the confined carriers

[1] Ideal quantum dots with d=0 have a discrete density of states described by a delta function.

do not penetrate into adjacent wells. Otherwise a so-called *superlattice* is created, where the degeneracy of the single quantum well eigenstates is lifted to form so-called *minibands* with extended states in z-direction.

Intersubband transitions

Between the subbands of quantum wells carrier transitions can occur. These *intersubband* transitions might be induced by optical absorption or emission, respectively, or carrier-phonon scattering (compare Fig. 2.1(b)). In contrast to broad *interband* absorption spectra, intersubband absorption exhibits narrow lines and large cross sections [17]. This is a direct consequence of the same curvature of the participating subbands. Intersubband and interband transitions in GaAs/AlGaAs quantum wells occur energetically between the bandgaps of their bulk constituents. However, in order to observe intersubband transitions the light has to be polarized in quantum well growth direction (*intersubband selection rule*) [24, sec. 1.II] (see also appendix A). Furthermore, only intersubband transitions between states of different parity can occur in a *symmetric* well, i.e. $|1\rangle \rightarrow |2\rangle$ is allowed, while $|1\rangle \rightarrow |3\rangle$ is dipole-forbidden.
Figure 2.2 shows an example for intersubband transitions, taken with an FTIR spectrometer (*Bruker: Equinox 55*). The sample, already described in [25], is a modulation-

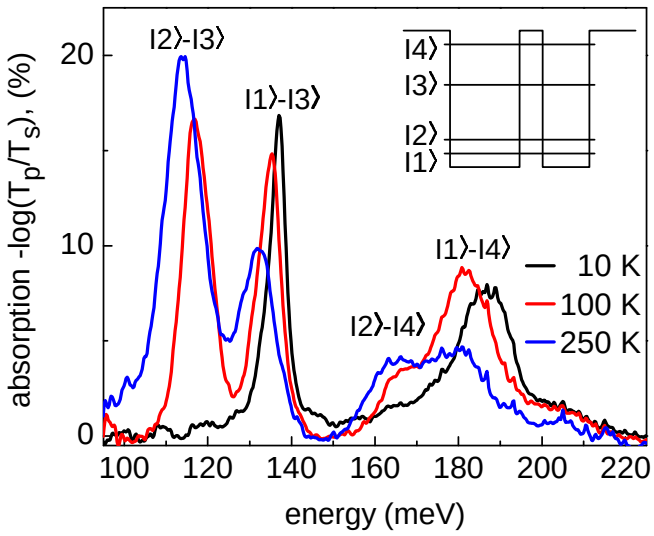

Figure 2.2.: Temperature-dependent intersubband absorption (taken with an FTIR spectrometer) in a modulation-doped coupled double quantum well (see inset for a sketch, material parameters in the text or [25]). At low temperature only the transitions from the occupied ground state $|1\rangle$ appear. With increasing temperature the second level $|2\rangle$ is filled which gives rise to additional absorption lines. Note that the double quantum well asymmetry relaxes the transition selection rules and allows transitions that are forbidden in symmetric wells, for instance the $|1\rangle \rightarrow |3\rangle$ transition.

doped ($4\times10^{11}/\mathrm{cm}^2$) *asymmetric* double quantum well with 6 and 7 nm thin GaAs wells, coupled by a 2 nm thin $Al_{0.33}Ga_{0.67}As$ barrier (see Fig. 2.2 inset for a sketch). Fifty of those double quantum wells have been grown, separated by 95 nm thick $Al_{0.33}Ga_{0.67}As$ spacer layers. Here, two quantum wells of different widths are coupled which results in a splitting of the degenerate single well eigenstates. The asymmetry of the structure relaxes the intersubband transition rules. At low temperature when only the ground state $|1\rangle$ is occupied, the $|1\rangle \rightarrow |3\rangle$ and $|1\rangle \rightarrow |4\rangle$ transitions are observed. With increasing temperature the second state is thermally populated and additional transitions ($|2\rangle \rightarrow |3\rangle$ and $|2\rangle \rightarrow |4\rangle$) appear. We also observe a broadening and only a moderate change in absorption strength that is mainly due to a change in the occupation of states. Additionally, a slight shift of the peaks towards lower energies occurs. Note the Lorentzian line shape of the transitions.
For observing the intersubband transition the sample has been polished in a 38° triangle-like waveguide. The intersubband absorption is then obtained as ratio of the transmitted *p*-polarized light that is partly polarized in quantum well growth direction and the transmission for the perpendicular, in-plane *s*-polarization. We will now briefly discuss why those waveguide geometries are needed.

Waveguide geometries

Since intersubband spectroscopy relies on the polarization component in quantum well growth direction, different coupling schemes have been developed that have to consider the spatial intensity distribution of the probe light within the sample [24, sec. 1.IV].
Normal incidence illumination does not provide the required polarization component, but irradiation at Brewster's angle does. However, due to the high refractive index η of semiconductors at infrared wavelengths, the internal angle Θ between light propagation direction and quantum well plane normal is rather small at Brewster's angle[2]. Only $\sin(\Theta)$ of the probe field amplitude proves intersubband-active and the interaction length is $1/\cos(\Theta)$. Hence, the coupling strength for the light intensity is only $\beta = \sin^2(\Theta)/\cos(\Theta) \approx 0.09$ for GaAs, for instance.
The most common geometries realize an internal angle of 45° or nearly 52° with two passes through the active layer. The coupling factor then increases to $2\times\beta(45°) \approx 1.41$ and $2\times\beta(52°) \approx 2.0$, respectively. As sketched in Fig. 2.3(a), those geometries employ specially processed waveguides where the facets are polished under a certain angle. Wedged waveguides with a facet angle of $\alpha = 45°$ are advantageous for absorption measurements where the transmission of intersubband-active *p*-polarized light is normalized to the *s*-polarized transmission. Both beams undergo identical reflection losses at the facets. A drawback is the introduction of a vertical beam displacement. With a facet angle of $\alpha = 38°$ the reflected beam inside the waveguide travels parallel to the entrance facet and exits the sample without beam displacement, given the waveguide has

[2] For GaAs with $\eta = 3.3$ we find a Brewster angle $\Theta_B = \arctan(\eta) = 73°$ and an internal angle of $\Theta = 17°$.

the appropriate length. Here, the internal angle is $\Theta = \alpha + \arcsin[\sin(90° - \alpha)/\eta] \approx 52°$. However, this waveguide produces different reflection losses for p- and s-polarized light. In waveguide geometries standing wave effects have to be considered. A standing wave results from the interference of the incident and reflected beam at the semiconductor-air interface. Their phase shift calculated from the Fresnel's equations is 168° for a 45° angle of incidence on the interface. This nearly complete phase reversal leads to a standing-wave pattern for the z-component of the electric field with a spatial periodicity for the intensity maxima of $\lambda/[2\eta\cos(\Theta)]$ (λ is the vacuum wavelength) [26].
Since we employ a 38° wedged waveguide we give the THz intensity profile of the intersubband-active z-component in Fig. 2.3(b) for a wavelength of 11 μm (in vacuum) that corresponds to the intersubband resonance of our sample. We assume a perfect phase reversal at the semiconductor-air interface, leading to an intensity node there. This can be remedied by changing the boundary condition via evaporation of a metallic film. In our sample we have introduced a spacer layer of 300 nm to shift the quantum wells (shaded area) away from the interface. It is also ensured that the active structure can be excited efficiently over the entire depth via near-infrared laser illumination. Note that the grown structure with a given intersubband resonance wavelength is only optimized for a certain waveguide geometry and can prove unfavorable for others. This is plotted for a facet angle of 70° (dashed line) where the THz beam is almost perfectly polarized in growth direction, but where the spatial overlap is poor.

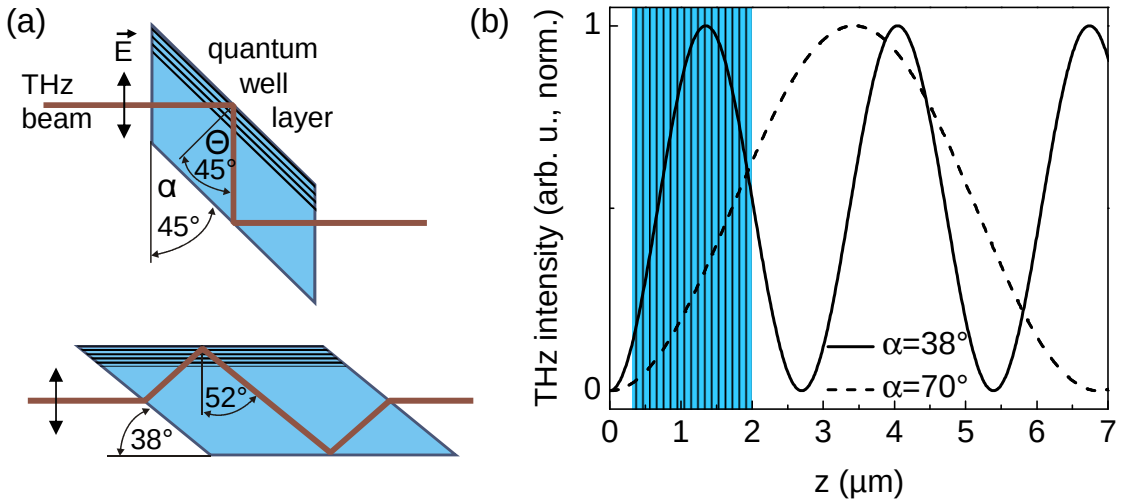

Figure 2.3.: (a) Waveguide geometries for two different external angles α. The THz beam is shown for intersubband-active p-polarized light. An $\alpha = 45°$ waveguide with the same internal angle $\Theta = 45°$ displaces the beam (top). We employ an $\alpha = 38°$ waveguide (bottom). (b) Intensity standing wave pattern for two different waveguides and a (vacuum) wavelength of 11 μm matching our intersubband resonance. z is the distance from the GaAs semiconductor-air interface. In both cases an intensity node is found at the interface. The quantum wells in our sample (shaded area) are covered by the $\alpha = 38°$ waveguide standing wave intensity maximum (solid line), but not in the case of the $\alpha = 70°$ waveguide (dashed line).

2.2. Nonlinear optics

Nonlinear optics describes the interaction of light with matter at high intensities. The electromagnetic wave with the electric field $\mathbf{E}(\mathbf{r},t)$ results in a material polarization $\mathbf{P}(\mathbf{r},t)$ which serves again as radiation source via the following wave equation:

$$\nabla \times \nabla \times \mathbf{E}(\mathbf{r},t) - \epsilon_0\mu_0 \frac{\partial^2 \mathbf{E}(\mathbf{r},t)}{\partial t^2} = \mu_0 \frac{\partial^2 \mathbf{P}(\mathbf{r},t)}{\partial t^2}, \tag{2.5}$$

where ϵ_0 and μ_0 are the vacuum permittivity and permeability, respectively. Nonlinear effects can be expected above an electric field strength of 1 kV/cm [27, p. 1], a regime that has become available with the invention of the laser. $\mathbf{P}(\mathbf{r},t)$ with its components $P_i(\mathbf{r},t)$ can be expressed as a power series in the electric field $E_i(\mathbf{r},t)$ [28, p. 2 *ff.*]:

$$\begin{aligned} P_i &= \epsilon_0 \sum_j \chi^{(1)}_{ij} E_j + \epsilon_0 \sum_{jk} \chi^{(2)}_{ijk} E_j E_k + \epsilon_0 \sum_{jkl} \chi^{(3)}_{ijkl} E_j E_k E_l + ... \\ &= P_i^{(1)} + P_i^{(2)} + P_i^{(3)} + ... \end{aligned} \tag{2.6}$$

where $\chi^{(1)}_{ij}, \chi^{(2)}_{ijk}, ...$ is the linear (second-order, ...) susceptibility tensor. For simplicity, we assume an instantaneous and local response and a frequency-independent susceptibility. For low electric fields only the linear susceptibility has to be taken into account leading to linear optics. However, for higher electric field strengths additional terms have to be considered. As an example we look at a superposition of two planar waves $E(t) = E_1 \sin(\omega_1 t) + E_2 \sin(\omega_2 t)$ incident to a nonlinear material in one spatial dimension. The resulting absolute value of the second-order polarization according to Eq. (2.6) reads:

$$\begin{aligned} P^{(2)}(t) = 1/2\epsilon_0\chi^{(2)} \quad [\quad & E_1^2 + E_2^2 \\ - \quad & E_1^2 \cos(2\omega_1 t) - E_2^2 \cos(2\omega_2 t) \\ - \quad & 2E_1E_2 \cos((\omega_1+\omega_2)t) \\ + \quad & 2E_1E_2 \cos((\omega_1-\omega_2)t)]. \end{aligned} \tag{2.7}$$

The first line represents a static polarization known as *optical rectification*. The second line describes *second-harmonic generation*. Line three and four contain a mixing of the two involved frequencies, namely *sum-* and *difference-frequency mixing*, which is the basis of THz generation (within broadband laser pulses) and near-infrared–terahertz sideband mixing.

So far we have considered a lossless and dispersionless medium where χ is real and frequency-independent. Here, we give a more general definition of the polarization and the susceptibility, following closely Boyd's book [28, p. 17 *ff.*]. We assume that the electrical field vector $\tilde{\mathbf{E}}(\mathbf{r},t)$ can be expressed as discrete sum of frequency components:

$$\tilde{\mathbf{E}}(\mathbf{r},t) = \sum_n \mathbf{E}(\omega_n) e^{-i\omega_n t}. \tag{2.8}$$

The summation is performed over all frequencies, both positive and negative. In order to represent the physical field, $\tilde{\mathbf{E}}(\mathbf{r},t)$ has to be a real valued quantity which requires $\mathbf{E}(-\omega_n) = \mathbf{E}(\omega_n)^*$. In analogy to equation (2.8) we write the polarization as

$$\tilde{\mathbf{P}}(\mathbf{r},t) = \sum_n \mathbf{P}(\omega_n) e^{-i\omega_n t}. \tag{2.9}$$

The *first-order susceptibility* $\chi^{(1)}_{ij}$ is defined as constant of proportionality via

$$P^{(1)}_i(\omega_m) = \epsilon_0 \sum_j \chi^{(1)}_{ij}(\omega_m) E_j(\omega_m). \tag{2.10}$$

In a similar way, the *second- and third-order susceptibilities* $\chi^{(2)}_{ijk}$ and $\chi^{(3)}_{ijkl}$ are given:

$$P^{(2)}_i(\omega_n + \omega_m) = \epsilon_0 \sum_{jk} \sum_{(nm)} \chi^{(2)}_{ijk}(\omega_n + \omega_m, \omega_n, \omega_m) E_j(\omega_n) E_k(\omega_m) \tag{2.11}$$

$$P^{(3)}_i(\omega_o + \omega_n + \omega_m) = \epsilon_0 \sum_{jkl} \sum_{(onm)} \chi^{(3)}_{ijkl}(\omega_o + \omega_n + \omega_m, \omega_o, \omega_n, \omega_m) E_j(\omega_o) E_k(\omega_n) E_l(\omega_m). \tag{2.12}$$

The summation over (nm) means that the sum $\omega_n + \omega_m$ has to be kept fixed and ω_n and ω_m are allowed to vary, while performing the summation.
We like to calculate explicit expressions for the optical susceptibility for a free atom in order to show the dependence on dipole transition moments and energy levels. We will come back to these expressions when discussing sideband generation in chapter 5.
Standard quantum-mechanical perturbation theory is used to solve Schrödinger's equation with light-matter interaction [28, sec. 3.2]. Originally, this formalism can only describe the *nonresonant* response without relaxation processes which would be included in a more complicated density matrix approach. However, in order to adapt the formalism to our *resonant* sideband generation, relaxation processes are incorporated later on via a phenomenological decay rate Γ.
We consider the time-dependent Schrödinger equation

$$i\hbar \frac{\partial \psi}{\partial t} = \hat{H}\psi \tag{2.13}$$

with the atomic wave function $\psi(\mathbf{r},t)$ and the Hamiltonian operator

$$\hat{H} = \hat{H}_0 + \hat{V}(t) = \hat{H}_0 - \hat{\boldsymbol{\mu}} \cdot \tilde{\mathbf{E}}(t) = \hat{H}_0 + e\hat{\mathbf{r}} \cdot \tilde{\mathbf{E}}(t). \tag{2.14}$$

$\hat{V}(t) = -\hat{\boldsymbol{\mu}} \cdot \tilde{\mathbf{E}}(t)$ describes the interaction between the atom and the electromagnetic wave in the electric dipole approximation with the dipole moment operator $\hat{\boldsymbol{\mu}} = -e\hat{\mathbf{r}}$. The electronic charge is $-e$, and $\tilde{\mathbf{E}}(t)$ is represented according to Eq. (2.8). $\hat{H}_0$ denotes the unperturbed Hamiltonian, i.e. no external field is applied. For this case we assume that the unperturbed atom is initially in state g at an energy $\hbar\omega_g$. Then the wave function solving Eq. (2.13) without electromagnetic field is of the form

$$\psi^{(0)}(\mathbf{r},t) = u_g(\mathbf{r}) e^{-i\omega_g t}, \tag{2.15}$$

where the spatially varying part $u_g(\mathbf{r})$ satisfies the time-independent Schrödinger equation. Treating $\hat{V}(t)$ as a small perturbation [28, p. 104 *ff.*] one can derive an expression $\psi^{(1)}$ for the first perturbative correction to the total wave function $\psi = \psi^{(0)} + \psi^{(1)} + ...$, that is linear in the applied field:

$$\psi^{(1)}(\mathbf{r},t) = \frac{1}{\hbar}\sum_m \sum_p \frac{\boldsymbol{\mu}_{mg}\cdot\mathbf{E}(\omega_p)}{\omega_{mg}-\omega_p} e^{i(\omega_{mg}-\omega_p)t} u_m(\mathbf{r}) e^{-i\omega_m t}. \tag{2.16}$$

Here, $\mathbf{E}$ is the electric field amplitude according to Eq. (2.8). $\boldsymbol{\mu}_{mg} = \int u_m^*(\mathbf{r})\hat{\boldsymbol{\mu}} u_g(\mathbf{r}) d^3r$ is the dipole transition moment between states m and g that have an energy difference of $\omega_{mg} = \omega_m - \omega_g$.
Now we can evaluate the expectation value of $\hat{\boldsymbol{\mu}}$,

$$\langle\tilde{\mathbf{p}}\rangle = \langle\psi\,|\hat{\boldsymbol{\mu}}|\,\psi\rangle\,, \tag{2.17}$$

which is connected to the material polarization $\tilde{\mathbf{P}} = N\langle\tilde{\mathbf{p}}\rangle$ via the number density of atoms N. The lowest-order contribution in $\langle\tilde{\mathbf{p}}\rangle$ that is linear in the field reads

$$\left\langle\tilde{\mathbf{p}}^{(1)}\right\rangle = \left\langle\psi^{(0)}\,|\hat{\boldsymbol{\mu}}|\,\psi^{(1)}\right\rangle + \left\langle\psi^{(1)}\,|\hat{\boldsymbol{\mu}}|\,\psi^{(0)}\right\rangle. \tag{2.18}$$

Inserting the wave functions (2.15) and (2.16) in Eq. (2.18) leads to the linear material polarization $\tilde{\mathbf{P}}^{(1)} = \sum_p \mathbf{P}^{(1)}(\omega_p)\exp(-i\omega_p t)$ (see Eq. (2.9)) that can be expressed in terms of the complex amplitude $P_i^{(1)}(\omega_p) = \epsilon_0 \sum_j \chi_{ij}^{(1)}(\omega_p) E_p(\omega_p)$ (see Eq. (2.10)). By comparison we find for the linear susceptibility:

$$\chi_{ij}^{(1)}(\omega_p) = \frac{N}{\epsilon_0\hbar}\sum_m \Big(\frac{\mu_{gm}^i\mu_{mg}^j}{\omega_{mg}-\omega_p-i\Gamma_m/2} + \frac{\mu_{gm}^j\mu_{mg}^i}{\omega_{mg}+\omega_p+i\Gamma_m/2}\Big). \tag{2.19}$$

In order to extend the formalism and include damping effects for resonant conditions we have introduced the population decay rate Γ_m of the real level m by replacing ω_{mg} with $\omega_{mg} - i\Gamma_m/2$.
Large values for $\chi_{ij}^{(1)}(\omega_p)$ are obtained for large transition dipoles, i.e. for allowed transitions, and in the case of *resonance enhancement* when the frequency ω_p approaches the resonance frequency ω_{mg}. In Fig. 2.4(a) the two terms are sketched in an energy level picture where the level m is located for the case of resonance enhancement. When g denotes the ground state, only the first *resonant* contribution is physical reality, whereas the *antiresonant* contribution can only become resonant for undefined negative frequencies $\omega_p < 0$. In the case of resonance enhancement when ω_p is close to the transition ω_{mg} between real states the second antiresonant contribution can be neglected and $\chi_{ij}^{(1)}(\omega_p)$ can be simplified as

$$\chi_{ij}^{(1)}(\omega_p) = \frac{N}{\epsilon_0\hbar}\mu_{gm}^i\mu_{mg}^j \frac{(\omega_{mg}-\omega_p)+i\Gamma_m/2}{(\omega_{mg}-\omega_p)^2+(\Gamma_m/2)^2}. \tag{2.20}$$

Figure 2.4(b) displays the real and imaginary part of $\chi_{ij}^{(1)}(\omega_p)$. While the real part

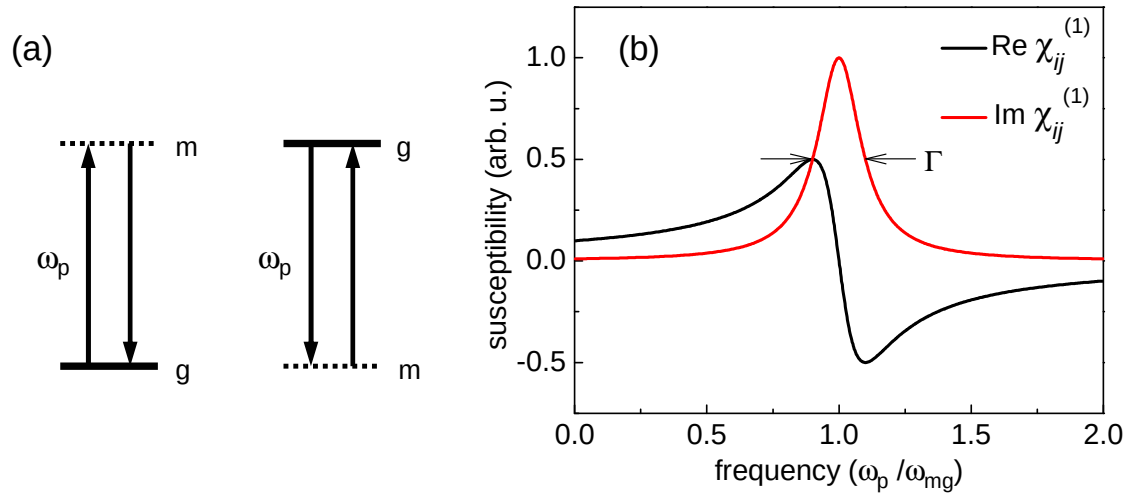

Figure 2.4.: (a) Energy level diagram of the resonant and antiresonant contribution to the linear susceptibility. The case of resonance enhancement is shown where $\omega_p = \omega_{mg}$. (b) Real and imaginary part of the linear susceptibility. The latter one is a Lorentzian with a FWHM of Γ.

changes its sign at the resonance frequency ω_{mg}, one observes a Lorentzian line shape with a full width at half maximum of Γ in the imaginary part. $\chi^{(1)}$ is connected to the absorption α via $\alpha(\omega) = \omega \mathrm{Im}(\chi^{(1)}(\omega))/(n(\omega)c)$, where c is the vacuum speed of light and n is the real part of the complex refractive index $\sqrt{1+\chi^{(1)}(\omega)}$. Obviously, the absorption also reveals a Lorentzian line shape.
In close analogy to the derivation of $\chi^{(1)}$ one finds the second- and third-order perturbative contribution, i.e. those contributions to the polarization that are proportional to the power of two and three, respectively, of the applied electric field. $\chi^{(2)}_{ijk}$ reads

$$\chi^{(2)}_{ijk}(\omega_p+\omega_q,\omega_p,\omega_q) = \frac{N}{2\epsilon_0\hbar^2}\sum_{mn}\Bigg(\frac{\mu^i_{gn}\mu^j_{nm}\mu^k_{mg}}{(\omega_{ng}-\omega_p-\omega_q-i\Gamma_{ng}/2)(\omega_{mg}-\omega_p-i\Gamma_{mg}/2)} + \frac{\mu^i_{gn}\mu^k_{nm}\mu^j_{mg}}{(\omega_{ng}-\omega_q-\omega_p-i\Gamma_{ng}/2)(\omega_{mg}-\omega_q-i\Gamma_{mg}/2)} + \ldots\Bigg). \tag{2.21}$$

Figure 2.5(a) illustrates the situation for resonance enhancement. Equation (2.21) includes a permutation of the indices p and q and the corresponding coordinates j and k. The whole formula contains four additional terms where two of them (including permutations) are shown in panel (b). These terms use a ground state g that is energetically higher than the involved virtual states. They are neglected since in our system the real energy levels for resonance enhancement lie above g.

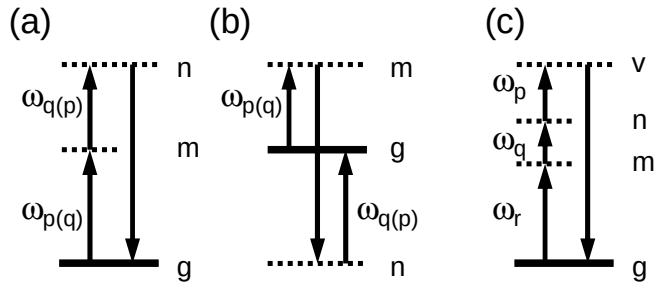

Figure 2.5.: (a) Energy level resonances for $\chi^{(2)}_{ijk}(\omega_p + \omega_q, \omega_p, \omega_q)$, including the permutation $\omega_p \rightarrow \omega_q$. (b) One of the missing terms in Eq. (2.21) where the ground state g is not the lowest energy level. (c) Resonant structure for the third-order susceptibility (Eq. (2.22)).

In sideband generation we will use the third-order susceptibility which is found as

$$\chi^{(3)}_{ijkl}(\omega_p + \omega_q + \omega_r, \omega_p, \omega_q, \omega_r) = \frac{N}{\epsilon_0 \hbar^3} \mathcal{P}\Big[\sum_{mnv} \Big(\frac{\mu^i_{gv} \mu^j_{vn} \mu^k_{nm} \mu^l_{mg}}{(\omega_{vg} - \omega_p - \omega_q - \omega_r - i\Gamma_{vg}/2)(\omega_{ng} - \omega_q - \omega_r - i\Gamma_{ng}/2)(\omega_{mg} - \omega_r - i\Gamma_{mg}/2)} + ... \Big) \Big]. \tag{2.22}$$

$\mathcal{P}$ is the intrinsic permutation operator, acting on the following expression in the brackets [ ] such that one has to average over all six permutations of the input frequencies ω_p, ω_q and ω_r while simultaneously permuting the cartesian indices j, k and l. The complete expression (2.22) including permutations comprises 24 terms. However, similar to Eq. (2.21) those terms where g is not the lowest energy level have been dropped. Figure 2.5(c) depicts the positions of the energy levels n, m and v for resonance enhancement.

2.3. Phase-matched difference-frequency mixing

Our approach to broadband THz generation is based on phase-matched difference-frequency generation (DFG) where all the frequency components within a single near-infrared (NIR) broadband laser pulse are mixed in a nonlinear crystal to get the difference-frequencies that lie in the THz spectral region. DFG is a $\chi^{(2)}$ process and is also referred to as optical rectification, since the resulting THz frequencies are much smaller than the NIR frequencies. The corresponding polarization $\mathbf{P}^{(2)}$ for mixing of two fields $\mathbf{E}(\mathbf{r}, \omega_1)$ and $\mathbf{E}(\mathbf{r}, \omega_2)$ is given by (compare Eq. (2.11)):

$$P^{(2)}_i(\mathbf{r}, \omega_0) = 2\epsilon_0 d^{(2)}_{ijk}(\omega_0; \omega_1, \omega_2) E_j(\mathbf{r}, \omega_1) E_k(\mathbf{r}, \omega_2), \tag{2.23}$$

where $d^{(2)}_{ijk} = \frac{1}{2}\chi^{(2)}_{ijk}$. Since we are far from any resonance in the system, the nonlinear coefficient is frequency-independent and one can also apply Kleinman's symmetrie rule,

i.e. the indices are freely permutable [28, p. 37 *ff.*]: d_{ijk} simplifies to d_{il}.
The polarization is connected to the emitted fields by the wave equation (Eq. (2.5)) which is given in the frequency domain by [28, p. 62]

$$\nabla \times \nabla \times \mathbf{E}(\mathbf{r},\omega) - \frac{\omega^2}{c^2}\underline{\boldsymbol{\epsilon}}^{(1)}(\omega)\mathbf{E}(\mathbf{r},\omega) = \frac{\omega^2}{c^2\epsilon_0}\mathbf{P}^{(2)}(\mathbf{r},\omega). \tag{2.24}$$

Here, $\underline{\boldsymbol{\epsilon}}^{(1)}(\omega) = \underline{\mathbf{1}} + \underline{\boldsymbol{\chi}}^{(1)}(\omega)$ stands for the frequency dependent dielectric tensor. DFG is a process involving three waves. Of course, all of them have to fulfill Eq. (2.24), which results in three coupled wave equations. We assume plane waves with a common collinear direction of propagation. Thus, two electric fields $E_1(z,\omega)$ and $E_2(z,\omega+\Delta\omega)$ generate a field $E_{\mathrm{THz}}(z,\Delta\omega)$ at the difference-frequency $\Delta\omega$:

$$\begin{aligned} E_1(z,\omega) &= \mathrm{Re}(A_1(z,\omega)\mathrm{e}^{\mathrm{i}k_1(\omega)z}) = \frac{1}{2}A_1(z,\omega)\mathrm{e}^{\mathrm{i}k_1(\omega)z} + c.c. \qquad (2.25)\\ E_2(z,\omega+\Delta\omega) &= \frac{1}{2}A_2(z,\omega+\Delta\omega)\mathrm{e}^{\mathrm{i}k_2(\omega+\Delta\omega)z} + c.c.\\ E_{\mathrm{THz}}(z,\Delta\omega) &= \frac{1}{2}A_{\mathrm{THz}}(z,\Delta\omega)\mathrm{e}^{\mathrm{i}k_{\mathrm{THz}}(\Delta\omega)z} + c.c.\,. \end{aligned}$$

$A(z,\omega)$ is a complex-valued amplitude that is slowly varying in the z-coordinate. Inserting this ansatz into the polarization (2.23) and the wave equation (2.24) yields for the THz amplitude $A_{\mathrm{THz}}(z,\Delta\omega)$ that we are interested in:

$$\frac{\partial}{\partial z}A_{\mathrm{THz}}(z,\Delta\omega) + c.c. = \frac{\mathrm{i}(\Delta\omega)^2 d}{2c^2 k_{\mathrm{THz}}(\Delta\omega)}A_1(z,\omega)A_2^*(z,\omega+\Delta\omega)\mathrm{e}^{\mathrm{i}\Delta kz} + c.c.\,. \tag{2.26}$$

d is the effective nonlinear coefficient that includes the phase-matching angles, as shown on the next page. The second derivative resulting from $\nabla\times\nabla\times$ (in Eq. (2.24)) has been neglected compared to the first one, i.e. $|\frac{\partial^2}{\partial z^2}A_{\mathrm{THz}}| \ll |k_{\mathrm{THz}}\frac{\partial}{\partial z}A_{\mathrm{THz}}|$. This *slowly-varying-amplitude approximation* holds when the fractional change in A_{THz} over a distance of one wavelength is much smaller than unity. Furthermore, we have introduced the phase-mismatch which we will deal with in the next section:

$$\Delta k = k_2(\omega+\Delta\omega) - k_1(\omega) - k_{\mathrm{THz}}(\Delta\omega). \tag{2.27}$$

Since the generated THz field is much weaker than the incident fields, we can take $E_1(z,\omega)$ and $E_2(z,\omega+\Delta\omega)$ as constant and neglect their coupled differential equations. Integration of Eq. (2.26) over the whole length L of the crystal yields the amplitude of the THz field at the exit of the crystal:

$$A_{\mathrm{THz}}(z,\Delta\omega) = \frac{(\Delta\omega)^2 d}{2c^2 k_{\mathrm{THz}}(\Delta\omega)}A_1(\omega)A_2^*(\omega+\Delta\omega)\left(\frac{\mathrm{e}^{\mathrm{i}\Delta kL}-1}{\Delta k}\right). \tag{2.28}$$

Phase-matching in GaSe

By calculating the intensity from the amplitude A_{THz} (Eq. (2.28)), one obtains a function with a maximum at $\Delta k = 0$:

$$I_{\mathrm{THz}} \propto \frac{\sin^2(\Delta k L/2)}{(\Delta k L/2)^2}. \tag{2.29}$$

Hence, phase-matching or equivalently $\Delta k = 0$ leads to very efficient nonlinear mixing. From Eq. (2.27) we find that this simply manifests the conservation of momentum for the three-photon process. One obtains an alternative point of view by dividing $\Delta\omega$ by $k_{\mathrm{THz}}(\Delta\omega)$ that is given in Eq. (2.27):

$$\frac{\Delta\omega}{k_{\mathrm{THz}}(\Delta\omega)} = \frac{\Delta\omega}{k_2(\omega+\Delta\omega) - k_1(\omega)}. \tag{2.30}$$

This equation requires the THz pulse phase velocity $v_{\mathrm{THz}}^{\mathrm{phase}} = \Delta\omega/k_{\mathrm{THz}}(\Delta\omega)$ (left hand side of the equation) to be identical with the group velocity of the NIR pulse $v_{\mathrm{NIR}}^{\mathrm{group}} = \partial\omega/\partial k$ (approximately on the right hand side of the equation). Otherwise, a generated THz pulse would be out of phase with a previously generated one and they would not interfere constructively. Phase-matching is less critical for mixing in thin nonlinear media, as can be seen from Eq. (2.29).

Phase-matching is normally not possible in a medium with normal dispersion and far from any resonance. However, in birefringent crystals like GaSe different polarizations of the three waves involved in DFG feel different refractive indices, making $\Delta k = 0$ possible.

GaSe is a uniaxial crystal and allows for two different types of phase-matching that differ in the polarization states and the effective nonlinear coefficient d [29, p. 25]:

$$\begin{aligned} \text{type-I } (eo - o \rightarrow o) : d &= d_{22}\cos(\Theta)\sin(3\Phi) \\ \text{type-II } (eo - o \rightarrow eo) : d &= d_{22}\cos^2(\Theta)\cos(3\Phi). \end{aligned} \tag{2.31}$$

Its hexagonal symmetry with its $\overline{6}$m2 point group reduces the number of non-vanishing components of d_{il} to $d_{21} = d_{16} = -d_{22}$ with the relatively large coefficient $d_{22} = 54 \pm 11$ pm/V [29, p. 169]. The effective coefficient d depends on two angles, Θ and Φ, over which phase-matching can be changed. Θ is the angle between the wave propagation vector $\mathbf{k}$ and the optical axis (z- or c-axis). Φ denotes the angle between the x-axis and the projection of $\mathbf{k}$ into the xy-plane (see Fig. 2.6(a)).

Figure 2.6(b) presents the two possible phase-matching types for GaSe. Changing between the types is done by rotating the crystal around the c-axis [30]. Note that the x- and y-axes can be distinguished crystallographically due to the hexagonal structure of the crystal. But they cannot be identified by linear optical methods in the uniaxial crystal[3]. In type-I phase-matching for instance an extraordinary (eo) beam of frequency

[3] Due to the distinct linear refractive index, the c-axis can be determined easily. When the crystal class and hence the effective nonlinear coefficient like Eq. (2.31) is known, the x- and y-axes can be deduced from the second-harmonic output for different angles with respect to the c-axis [31].

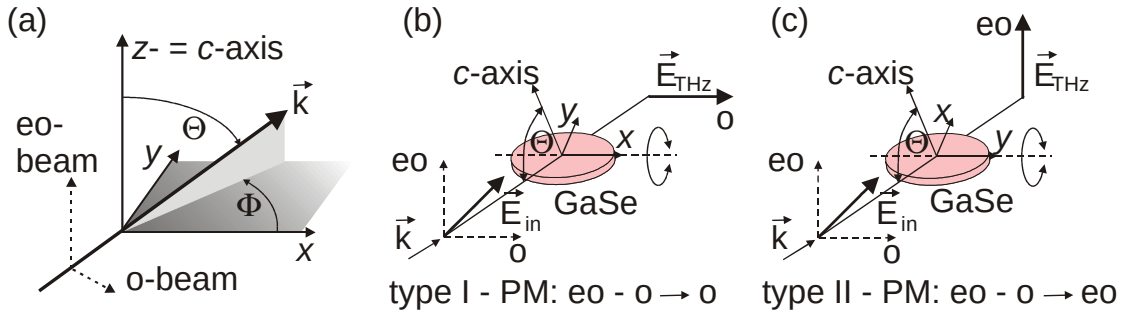

Figure 2.6.: (a) Definition of the polar coordinate system in a uniaxial birefringent crystal with the optical c-axis z. $\mathbf{k}$ is the propagation direction. The extraordinary (eo) beam is polarized in the plane formed by $\mathbf{k}$ and the c-axis, the ordinary (o) beam's polarization is perpendicular to that plane. (b) Type-I phase-matching in GaSe needs the linear polarized NIR input beam to provide ordinary and extraordinary polarization components in order to generate an o-polarized THz beam. (c) In type-II phase-matching the crystal with its hexagonal structure is rotated by 90° around the c-axis in order to give an eo-polarized THz beam.

$\omega + \Delta\omega$ mixes with an ordinary (o) one at frequency ω to generate the THz frequency $\Delta\omega$ with ordinary polarization, i.e. eo - o → o. Ordinary beams have their polarization perpendicular to the plane spanned by the c-axis and the propagation vector $\mathbf{k}$. The refractive index n_o for o-beams does not depend on Θ. Beams polarized in the plane formed by the c axis and $\mathbf{k}$, i.e. extraordinary beams, see a Θ-dependent refractive index n_eo. GaSe is negatively birefringent ($n_\mathrm{o} > n_\mathrm{eo}$). One can show that this refractive index $n_\mathrm{eo}(\omega, \Theta)$ is given by [32, sec. 14.3]

$$n_\mathrm{eo}(\omega, \Theta) = \left(\frac{\sin^2(\Theta)}{n_\mathrm{eo}^2(\omega)} + \frac{\cos^2(\Theta)}{n_\mathrm{o}^2(\omega)} \right)^{-1/2}. \tag{2.32}$$

$n_\mathrm{eo}(\omega) = \sqrt{\epsilon_\mathrm{eo}(\omega)} = n_\mathrm{eo}(\omega, \Theta = 90°)$ is the value obtained for $\Theta = 90°$ and can be found in reference [33].
Note that both phase-matching schemes require the incident NIR beam to have both ordinary and extraordinary polarization components. We employ type-II phase-matching. Also, not only two frequencies mix in the broadband NIR pulse, but all components. Hence, the total THz amplitude at a specific THz frequency $\Delta\omega$ is not given by (2.28), but by its integration over ω:

$$A_\mathrm{eo}^\mathrm{THz}(z, \Delta\omega) = \frac{(\Delta\omega)^2 d(\Theta)}{2c^2 k_\mathrm{eo}(\Delta\omega, \Theta)} \int A_\mathrm{o}(\omega) A_\mathrm{eo}^*(\omega + \Delta\omega) \left(\frac{\mathrm{e}^{\mathrm{i}\Delta k L} - 1}{\Delta k} \right) d\omega. \tag{2.33}$$

By tilting the GaSe crystal with respect to the incoming NIR beam, i.e. by changing the angle Θ, phase-matching is achieved for different THz frequencies which results in a tunable center frequency.

3. Spectroscopy tools

Terahertz spectroscopy has become a powerful tool to investigate low-energy excitations in matter. The experiments described in this thesis work employ different experimental setups that shall be explained in the following sections: a broadband THz setup for probing excitations up to 40 THz (7.5 μm, 165 meV), a strong infrared light source which is the Rossendorf free-electron laser FELBE covering 1 to 75 THz (4-280 μm, 4-310 meV), and a near-infrared time-resolved streak camera spectroscopy system. Whereas the Fano signature in the intersubband THz response of a multiple quantum well is measured using the broadband THz setup (chapter 4), the free-electron laser and the streak camera are used to investigate THz sidebands and Autler-Townes splitting (chapters 5 and 6, respectively).

3.1. Introduction

The THz spectral region (0.3-30 THz) covers a lot of interesting and also technologically important excitations in condensed matter systems [2, 13, 34]. In this region lattice vibrations have resonances [35] and vibrational and rotational transitions in molecules characterize chemical and biological compounds. For instance, the CO_2 vibrational transition, where the CO_2 laser is based on, lies at 10.6 μm. Also explosives reveal their spectral fingerprints which can become important in security applications [36]. As already mentioned, intersubband and excitonic transitions in confined semiconductor heterostructures occur in the THz range [3, 8, 24], and are the topic of this thesis. This region can be investigated by standard Fourier transform infrared (FTIR) spectroscopy [37]. Here, the light from an incoherent blackbody-radiation source, like a globar, is split in a Michelson interferometer and brought to interference on a detector that measures the intensity with respect to the optical path difference. The Fourier transform leads to the spectrum. However, no phase information about the electric fields is obtained. Additionally, FTIR spectroscopy gives no time resolution and has a low power incoherent THz source.
During the last decades, efficient sources and detectors for the THz region have been developed. Below approximately 5 THz large area photoconductive Hertzian dipole antennas [38, 39] are used that have developed from the concept of photoconductive switches [14]. They are pumped by short-pulsed (approx. $\leq$ 100 fs) lasers with several MHz repetition rates and are taken for field-resolved detection as well [40]. However,

free-space electro-optic sampling using nonlinear crystals like ZnTe is the standard detection scheme [41, 42].
Higher frequencies can be obtained by phase-matched difference-frequency generation (DFG) using two different wavelengths, for example the signal and idler wave of an optical parametric oscillator pumped by a high-power Ti:sapphire laser. Using $AgGaS_2$ or GaSe nonlinear crystals a wide tuning range of 5 to 18 μm at 76 MHz repetition rate and 2 mW average power has been reported [43]. Recently, two optic parametric amplifiers pumped by the same 1 kHz Ti:sapphire amplifier reached THz fields exceeding 100 MV/cm with a broad tunability from 10 to 72 THz exploiting DFG in GaSe and $AgGaS_2$ crystals [44]. However, such relatively complicated schemes rely on high-power lasers and combine several stages of nonlinear frequency conversion decreasing the signal-to-noise ratio.
A simpler method to generate frequencies above 5 THz is optical rectification in GaAs within individual ultrashort 15 fs NIR pulses [45]. Broadband THz pulses are measured with frequencies up to 30 THz and pulse lengths of 40 fs. But since the nonlinear process is not phase-matched, only the surface emits THz radiation which makes this process inefficient. Two orders of magnitude higher THz power is achieved with phase-matched difference-frequency mixing within ultrashort NIR pulses in birefringent nonlinear crystals like GaSe [46, 47]. Average powers of a few μW are measured at MHz repetition rates. The spectra are broadband and tunable up to 40 THz. Large angles of incidence prevent to reach higher frequencies. By using another material, $LiIO_3$, ultrabroadband 50-130 THz pulses could be demonstrated recently with a 1 kHz amplifier [48].
For detection of those high frequencies up to 40 THz standard electro-optic sampling can be employed, but with a very thin (10 μm) ZnTe crystal as detector [15]. Phase-matched detection in GaSe is more efficient here [30, 49].
Another candidate for THz generation are quantum cascade lasers [1, 50] that consist of a complex, specially designed layered structure of semiconductor quantum wells and superlattices. However, they are designed for each individual wavelength and show limited tunability. Moreover, they do not deliver ps pulses.
Whereas the THz sources mentioned before are table-top systems, the free-electron laser [16, 51, 52] is a large and very complicated facility, but it can deliver high-power pulses in a broad wavelength range.

3.2. Broadband terahertz setup

Here, we introduce our THz setup and summarize its characteristics. For a more comprehensive treatment see also references [53, 54].
Figure 3.1(a) recapitulates the basic concept of THz generation: all frequency components within a single broadband near-infrared laser pulse are mixed via phase-matched DFG to give rise to THz emission. The process has been discussed in more detail in the preceding chapter. However, we see already that a broadband NIR high-power laser is required to obtain a large THz tunability and high output power.

Ti:sapphire laser oscillator

Today broadband and thereby ultrashort pulse laser oscillators are based on Ti:sapphire (Titanium-doped sapphire, Ti^{3+}:Al_2O_3) as gain medium. Pulses as short as 3.8 fs could be demonstrated [55] and sub 7 fs systems are commercially available nowadays. In Ti:sapphire lasers short pulse generation is possible due to the broad flourescence bandwidth (670-1070 nm) and passive mode locking via the nonlinear optical Kerr lens effect directly in the gain medium. The Kerr effect is an intensity-dependent self-focusing of the laser beam. Starting from an intensity fluctuation (from noise or a perturbation) the formerly continuous wave (cw) beam develops spikes with higher intensities that undergo a self-focusing. This leads to a better overlap with the pump beam for pulses compared to the cw contribution. Hence, high-intensity short pulses undergo more gain and thereby a pulsed operation is favored.
We use a *Femtolasers: Femtosource Scientific sPro* laser oscillator, installed in 2000. It is optically pumped at 532 nm by a cw 5 W Nd:YVO_4 laser (*Coherent: Verdi V5*). Dispersion introduced by the Ti:sapphire crystal and the air in the cavity is compensated by several mirrors with negative dispersion inside and outside the oscillator. The oscillator output coupler is attached to a piezo-drive and placed on a motorized linear translation stage. Both are controlled by a feedback loop (*Femtolasers: Femtolock*) for active synchronization of the repetition rate to an external reference frequency. The laser repetition rate is 78 MHz. While the power spectrum is centered at around 800 nm at a FWHM of typically 105 to 115 nm (see Fig. 3.1(b)), the pulses can be as short as 11 fs. The average output power is approximately 400 mW.
Note that the spectral width of the NIR laser spectrum limits the highest achievable THz frequencies, in our case 48 THz. The low-frequency side is limited by the GaSe reststrahlen band at around 7.5 THz [56]. Below the reststrahlen band DFG is again

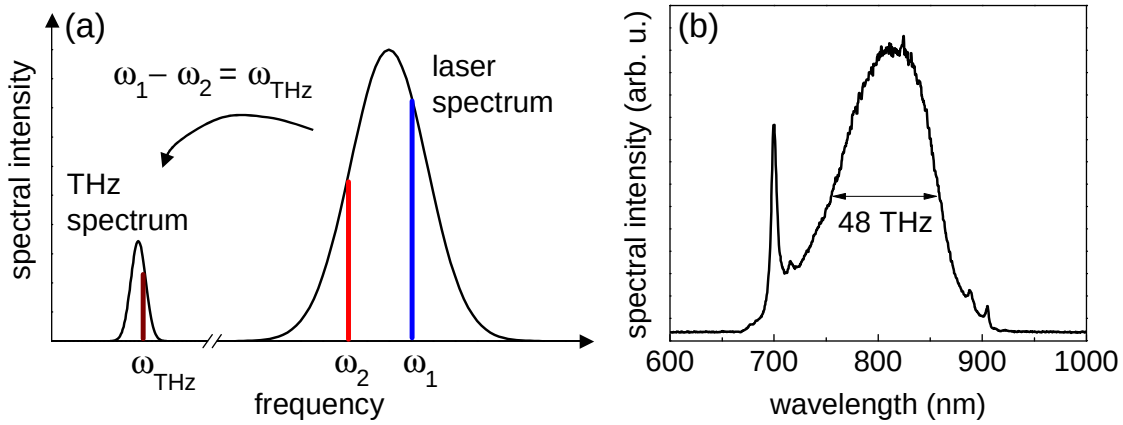

Figure 3.1.: (a) Scheme for difference-frequency mixing of two optical frequencies ω_1 and ω_2 in the laser spectrum to obtain the THz frequency ω_{THz}. (b) Broadband fs laser spectrum with a FWHM of 105 nm. At 700 nm a cw line from spontaneous emission appears, but does not contribute to THz generation.

possible [57]. We employ GaSe as THz emitter crystal because of its low absorption in the THz range [58], its high nonlinear coefficient d and its large birefringence $n_o - n_{eo}$ that allows phase-matching over a broad frequency range.

Setup

Figure 3.2(a) is a schematic view of the setup. The femtosecond laser beam is split by a 90:10 beamsplitter, using the larger part for phase-matched THz generation and the smaller one for field-resolved sampling of the THz field (to be explained later on). In the THz generation path the NIR beam is focused on a tilted 55 μm thin z-cut GaSe crystal by a gold-coated off-axis parabolic mirror with effective focal length of 11.6 cm. In order to provide simultaneously an o- and eo-polarized NIR beam for type-II phase-matched THz generation (see Fig. 2.6), a $\lambda/2$ waveplate rotates the beam polarization to 45°. The emitted THz radiation is collected, guided and refocused at a potential sample position by additional off-axis parabolic mirrors of identical focal length (11.6 cm). The transmitted NIR beam is blocked by a Si wafer. The NIR sampling beam split off from the THz generation beam goes over a mechanical delay line (*PI Physik Instrumente GmbH & Co. KG: M-410 CG*) and is overlapped with the THz beam by means of a Si wafer. Moving the delay line by a distance Δx is accompanied by a time delay of $\Delta t = 2\Delta x/c$, where c is the speed of light. Both beams then propagate collinearly and are focused by an off-axis parabolic mirror (5.8 cm focal length) on another 25 μm thin GaSe crystal whose orientation and phase-matching angle is identical to that of the first one. Note that a $\lambda/2$ waveplate in the sampling beam path rotates the NIR polarization perpendicular to the THz polarization. Finally, the NIR sampling beam is analyzed with a $\lambda/4$ waveplate, a Wollaston prism and a pair of intensity-balanced photodiodes. As explained later on in more detail the polarization state of the NIR beam is altered by the THz field within the GaSe crystal. This change is recorded as a function of the temporal delay between THz and NIR pulses that can be controlled via the delay line (*electro-optic sampling*). For a good signal-to-noise ratio a lock-in amplifier (*Stanford Research Systems: Model SR830 DSP*) is used together with a mechanical chopping of the THz beam at frequencies between 0.3 to 3 kHz. A Labview based software finally records the THz field with respect to the delay line position.
In Fig. 3.2(b) the measured field-resolved THz transient is plotted for a phase-matching angle $\Theta \approx 58°$. It reveals an intensity pulse duration of 53 fs. The corresponding power spectrum in Fig. 3.2(c) is taken from the main pulse only and has a spectral width (FWHM) of 9.6 THz. The resulting time-bandwidth product of 0.51 is close to the Fourier limit of 0.441 for Gaussian pulses. This is underlined by an almost identical phase of all the main frequency components of the THz pulse (Fig. 3.2(d)).
Typical THz pulse energies are 1 fJ for the 55 μm thin GaSe emitter [53], corresponding to field strengths at the intermediate focus of the order of 200 V/cm.
In the following we give a short characterization of the THz emission and explain the detection method in more detail.

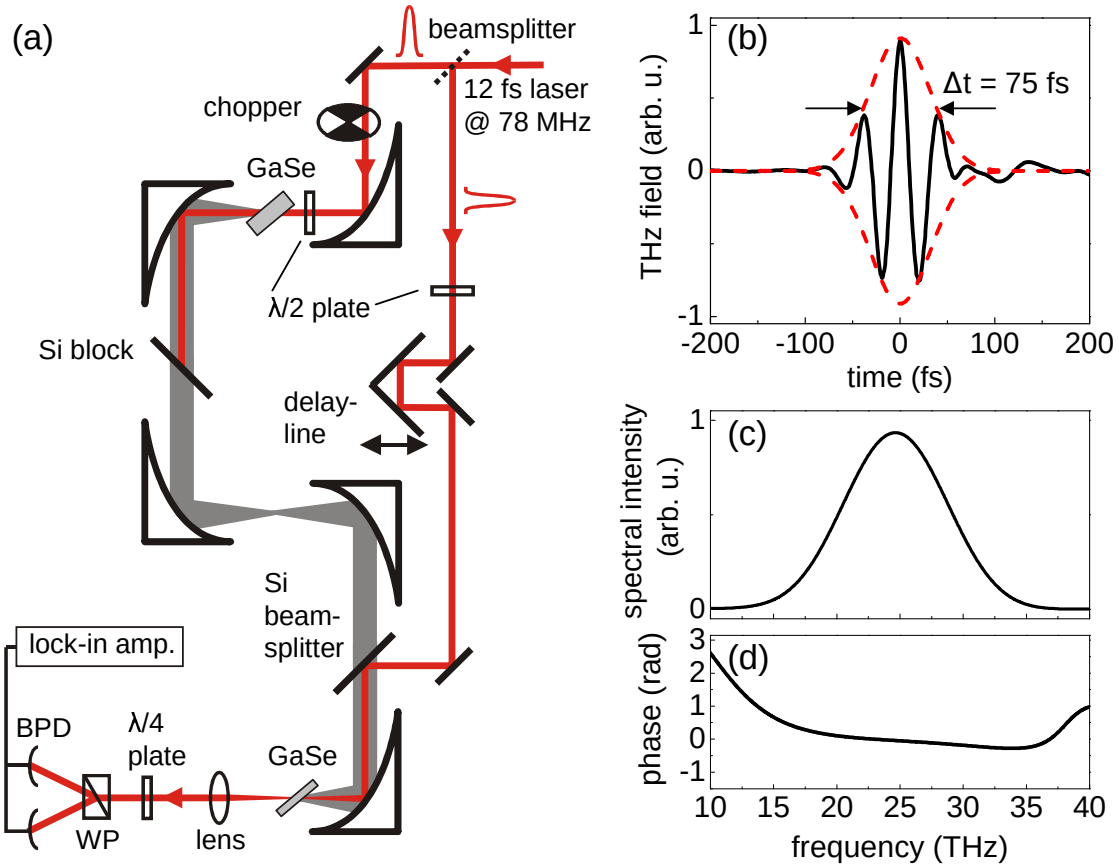

Figure 3.2.: (a) Broadband THz setup with phase-matched electro-optic sampling. The 12 fs NIR laser output is split. Nearly all intensity (90%) is transmitted and focused on a 55 μm thin GaSe crystal for phase-matched DFG. The THz radiation is sampled in a second 25 μm thin crystal via electro-optic sampling (compare Fig. 3.4, BPD: balanced photodiodes, WP: Wollaston prism). To this end the second part of the split laser beam (10 %) is used. Note that a $\lambda/2$ waveplate provides o- and eo-polarized beams for the DFG. (b) THz field (black line) from a 55 μm thin GaSe crystal measured with a 25 μm thin one. For both crystals the phase-matching angle was $\approx 58°$. The red dashed line gives the field envelope, leading to a (intensity) pulse duration of 53 fs. (c) Corresponding spectrum from the main pulse only, without the small subsequent oscillations. A time-bandwidth product of 0.51 is close to the Fourier limit of 0.441. (d) Nearly flat phase over the main frequency components.

Interferometric autocorrelation

A simple way of THz detection is to make use of a Michelson interferometer and record an autocorrelation [53, 54] which is used here to characterize the emitted THz pulses. Now the broadband fs NIR laser beam is split equally by a 50:50 beamsplitter in two beams. A $\lambda/2$ waveplate ensures that both beams provide simultaneously e- and eo-polarization that is necessary for phase-matched difference-frequency mixing. After one of the NIR beams having gone through a mechanical delay line they are both focused

on the same GaSe crystal by an off-axis parabolic mirror with an effective focal length of 11.6 cm. Both THz beams are then refocused and overlapped on a liquid-nitrogen cooled HgCdTe (Mercury-Cadmium-Telluride, MCT) detector (*Judson Technologies*)[1]. The MCT detector is connected to a lock-in amplifier while the NIR beam is chopped mechanically. By varying the time delay between the THz pulses and detecting the interference pattern of both overlapping THz pulses one can obtain the power spectrum $|E_{\mathrm{THz}}(\omega)|^2$ after Fourier transformation of this interferogram. That is the basis of FTIR spectroscopy. Note that we employ a non-collinear propagation of the THz pulses that prevents spurious effects and allows the direct retrieval of the spectrum in this linear autocorrelation [59].

In Fig. 3.3(a) the interferograms from such an autocorrelation are presented for two GaSe crystals of different thickness. Ideally, autocorrelation traces should be symmetric. In our case one of the pulses has probably seen a slightly different dispersion than the other one, i.e. the pulses are chirped differently. Both crystals are tuned to an phase-matching angle Θ of nearly 60°. One clearly notices that the thicker crystal ($l \approx 55$ μm) emits a longer pulse than the $l \approx 25$ μm thin one. Surely this results in a narrower spectrum for the thick crystal (11 THz FWHM compared to 19 THz for the thin crystal), as can be seen in Fig. 3.3(b). It directly reflects the more critical phase-matching condition for thicker crystals according to Eq. (2.29). Also the calculated spectrum is given here for both crystals (dashed lines), using Eq. (2.33). Note that the low-frequency side of the measured 25 μm GaSe spectrum is not detected entirely because of the MCT detector cut-off below 19 THz ("16 μm MCT").

In Fig. 3.3(c) the phase-matching angle Θ is varied for the 55 μm thin GaSe crystal. Good agreement between the measured (red line) and the calculated spectra (black line) evaluating Eq. (2.33) is obtained, keeping in mind the MCT detector cut-off below 12 THz in this measurement ("26 μm MCT"). At a phase-matching angle of $\Theta = 0°$ a large low-frequency and a smaller high-frequency peak can be seen, separated by a minimum at 25 THz where phase-matching is impossible at this angle. Tilting the crystal to $\Theta = 20°$ enables phase-matching for other frequency components: the peaks shift to higher frequencies and the second high-frequency one at 37 THz decreases. For $\Theta \geq 40°$ a "new" broad peak at 15 THz appears and can be tuned continuously up to 33 THz for $\Theta = 70°$. At the high-frequency side the crystal holder geometry limits the maximum achievable phase-matching angle to approximately 75°. Nevertheless, we have demonstrated an up to 11 THz FWHM broadband tunable THz source covering the spectral region between 15 to 40 THz (7.5-20 μm or 60-165 meV). Note that the maximum THz intensity can be obtained for Θ between 40° and 50° with a drop to half of this peak intensity at 35° and 60° [53]. Since the intersubband resonance of our sample lies at 27 THz we mainly use a phase-matching angle between 55° and 60°.

A drawback of this simple autocorrelation method is that it measures only the THz power spectrum, as known from FTIR spectroscopy. No information about the field

[1] Those detectors measure time-averaged THz intensities and do not see the individual THz pulses coming at 78 MHz because of their limited bandwidth of < 1 MHz. Their working principle is a photocurrent measurement of the low-bandgap MCT semiconductor compound and therefore they show a low-frequency cut-off for THz radiation below the bandgap.

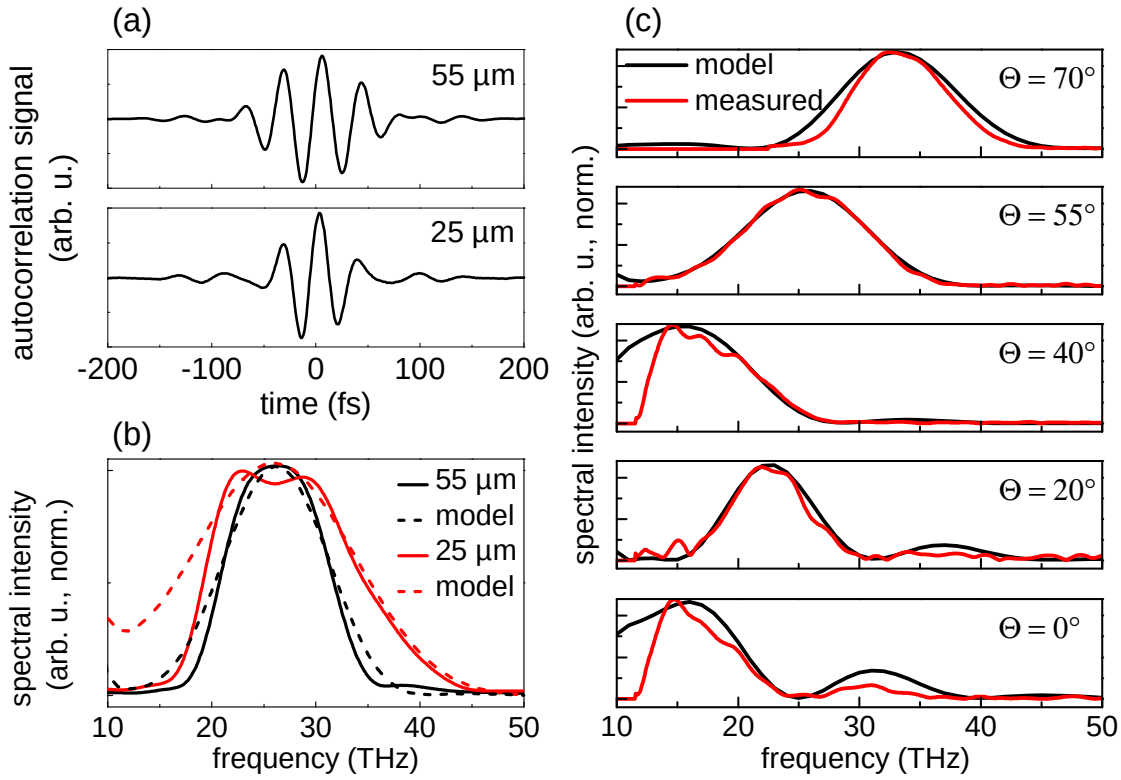

Figure 3.3.: (a) Autocorrelation for the 25 μm and 55 μm thin GaSe emitter, respectively. (b) Corresponding spectra showing a larger bandwidth for the thinner crystal. Below 19 THz the MCT detector cut-off narrows the spectrum, as can be seen by the simulated spectra (dashed lines, calculated from Eq. (2.33)). (c) The emission spectrum of the 55 μm GaSe crystal shifts with the phase-matching angle Θ. The theoretical model using Eq. (2.33) fits quite well with the measurement. Note the MCT detector cut-off below 12 THz.

and its phase is obtained. But usually only phase-sensitive THz spectroscopy gives all information to describe the sample response, since both real and imaginary part of the dielectric function can be deduced from that. For example, in the next chapter that deals with Fano signatures in the intersubband THz response of a quantum well, the intersubband absorption needs to be calculated from the Fourier transformed measured electric fields, and not from the power spectra.

Field-resolved detection via (phase-matched) electro-optic sampling

One method to detect THz pulses and resolve the THz field is a cross-correlation technique between this THz pulse and a single-cycle or at least much shorter THz pulse [60, 61]. Our previous approach [53, 54] was mainly based on this technique, where the THz pulses from the 25 μm thin GaSe crystal sampled the pulses from the 55 μm thick crystal. Looking back in Fig. 3.3(a) and (b) one notices that the prerequisite of a

much shorter sampling pulse is rather poorly fulfilled. For that reason we go to a more elegant and widely accepted detection scheme that samples the THz field directly by the 12 fs ultrashort NIR pulses. Now the sampling pulse is indeed significantly shorter than the THz pulse itself.
In the low-frequency THz range below 5 THz different non-phase-matchable detector crystals like ZnTe, GaP or polymer devices have been used in the literature [41, 42, 62–64]. ZnTe has turned out to be the best material in this spectral region [65] and for frequencies below 2 THz relatively long coherence lengths above 2 mm can be achieved [63].
We first address electro-optic sampling (EOS) in the common non-phase-matchable material ZnTe and explain its working principle. ZnTe is a zinc-blende crystal that is intrinsically not birefringent. It is used in <110> orientation. EOS is based on the Pockels effect: an electric field, in this case that of the THz transient itself, induces a birefringence in the electro-optic material and changes the index ellipsoid. This instantaneous response of the material can be probed by a linearly polarized ultrashort NIR pulse that is co-propagating collinearly with the THz pulse. Since the Pockels effect is linear in the applied electric field the THz transient is directly measured.
In Fig. 3.4 a typical experimental scheme for EOS is depicted. A linearly polarized NIR sampling beam is overlapped with a linearly polarized THz beam, for instance via a Si beamsplitter. Both beams are focused by an off-axis parabolic mirror near normal incidence on the same interaction volume of a <110>-oriented ZnTe crystal. The NIR beam can be polarized parallel or normal to the THz polarization when the THz polarization is normal to the crystal's z-axis [66]. Without THz beam a $\lambda/4$ waveplate placed behind the crystal converts the NIR polarization to a circular one that is then split by a Wollaston prisma into two perpendicularly polarized beams of equal intensity. Both beams are focused on two photodiodes. Their difference signal is balanced to zero without THz field. With THz field present the NIR sampling beam gets slightly elliptically polarized after the $\lambda/4$ waveplate, resulting in a difference signal from the

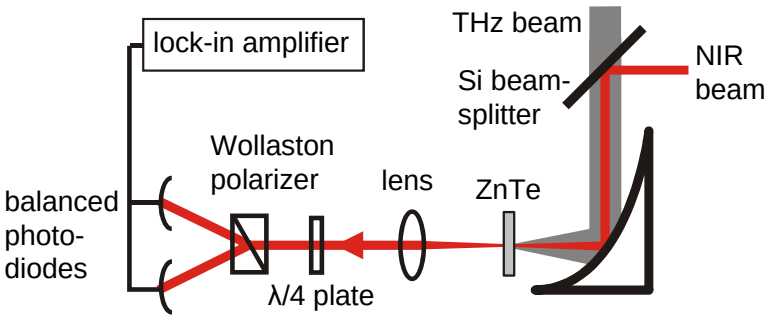

Figure 3.4.: Electro-optic sampling scheme for field-resolved THz detection. The THz electric field induces a birefringence in a ZnTe crystal. This change is probed by a linearly polarized NIR laser beam whose polarization state after the $\lambda/4$ waveplate changes from circular to elliptical with a THz field present. A Wollaston prism and two balanced photodiodes monitor the modification of the NIR polarization.

unbalanced photodiodes that is read out as a function of the temporal delay between THz pulse and NIR sampling pulse.
Now we derive a relation between the measured intensity difference signal ΔI and the phase retardation Γ of the NIR beam, i.e. the phase retardation between the two circular polarization components that produce the linear NIR polarization. For convenience we assume a linearly polarized NIR sampling beam propagating in z-direction and polarized along the x-direction: $\mathbf{E}_{\text{in}} = (E, 0)\, e^{i(\omega t - kz)}$. This field is transformed to an elliptically polarized field $\mathbf{E}_{\text{out}}$ after having passed the optical elements that is the nonlinear crystal and the $\lambda/4$ waveplate. In analogy to the Jones matrix formalism one can represent the two optical elements by matrices $\mathrm{M}(\Gamma)$ and $\mathrm{M}_{\lambda/4}$ (where $\Gamma = \pi/2$), respectively, which yields [58]:

$$\begin{aligned}
\mathbf{E}_{\text{out}} &= \frac{1}{2} M_{\lambda/4} M(\Gamma) \mathbf{E}_{\text{in}} + c.c. \\
&= \frac{1}{2}\frac{1}{\sqrt{2}} \begin{pmatrix} 1 & e^{i\frac{\pi}{2}} \\ e^{i\frac{\pi}{2}} & 1 \end{pmatrix} \begin{pmatrix} \cos\frac{\Gamma}{2} & e^{i\frac{\pi}{2}} \sin\frac{\Gamma}{2} \\ e^{i\frac{\pi}{2}} \sin\frac{\Gamma}{2} & \cos\frac{\Gamma}{2} \end{pmatrix} \mathbf{E}_{\text{in}} + c.c. \\
&= \frac{1}{2}\frac{E}{\sqrt{2}} \begin{pmatrix} \cos\frac{\Gamma}{2} - \sin\frac{\Gamma}{2} \\ e^{i\frac{\pi}{2}} \left(\cos\frac{\Gamma}{2} + \sin\frac{\Gamma}{2}\right) \end{pmatrix} e^{i(\omega t - kz)} + c.c. = \begin{pmatrix} E^x_{\text{out}} \\ E^y_{\text{out}} \end{pmatrix}. \qquad (3.1)
\end{aligned}$$

The time-averaged intensity difference signal ΔI from the photodiodes reads:

$$\begin{aligned}
\Delta I &= \lim_{T\to\infty} \frac{1}{T} \int_0^T (E^y_{\text{out}})^2 - (E^x_{\text{out}})^2 dt \\
&= \frac{E^2}{2} \left[\left(\cos\frac{\Gamma}{2} + \sin\frac{\Gamma}{2} \right)^2 - \left(\cos\frac{\Gamma}{2} - \sin\frac{\Gamma}{2} \right)^2 \right] \\
&= E^2 \sin\Gamma \approx I \cdot \Gamma. \qquad (3.2)
\end{aligned}$$

In the last line we used $\sin\Gamma \approx \Gamma$ for small Γ. Using a <110>-oriented ZnTe detector, Γ is connected to the THz electric field via [66]:

$$E_{\text{THz}} = \frac{\lambda_{\text{NIR}}}{2\pi n^3_{\text{NIR}} r_{41} l} \Gamma, \qquad (3.3)$$

with the electro-optic coefficient $r_{41} = 3.9$ pm/V and the crystal length l.

In order to extend the field-resolved detection bandwidth up to 40 THz, very thin ZnTe crystals are necessary with a thickness of $l \approx 10$ μm [15]. In thicker crystals phase-matching cannot be achieved over such a broadband range which is why the measured THz response has to be corrected due to a phase-mismatch between THz phase velocity and the NIR sampling pulse group velocity [67]. On the other hand thin crystals are hard to produce, are fragile and the sensitivity decreases with the decreasing interaction length.
We can overcome this drawback by using GaSe also as detector [30, 49, 68], as has already been shown in the schematic layout of our setup (Fig. 3.2(a)). The advantage is that it is phase-matchable and hence thicker crystals can be used. Its electro-optic

coefficient $r_{22} = 14.4$ pm/V [29] is also larger than that of ZnTe. The detection principle may be interpreted as the inversion of the generation process [68], which means type-II phase-matched sum-frequency generation. Going back to Fig. 2.6(c) (page 15) the geometry is the following. The ordinarily polarized NIR probe beam interacts with the extraordinarily polarized THz beam to generate an NIR beam at the sum-frequency with extraordinary polarization. This component modifies the overall polarization state after phase-sensitive superposition with the transmitted NIR probe beam. Since the amplitude of the sum-frequency signal is proportional to the THz field amplitude, the polarization change is also proportional to the THz field. Therefore, this scheme is similar to standard field-resolved electro-optic sampling. However, due to the birefringence of GaSe, the detection efficiency can be increased by tilting the crystal according to the appropriate phase-matching angle Θ. Consequently, the detection crystal is used with a similar phase-matching angle as the emitter crystal. One also has to assure that the detection bandwidth is larger than the emission bandwidth. This is the case when detecting with the 25 μm thin crystal while the THz emission comes from the 55 μm thick GaSe (see Fig. 3.3(b)).

THz emission based on a large-area photoconductive antenna

For our sample characterization, i.e. for revealing the intraexcitonic $1s$-$2p$ transition later on, a THz probe scheme in the 1-5 THz region is also required. We employ a planar large-area photoconducting THz antenna that delivers electric field strengths up to 1 kV/cm [38, 39]. It replaces the GaSe emitter in the NIR laser focus in Fig. 3.2(a). Due to pronounced water vapor absorption in this spectral region the setup is purged with gaseous nitrogen. THz detection is based on EOS in ZnTe (see Fig. 3.4). The antenna consists of several interdigitated finger-like electrodes placed on semi-insulating GaAs substrate, as can be seen in the schematic drawing of Fig. 3.5(a). A voltage[2] is applied at the electrodes in such a way that every second electrode is on the same potential, and the electrodes between them are at another potential. Thus, the electric field is reversed between two adjacent periods. Every second period is shadowed with a metallization isolated from the electrodes. Hence, charge carriers are photogenerated across the GaAs bandgap by the pulsed fs NIR laser only in every second period where the electric field is unidirectional. Those photoexcited carriers are accelerated and the emitted THz radiation interferes constructively. Due to ZnTe phonons the THz emission is limited to a range below 4 THz which can be seen in Fig. 3.5(b). The various dips in the spectrum come from water vapor absorption. Detection below 1 THz is restricted due to large opening angles for low frequency components of the THz antenna [40].
So far we have demonstrated broadband THz generation and coherent detection and will now come to another source of THz pulses, the free-electron laser.

[2] Here, the antenna was biased with a square wave with ± 20 V maximum voltage and 50% duty-cycle at 10 kHz. The average optical excitation power was 100 mW.

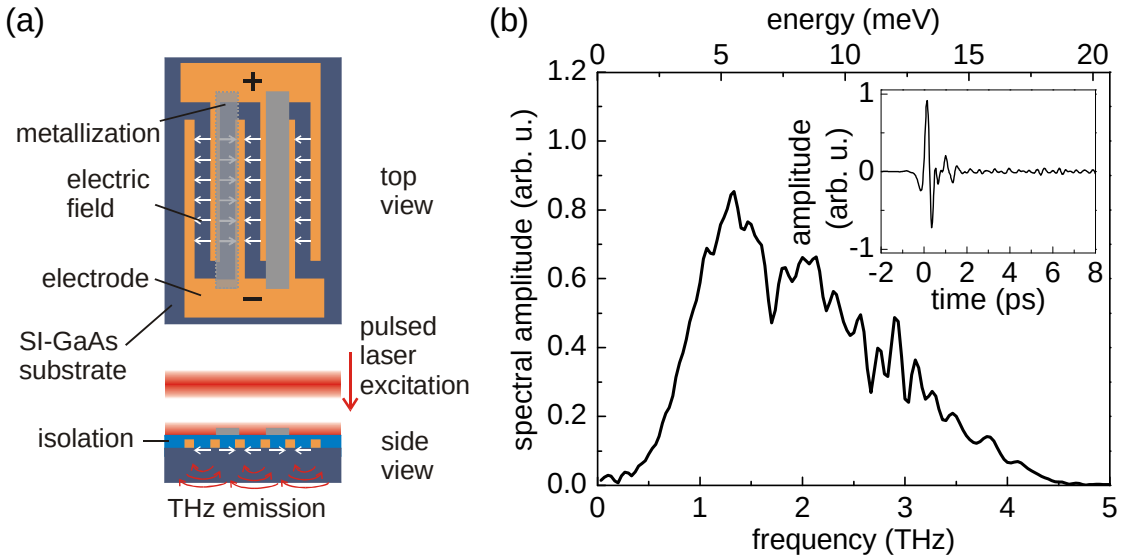

Figure 3.5.: (a) Schematic layout of the large-area photoconductive antenna, driven by a fs pulsed laser. (b) Spectrum after Fourier transformation of the time transient (see inset) recorded via electro-optic sampling in a 40 μm thin <110>-oriented ZnTe crystal. The pronounced dip at 1.7 THz is due to water absorption despite purging of the setup with gaseous nitrogen.

3.3. Free-electron laser

In this thesis we will not only investigate the THz response in the low-field regime with the table-top systems described before. We also make use of the Rossendorf free-electron laser (FEL) FELBE [69]. It serves as a strong THz source in the infrared spectral region for our experiments concerning sideband generation and Autler-Townes splitting. FELBE covers a wavelength range from 4 to 280 μm. However, the main advantage of FELBE compared to most of the other FELs is the quasi continuous wave operation, making it possible to deliver 1-25 ps long pulses with average powers up to 20 W (wavelength-dependent) at a repetition rate of 13 MHz. The high repetition rate results in superior signal-to-noise ratios [8] and also allows for synchronization to 78 MHz table-top lasers for two-color experiments [70].
State-of-the-art accelerators are essential for operating an FEL. The heart of FELBE is the thermionic electron gun and the two superconducting high-frequency 20 MeV linear accelerators, providing a high average beam current of 1 mA in $<$ 10 ps short pulses at a low energy spread and a superior beam brilliance. This high-quality electron beam itself can be used for experiments to generate neutrons, positrons, bremsstrahlung and X-rays. Or, together with two independent FELs, U27 and U100, it can also serve as source for infrared radiation. While in conventional lasers the lasing process is confined to a particular transition in an atom or a molecule, for instance in a Ti:sapphire laser crystal or the vibrational molecular transition in a CO_2 laser, the gain medium in

an FEL consists of the electron beam in a magnetic field. This allows a wide tuning range that is in principle only limited by the electron accelerator technology. Since the electron beam can carry a huge energy also very high radiation intensities can be achieved without destroying the laser gain medium due to losses like in conventional solid state lasers, for instance.
We will now briefly describe the operation principle of an FEL [71],[72, ch. 9], [73, sec. 13.13] and will also demonstrate electro-optic sampling of FEL pulses. A thorough characterization of FELBE can be found in [54, 69, 74, 75].

Working principle

A schematic view of a free-electron laser is presented in Fig. 3.6. Electron bunches emitted from a gun are accelerated to relativistic energies and are fed into a planar arrangement of magnets. This so-called *undulator*[3] provides a periodic alternating magnetic field with a period of λ_u. Electrons passing through that undulator field experience a Lorentz force that results in an oscillating motion in the transverse direction. As accelerated charges they spontaneously emit infrared synchrotron radiation in a narrow cone in forward direction because of the relativistic electron energies. The electron bunch travels along the undulator axis with its emitted radiation pulse. Both have a length of only ≈ 1 mm. While the electron pulses are extracted after the undulator the radiation pulses are kept in an optical cavity composed of two mirrors. The mirror distance is 11.53 m at FELBE, corresponding to a pulse round-trip frequency of 13 MHz that is identical to the electron bunch repetition rate. Analogous to a conventional laser this cavity provides a feedback between radiation and laser gain medium. Hence, the initially spontaneous emission interacts with the next electron bunches, leading to stimulated emission, optical gain and amplification. Finally a part of the radiation is coupled out through a hole in one cavity mirror[4]. Note that the U100 cavity has an additional parallel-plate waveguide going from the undulator to a cylindrical shaped cavity end mirror on the right hand side of Fig. 3.6. It is necessary since the mode would be too large inside the undulator and gain would be decreased. Thus, the waveguide compresses the optical mode vertically, resulting in increased gain and allowing smaller undulator gaps [69].
The emitted wavelength λ_0 depends on the undulator parameters, i.e. the magnetic field amplitude B and the undulator period λ_u, and on the relativistic energy of the electrons $\gamma m_0 c^2$ with the electron rest mass m_0, the vacuum speed of light c and $\gamma = (1 - (\frac{v}{c})^2)^{-\frac{1}{2}}$. It can be demonstrated [72, p. 271], [73, p. 449] that λ_0 reads

$$\lambda_0 = \frac{\lambda_u}{2\gamma^2}\left(1 + \frac{K^2}{2}\right), \tag{3.4}$$

[3] The U27 undulator for the wavelength range 4-22 μm consists of two times 34 periods with $\lambda_u = 27.3$ mm. The long wavelength (18-280 μm) U100 undulator has 38 periods with $\lambda_u = 100$ mm.
[4] For instance a 7 mm hole is used at a wavelength of 200 μm.

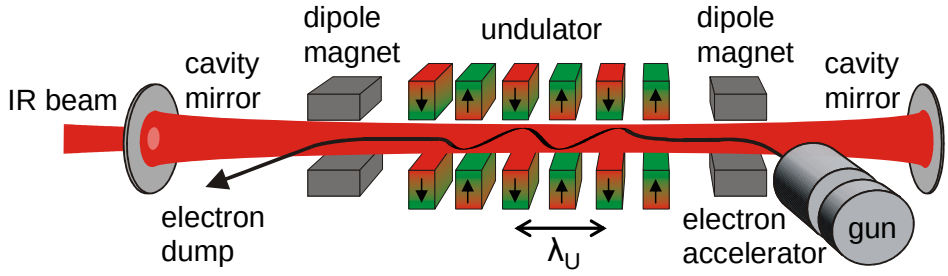

Figure 3.6.: Schematic view of a free-electron laser. A pulsed electron beam from a thermionic gun is accelerated to relativistic energies and fed into the undulator by a dipole magnet. The undulator is a periodic arrangement of magnets that give rise to a magnetic field in the electron beam path that changes its direction every $\lambda_u/2$. The electrons flying through the undulator perform an oscillating motion in transverse direction caused by the Lorentz force. Behind the undulator they are extracted to a beam dump. The wiggling motion of the electron bunches leads to synchrotron radiation that is confined in a cavity made from two mirrors. The radiation interacts with successive electron bunches and is amplified. A small part of the infrared radiation is coupled out through a hole in one cavity mirror. Be aware that the wiggling motion is exaggerated for clarity.

where the dimensionless undulator parameter K is given by

$$K = \frac{\lambda_u e B}{2\pi m_0 c}. \tag{3.5}$$

Obviously, the emission wavelength can be tuned over a broad range by variation of the electron energy and the magnetic field. The latter one is varied by altering the undulator gap, i.e. the distance between the two rows of magnets in the undulator.
Equation (3.4) also defines a *resonance energy* γ_r for a given wavelength λ_0. This terminology comes from the fact that a single electron at this energy in its moving coordinate system sees the undulator period and the period of a present coherent electromagnetic wave with wavelength λ_0 to be equal [73, p. 449]. It can be shown [76, p. 237] that the electron bunch at energy γ_r falls behind the electromagnetic wave by a wavelength λ_0 every undulator period λ_u.
When the phase between light field and transverse oscillating motion of the electron is zero, i.e. the electron transverse motion is in the electric field direction, the electron is decelerated in this direction and loses energy to the light field. This corresponds to stimulated emission. At a phase difference of π the electron absorbs energy from the wave. Going from a single electron to a bunch of electrons that is injected in the undulator, one expects a random phase, leading to neither absorption nor stimulated emission with a net gain of zero [73, p. 450]. However, when the electrons lose energy (stimulated emission) or gain energy (absorption) they are slowed down or accelerated longitudinally, respectively, because their wiggle amplitude is a function of the longitudinal velocity. Thus, a redistribution in the longitudinal direction occurs and the initial macroscopic electron bunch gets fragmented microscopically in narrow bunches spaced by one optical wavelength λ_0 [71, p. 15]. At the resonance energy γ_r this *microbunching effect* does not lead to net gain either, although the microbunch spacing

of λ_0 would lead to constructive interference and coherent emission. But for energies slighly larger than γ_r net gain is achieved (*positive detuning*) [73, p. 461 *ff.*]. Hence, a free-electron laser has to be operated slightly above the resonance energy.
Since the electron bunch continuously slips back with respect to the optical pulse by the optical wavelength λ_0 per undulator period λ_u, there might be a significant loss of overlap between electron and light pulses on their transit through the undulator, depending on the electron bunch length. If the electron pulse length is smaller than the slippage length that is the number of undulator periods times λ_0, the optical pulse does not overlap with the electron bunch over the entire undulator length and gain is reduced [77, 78][5]. In any case, the front of the optical pulse gets amplified by the free electrons only at the beginning of the undulator, while its trailing edge is amplified over a longer distance. Since the optical pulse performs several round-trips this *slippage effect* accumulates, resulting in an asymmetric amplification of the rear of the optical pulse. Consequently, the effective optical group velocity is smaller than its vacuum value, decreasing the overlap and gain (known as *laser lethargy*). This can be overcome by reducing the cavity length slightly (*cavity length detuning*), leading to an improved microbunching and a uniform growth of the optical pulse that develops into a stable shape [79].

FEL characteristics

Previous studies demonstrated that both undulators of FELBE deliver optical pulses which are very close to the Fourier limit, making it possible to estimate the actual pulse width from the measured power spectrum with an error smaller than 15% [54]. The pulse length has been extracted from a second-order autocorrelation. This technique (see Fig. 3.7(a)) is based on second-harmonic generation (SHG) in a nonlinear crystal that is chosen wavelength-dependent (for instance a non-birefringent CdTe crystal for 11 μm) [80]. Two FEL pulses that were split from one single initial pulse by a beamsplitter are focused non-collinearly on the same spot on such a crystal. While one pulse is delayed with respect to the other, the transmitted SHG signal is recorded by a suitable detector. Figure 3.7(b) illustrates such an autocorrelation trace for an FEL wavelength of 11 μm, a CdTe crystal and an MCT detector with a cut-off wavelength of ≈ 5 μm (*Judson Technologies*). Note that this detector automatically filters the original beams. The corresponding power spectrum taken by a grating spectrometer [74] is shown in Fig. 3.7(c). The resulting time-bandwidth product of $\tau_{\mathrm{pulse}}\Delta\nu = (2.2/\sqrt{2}) \times 0.27 \approx 0.42$ is very close to the Fourier limit of 0.441 for Gaussian pulses[6]. The typical relative bandwidth $\Delta\lambda/\lambda$ is 1-2%. For the long wavelength U100 undulator this results in pulse lengths of the order of 10-25 ps.

[5] This effect becomes more critical at longer optical wavelengths. For instance, at $\lambda_0 = 200$ μm the slippage length at the end of the U100 undulator is 38×200 μm $= 7.6$ mm, much longer than the electron bunch length of the order of 1 mm.

[6] The second-order autocorrelation FWHM is $\sqrt{2}$-times the real pulse width for an ideal Gaussian pulse.

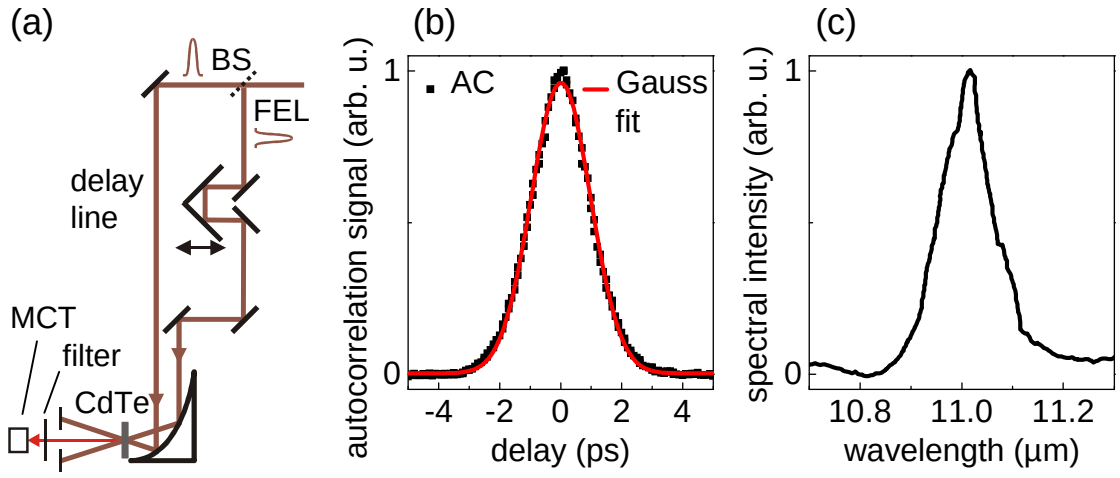

Figure 3.7.: (a) Autocorrelation setup where a mylar beamsplitter (BS) splits the FEL beam in two parts that are focused on a CdTe crystal. While one beam is temporally delayed with respect to the other one, the second-harmonic signal is recorded by an MCT detector. The original beams are blocked or filtered out. (b) Measured autocorrelation trace (AC, black dots) and Gauss fit (red line) for an FEL wavelength of 11 μm. The autocorrelation FWHM is 2.2 ps. (c) The corresponding FEL spectrum from a grating spectrometer has a width of 0.11 μm (FWHM). The resulting time-bandwidth product of 0.42 is close to the Fourier-limit for Gaussian pulses.

In Fig. 3.8(a) the FEL output power is plotted with respect to the detuning, i.e. shortening of the cavity in the region where the FEL is lasing[7]. The power decreases for a decreasing cavity length because the interaction time between the optical pulses and the gain medium shortens before the optical pulses are driven away completely from the electron bunches in successive cavity round-trips. The autocorrelation trace from Fig. 3.7(b) has been recorded near the maximum of the detuning curve. It is known that the infrared pulse duration increases with an increasing negative detuning as a consequence of the reduced overlap with the electron bunches [81]. The time-bandwidth product stays nearly constant so that the spectral width gets narrower [54]. Also the pulse shape changes distinctly and develops an asymmetry away from an ideal Gaussian shape. This is hard to see with an autocorrelation technique [54] since an autocorrelation trace involves two identical pulses and is therefore symmetric. The real pulse structure cannot be retrieved unambiguously. However, electro-optic sampling (see section 3.2) cannot only measure the intensity profile, but also the electric field of the FEL pulses [81]. Field-resolved EOS requires a very fast measurement in order to prevent the synchronization jitter between the FEL and the NIR sampling laser to average and wash out the field structure. The feasibility has been shown by detuning

[7] Note that the zero position of the detuning is set to the maximum FEL power while for positive detunings the power drops rapidly and lasing stops within 2-3 μm. An absolute value to which extent the cavity is tuned away from the ideal 13 MHz round-trip frequency can only be estimated. It is expected that the maximum saturated laser intensity occurs at a $\approx 0.2\lambda_0$ shorter cavity than the synchronous value [77].

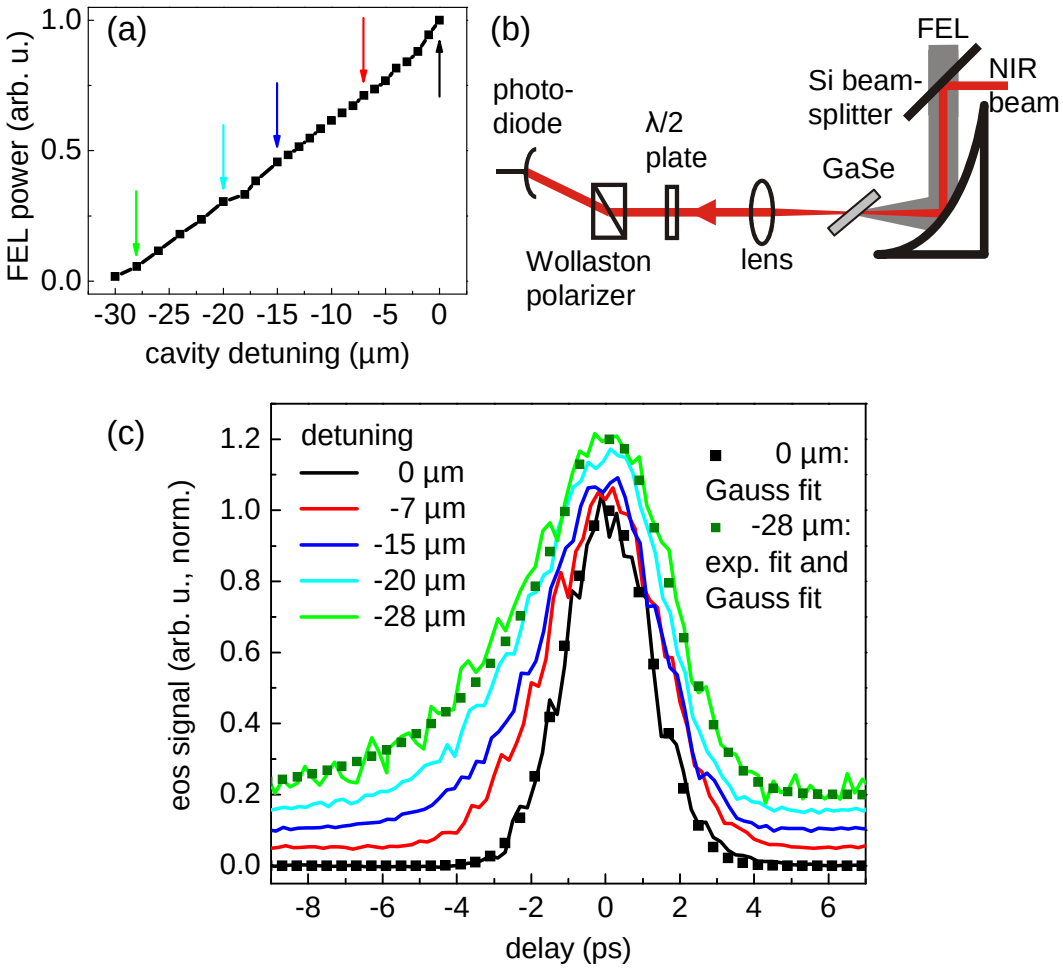

Figure 3.8.: (a) Cavity detuning curve for an FEL wavelength of 11 μm. Shortening the cavity decreases the FEL output power. (b) Intensity electro-optic sampling scheme for FEL pulses. Without FEL the Wollaston polarizer blocks the NIR sampling beam. Under FEL illumination the NIR polarization is changed, leading to a signal on the photodiode. (c) Normalized intensity EOS traces obtained with a 55 μm thin GaSe crystal for different detunings (as indicated by the colored arrows in panel (a)). The curves are offset in vertical direction for clarity. While at zero detuning (black line) the profile is Gaussian (black dotted fit), the pulse gets asymmetric to larger detunings and develops an exponentially rising edge with a Gaussian-like trailing edge (measured green line and green dotted fit).

the repetition rate of the synchronized FEL and NIR lasers, so that the NIR sampling pulse sweeps over the entire FEL pulse within a few μs while probing the FEL field [81]. However, here we will only demonstrate how to obtain the intensity envelope.
The experimental scheme for intensity EOS is given in Fig. 3.8(b). Analogously to field-resolved EOS (see Fig. 3.4) the THz beam and the NIR sampling beam are focused and overlapped on a nonlinear crystal. At a wavelength of 11 μm we can employ GaSe for phase-matched detection, provided the crystal is tilted to the appropriate phase-matching angle for that wavelength. The $\lambda/4$ waveplate and the pair of balanced

photodiodes in the conventional EOS setup is replaced by a $\lambda/2$ waveplate and a single photodiode. The $\lambda/2$ waveplate is rotated in such a way that the transmitted linearly polarized NIR beam is blocked by the Wollaston polarizer and the detector is balanced to zero when no FEL field is present. Under FEL illumination with a polarization perpendicular to the NIR probe polarization a type-II phase-matched sum-frequency process occurs [68] in our configuration (see Fig. 2.6(c)). The eo-polarized THz beam and the o-polarized NIR beam generate eo-polarized NIR light. This eo-polarized component is directly measured with the single photodiode, while the other polarization component is blocked. Due to the involved $\chi^{(2)}$ process the sum-frequency light intensity is proportional to the THz intensity. Consequently, the photodiode signal is proportional to the THz intensity, and not to the THz field as in field-resolved EOS with a pair of balanced photodiodes. One can also apply a formalism analogously to Eq. (3.1) (page 25) to describe the detection of the elliptical polarization after the GaSe crystal. The $\lambda/4$ matrix has to be replaced by $\mathrm{M}_{\lambda/2} = \mathrm{M}(\Gamma = \pi)$ for the $\lambda/2$ waveplate. The phase retardation Γ of the NIR beam is then related to the time-averaged NIR intensity signal Δ that is measured by the single photodiode in the following way:

$$\Delta \propto \sin^2 \frac{\Gamma}{2} \propto E_{\mathrm{THz}}^2. \tag{3.6}$$

Again, $\sin\Gamma \approx \Gamma$ for small Γ has been inserted and $\Gamma \propto E_{\mathrm{THz}}$ (from Eq. (3.3)).
The measured THz intensity envelopes for different detunings are depicted in Fig. 3.8(c) for the 55 μm thick GaSe detector crystal. As sampling beam the previously introduced 12 fs laser oscillator is used. Its motorized cavity output coupler is controlled by a synchronization unit (*Femtolasers: Femtolock*) that actively synchronizes the oscillator repetition rate to the 13 MHz FEL master clock. The measured pulse width also includes a timing jitter of the synchronization. Comparing the measured EOS FWHM of 2.6 ps for zero detuning with the FWHM pulse width of 1.5 ps from the autocorrelation trace obtained under similar FEL operation (see Fig. 3.7(b)), one finds a difference in the widths of 1.1 ps that can be attributed to this synchronization jitter. It lies within the range of 1-2 ps obtained by other experiments [54]. Note that this jitter allows us to measure only an intensity envelope and not the full trace of the squared electric field, E_{THz}^2, which is smeared out.
The intensity electro-optic sampling shows that for increasing detuning the pulse duration increases and the pulse shape gets asymmetric. At other FEL facilities an exponentially rising edge and a Gaussian shaped falling edge could be seen [81, 82]. The same is observed at FELBE. While the zero detuning curve is nicely represented by a single Gaussian with a FWHM of 2.8 ps, the -28 μm detuned curve is fitted by an exponentially rising edge (time constant 2.6 ps) for a delay $\Delta t < 0$ and a Gaussian shape for $\Delta t \geq 0$ with a FWHM of 3.6 ps.
Measuring the peak signal for different FEL powers at zero detuning has also verified that the intensity EOS goes linearly with the THz intensity (not shown). For average FEL powers above 300 mW saturation sets in. It is worth mentioning that with a 2 mm thick GaSe crystal and an average FEL power of only 0.1 mW we could still achieve a signal-to-noise ratio of 7. We could also demonstrate intensity electro-optic sampling at the FELBE U100 longer wavelengths (not shown). Here, either ZnTe [81] or GaP

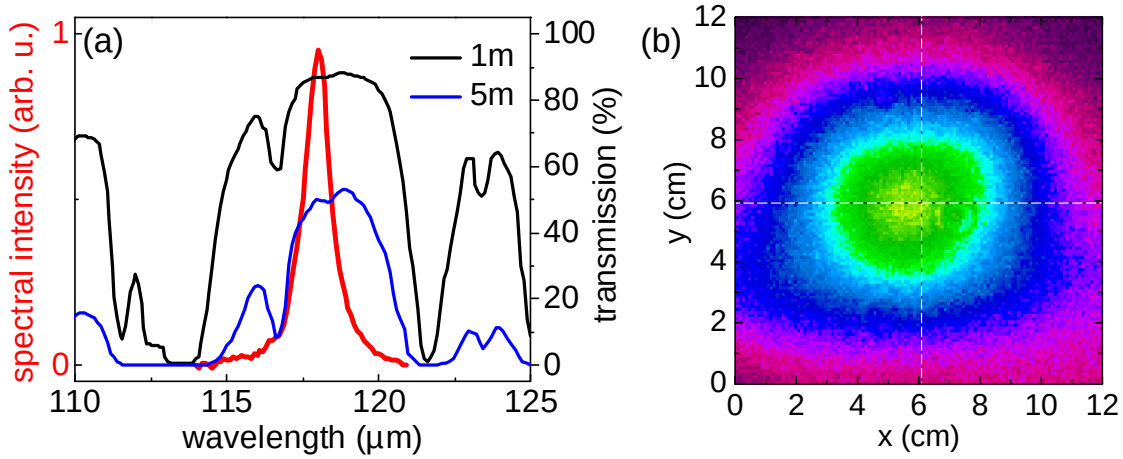

Figure 3.9.: (a) FEL power spectrum (red line) at a wavelength of 118 μm with calculated ambient air transmission for a path length of 1 m (black line) and 5 m (blue line) [83]. (b) False color image of the corresponding spatial beam profile taken with a pyroelectric camera.

[64] can be used as non-phase-matchable electro-optic crystals under normal incidence instead of GaSe whose efficiency below the reststrahlenband is poor [15].
For certain experiments involving the free-electron laser it is important to know the pulse structure, e.g. in order to estimate the pulse peak power. Also pulse replicas are not desired. But especially for the wavelengths of the U100 undulator pulse distortions, replicas and a pulse lengthening can occur due to pronounced water absorption in ambient air. The beamline from the undulator to the optical laboratories is purged with nitrogen gas. Also parts of the setup which is 2 m away from the FEL beamline exit can be purged with nitrogen when necessary. Nevertheless, it is crucial to choose the desired FEL wavelength within a gap between water vapor absorption lines. Figure 3.9(a) plots an FEL power spectrum at a wavelength of 118 μm (red line) surrounded by the ambient air transmission[8]. The latter one is calculated for 1 m (black line) and 5 m (blue line) transmission through air at 20°C and a relative humidity of 30%. Here, the selected FEL wavelength nicely fits in a gap with low water vapor absorption. Note that at some wavelengths, e.g. at 114 μm, even 1 m of air can absorb totally.
For our experiments the FEL pulse structure is not monitored regularly with electro-optic sampling because this is time-consuming and should be done at the same position as the "real" experiment. We rather measure the pulse structure directly at the sample in the respective experiment by using the respective experiment itself. The effect under investigation, i.e. sideband generation as well as Autler-Townes splitting are investigated at the temporal overlap of the FEL and NIR laser pulses, allowing us to sample the FEL pulse structure quasi in-situ by changing the temporal delay.

[8] Data digitalized with permission from [83] where the calculation was done based on the HITRAN database and the LINEFIT model [84].

Spatial FEL beam profile

Not only the temporal, but also the spatial profile is important. A good spatial profile allows a symmetric focusing. The mode profile at the wavelength of 118 μm is shown in a false color image in Fig. 3.9(b). An almost ideal Gaussian mode has been obtained. Note that the spatial mode structure is also strongly affected by water vapor absorption. This picture has been recorded with a pyroelectric camera (*Spiricon Pyrocam III*) consisting of a 12.4×12.4 mm^2 large array of 0.1×0.1 mm^2 small pixels.
To conclude, the FEL is a unique THz radiation source that enables high intensity studies with a picosecond time resolution in the broad 4-280 μm spectral range.

3.4. Streak camera

Since our streak camera setup is employed in this thesis for the first time we would like to give a short description of this valuable spectroscopy tool. Nowadays, streak cameras with a time resolution down to 0.2 ps are available. Combined with a grating spectrometer they allow for time-resolved spectroscopy in a broad range of applications, including photoluminescence, photochemistry and laser ablation [85].
The schematic layout of our streak camera setup is plotted in Fig. 3.10(a). A lens focusses the light to be analyzed on the entrance slit of a Czerny-Turner type grating spectrometer (*Bruker: Chromex 250is/is*) whose f-number is $f/4$. We can choose three different gratings with 100, 300 and 1200 lines/mm with a nominal resolution of 1.8 nm, 0.6 nm and 0.15 nm, respectively, for a slit width of 20 μm. The dispersed light is guided to the streak camera (*Hamamatsu: C5680-27*) where a fast, sensitive, high resolution CCD camera (*Hamamatsu: ORCA-ER C4742-95*) is attached. The timing of the streak camera is triggered by the NIR laser pulses themselves. A beamsplitter (BS) gives a portion of the laser light on a fast photodiode (PD) providing the trigger signal that can be delayed user-defined via a delay unit (*Hamamatsu: C6878*). Note that there is the possibility to attach the CCD to the monochromator exit of the spectrometer when time resolution is not required.
In Fig. 3.10(b) the working principle of the streak camera itself is explained [85]. The dispersed light pulses to be measured exhibit different intensities and temporal offset against one another. The pulses are projected onto a slit and focused onto the photocathode which is 0.15×5.4 mm^2 small and configured of several layers of metallic films. Photoelectrons are ejected proportionally to the light intensity. They are accelerated and pass a pair of sweep electrodes where a high alternating voltage is applied. The resulting electric field deflects them differently according to the point in time they enter the field (see inset). Like in a television Braun tube the electrons get separated vertically via this high-speed sweep. When they pass the following micro-channel plate (MCP) their number is multiplied by a factor of up to 10000, depending on the adjustable bias. A MCP consists of many thin glass capillaries (diameter ≥ 10 μm) whose

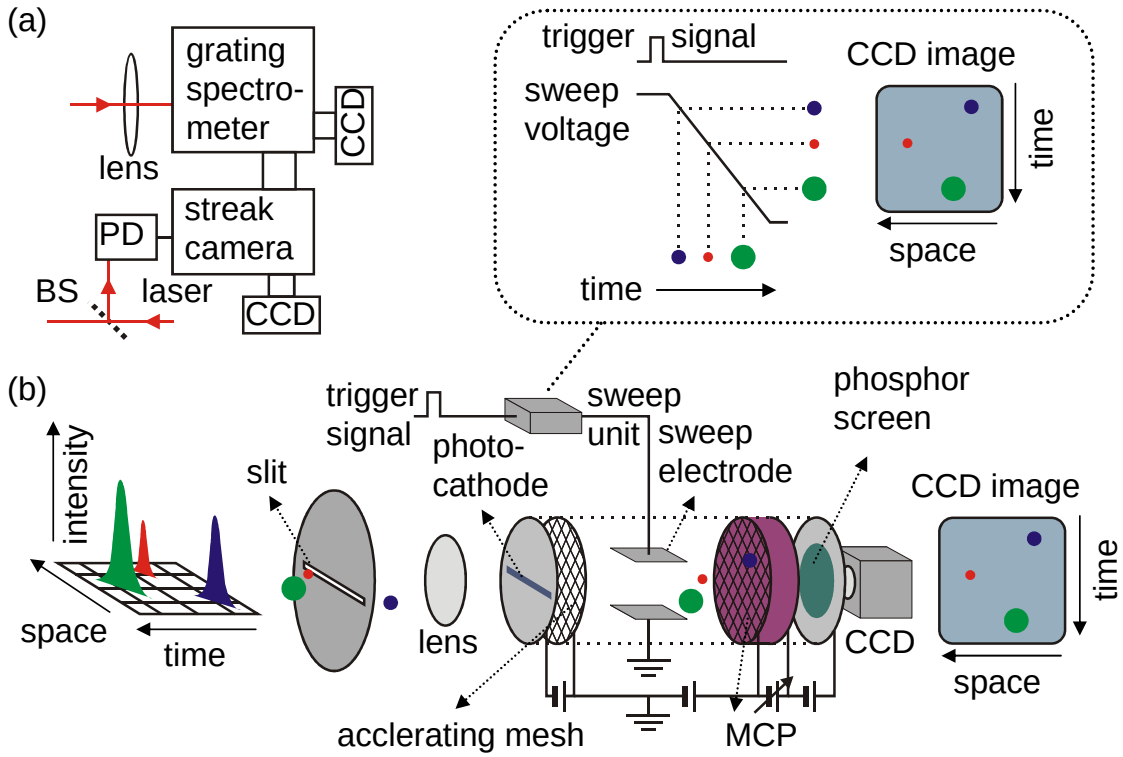

Figure 3.10.: (a) Streak camera setup. The NIR laser induced signal (e. g. a photoluminescence) to be investigated spectrally and temporally is first dispersed by a grating spectrometer and then guided to a streak camera. A CCD camera can either be attached directly to the spectrometer (for spectral resolution only) or to the streak camera. A part of the NIR laser light taken by a beamsplitter (BS) and detected via a fast photodiode (PD) serves as trigger signal. (b) Streak camera operating principle. Light pulses that have been separated horizontally in space by a grating spectrometer enter a slit and are focused on a photocathode. Photoelectrons are ejected and accelerated. They pass between two sweep electrodes where a time-dependent voltage is applied after a trigger signal. Depending on the point in time the electrons enter, the varying field deflects them differently and separates them vertically (see inset). A micro-channel plate (MCP) amplifies the number of photoelectrons. Finally they hit a phosphor screen where the resulting light emission is detected with a CCD camera. The CCD image now shows the time- and space- (i.e. wavelength-) dependent signal intensity.

internal walls are coated with a secondary electron emitting material. Finally the electrons bump against a phosphor screen where they are converted back into light that is detected by a CCD camera. On the CCD image the original light pulses appear now separated horizontally, i.e. in wavelength, and vertically, i.e. in time.
Instead of a single sweep a high-speed repeated sweep with the 78 MHz frequency of the laser oscillator is performed, using a sinewave voltage. As a result of this *synchroscan* the signal in the return sweep (say upwards) would overlap with the main sweep (downwards). When looking at temporally long signals this is not desired and can be prevented by applying a horizontal field between two plate electrodes (not shown in Fig. 3.10(b) for clarity). This *synchronous blanking* uses a sinewave voltage with a

phase difference compared to the vertical sweep signal and conducts the return sweep around the phosphor screen. Hence, only during the main sweep a signal is measured. A significant drawback of synchronous blanking are traces on the screen that are not straight, which is why our system works in synchroscan mode.
The streak camera system can be operated in the spectral range from 300 nm to 1400 nm, limited by the photocathode sensitivity. Its radiant sensitivity as photoelectric current (in mA) per 1 W of incident light is plotted in Fig. 3.11(a). Clearly, a sharp drop in sensitivity can be seen below 300 nm, and a moderate one above 1200 nm. Note the logarithmic scale. Figure 3.11(b) gives a typical quantum efficiency plot for our type of CCD camera. When attached to the streak camera this wavelength dependency is not important since the phosphor screen emits always at the same wavelength. However, it has to be taken into account when it is used directly with the spectrometer.
There are two different operating modes for the streak camera: in the "focus mode" the sweep voltage is zero and therefore only a spectrally-resolved time-integrated image is seen, whereas the "operate mode" provides additional time resolution. The latter one is divided in 4 modes with different maximum time range from 160 ps to 2.1 ns. The corresponding time resolution is $\approx$ 4 ps and 11 ps, respectively. Note that these values are accessible for daily operation using the coarse 100 lines/mm grating. However, the nominally best time resolution is 3.5 ps looking at the grating's 0th order reflection. It is also important to mention that the time resolution is strongly affected by the chosen slit widths and gratings. Narrowing the streak-camera's entrance slit in vertical direction increases the time resolution at the expense of signal intensity. While a smaller spectrometer entrance slit and a finer grating increases the spectral resolution, it decreases the time resolution since the grating is tilted against the specular reflection.
Finally, a typical streak camera false color image is displayed in Fig. 3.12. The time-integrated mode of panel (a) shows the photoluminescence (PL) of a doped self-

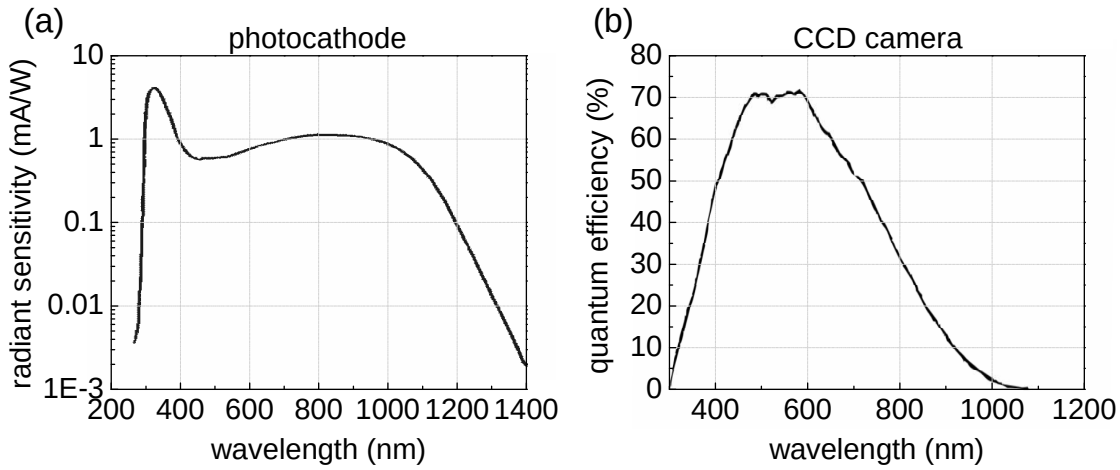

Figure 3.11.: (a) Streak tube photocathode (type: *Hamamatsu: N5716-02*) radiant sensitivity as photoelectric current per incident light power. (b) Typical CCD camera quantum efficiency for our type. [Both extracted from the Hamamatsu user manuals.]

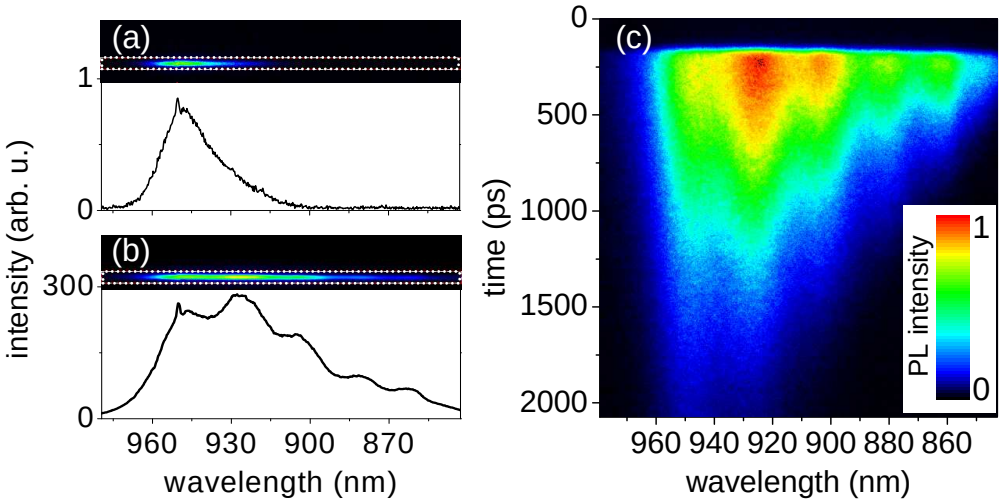

Figure 3.12.: (a) Time-integrated streak camera false color image showing quantum dot photoluminescence of the lowest energy state at 0.1 kW/cm^2 NIR excitation peak intensity. The black curve at the bottom is the integrated intensity profile calculated within the marked white dotted box. (b) Same as before for 900 times higher excitation intensity, now revealing also higher excited states. (c) Time-resolved photoluminescence. Carriers in higher excited states relax faster and also accumulate in the lowest two excited levels.

assembled InGaAs quantum dot sample (sample from reference [8], annealed at 820°C). An NIR laser at a wavelength of 806 nm delivering 2.8 ps long pulses serves as excitation source with a peak intensity of 0.1 kW/cm^2. For a better image contrast the background signal without laser illumination has been subtracted. The black curve below gives the integrated intensity within the marked white dotted box, showing the PL from the lowest energy state. When going to a high excitation peak intensity of 90 kW/cm^2 the integrated PL reveals additional equally spaced excited energy levels (panel (b)). Switching now to the time-resolved mode (panel (c)) provides further information. Carriers in higher energy states relax faster and accumulate partly in the lowest excited energy levels. Probably due to carrier heating the second lowest excited level shows the highest PL signal in the beginning, whereas PL from the lowest excited state catches up in the end when the distribution has cooled down sufficiently.
To conclude, the streak camera can provide valuable temporal information in the visible and NIR spectral region.

3.5. Sample

In this thesis we investigate an undoped GaAs/AlGaAs multiple quantum well (MQW) structure (sample notation H063). Its parameters are given in Fig. 3.13(a). The structure consists of 60 periods of 8.2 nm thin GaAs wells, separated by 19.6 nm thin

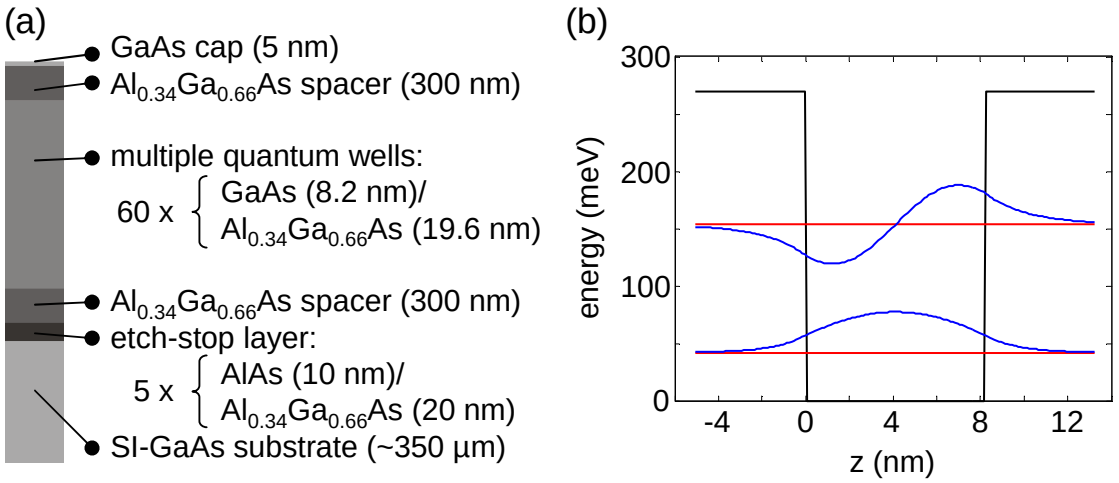

Figure 3.13.: (a) Structure parameters for the GaAs/$Al_{0.34}Ga_{0.66}As$ multiple quantum well sample. A spacer layer on top of the structure ensures a good spatial overlap with the THz beam in a 38° wedged waveguide geometry. An etch stop superlattice allows the removal of the semi-insulating (SI) GaAs substrate. (b) Electronic energy band diagram in growth direction z for a single quantum well of our MQW structure. The calculated energy levels (red lines) are given with the corresponding envelope wave functions (blue lines).

$Al_{0.34}Ga_{0.66}As$ barriers. A 300 nm thick $Al_{0.34}Ga_{0.66}As$ spacer layer was grown on top of the structure. It ensures a good spatial overlap with the THz beam at the intersubband resonance wavelength as has been demonstrated in Fig. 2.3(b). At the same time it is transparent for NIR light for efficient photoexcitation of the undoped quantum wells. An identical spacer layer has been inserted underneath the MQW structure. It is separated from the semi-insulating (SI) GaAs substrate by five periods of a $Al_{0.34}Ga_{0.66}As$/AlAs etch stop superlattice with layer thicknesses of 20 and 10 nm, respectively. As already mentioned, the sample was polished in a 38° wedged waveguide geometry for the optical near-infrared pump intersubband THz probe experiment (see next chapter 4).
The experiments investigating sideband generation (chapter 5) and Autler-Townes splitting (chapter 6) require a transmission geometry in the near-infrared spectral region. To this end a 5×5 mm^2 piece of the aforementioned wafer has been glued on 500 μm thick NIR-transparent <100>-oriented ZnTe and the semi-insulating GaAs substrate has been etched down to the etch stop superlattice[9]. Note that we do not use <110>-oriented ZnTe as substrate. <110>-ZnTe is commonly used in electro-optic

[9] The following sample preparation has been performed at the Vienna Technical University [86]: First, the GaAs substrate was removed to a residual thickness of 50-60 μm. Then the sample was glued on the ZnTe substrate using a photoresist (*Clariant GmbH: AZ5214*). After 10 minutes of baking at 100°C, the ZnTe backside was also protected with a photoresist layer. The remaining GaAs substrate was removed by wet etching in a H_2O_2:NH_3 (20:1) solution that stops on AlGaAs where one notices the surface to turn from rough to smooth. Afterwards the sample was cleaned for some seconds using a developer (*micro resist technology GmbH: ma-D 333*). Note that the photoresist softens at temperatures of 100°. Also it solves in acetone!

detection (see section 3.2). Here, we want to avoid an electro-optic effect that changes a near-infrared beam polarization when illuminated with a THz beam. <100>-ZnTe does not show such an electro-optic response.
Figure 3.13(b) plots the conduction band potential for a single quantum well of our MQW structure. Solving the Schrödinger equation yields energies of 41.9 meV and 153.7 meV for the two lowest conduction subbands[10] (plotted as red lines with the corresponding envelope wave functions in blue). The resulting intersubband spacing of 111.8 meV (27.0 THz or 11.1 μm) is in good agreement with the measured value of 27.3 THz (see Fig. 4.4 on page 48). Further sample characteristics are shifted to the positions in this thesis where they are directly required, in order to prevent redundancy. Apart from the aforementioned intersubband resonance, Fig. 5.2 on page 66 gives the transmission of the etched sample, Fig. 5.3 on page 68 shows the 1s-2p transition of the hh(1s) exciton whereas a time-resolved photoluminescence can be found in Fig. 5.4 on page 69.

[10] Matlab program by Myron Seto, Institute of Semiconductor and Solid State Physics, University of Linz, Linz, Austria.

4. Fano signatures in the intersubband terahertz response

In this chapter broadband THz pulses are used to probe the conduction intersubband transition of an undoped GaAs/$Al_{0.34}Ga_{0.66}As$ multiple quantum well after resonant photoexcitation at the 1s heavy-hole exciton. The pump-induced change in the transmitted THz field reveals a strong beating. In the frequency domain this results in an asymmetric Fano-like line shape for the intersubband resonance and an additional broad low-frequency peak. However, the total THz absorption shows only the expected single symmetric peak of the intersubband transition. In our microscopic theory these signatures unambiguously originate from the phase-sensitive superposition of ponderomotive and THz intersubband currents. These features appear in field-resolved THz spectroscopy, but not in intensity-based standard FTIR spectroscopy, as we will discuss shortly.

Parts of this chapter have been published in *Phys. Rev. Lett.* **102**, 127402 (2009).

4.1. Introduction

Terahertz experiments on optically excited or doped semiconductors provide unique opportunities to analyze and manipulate low-energy excitations or quasi-particle states, like intersubband transitions between quantum confined states [60, 61, 87–89], excitons or plasmons, and monitor their dynamical evolution [9, 90–93]. With sufficiently strong THz pulses, one can even reach the regime of "extreme nonlinear optics" leading to effects like Rabi flopping [19, 89, 94], ac Stark splitting [95] or the dynamical Franz-Keldysh effect [96, 97].
The microscopic analysis of these experiments shows that the THz wave propagating through the semiconductor is determined by the combined response of the so-called ponderomotive current and the true THz transitions. Here, the ponderomotive contribution refers to the charge current generated by the classical field that causes a wiggling motion of the carriers according to the acceleration theorem $\hbar\dot{\mathbf{k}} = -e\,\mathbf{E}_{\mathrm{THz}}$ [98, 99]. The time-averaged kinetic energy of such a particle's motion during one cycle of light leads to the well known ponderomotive energy $U_p = e^2E^2/(4m^*\omega^2)$ (with the effective mass m^*). This part of the light-matter interaction, often thought to

be relevant only at high intensities [97], produces the simple response with the linear susceptibility $\chi(\omega) = -\omega_\mathrm{p}^2/\omega^2$ (ω_p is the plasma frequency). Due to the factor ω^{-2}, the ponderomotive contribution can usually be neglected in the analysis of interband optical excitations. However, it is of relevance in the low-energy THz regime even at the lowest intensities. It is described by an additional ponderomotive current J_A as source term in the wave equation where J_A is related to the vector potential $\mathbf{A}$ of the THz pulse.
Thus, the THz response of an excited semiconductor is influenced by ponderomotive effects plus the true THz transitions. When both contributions are of equal strength, one expects a strong interplay. In the experiment reported in reference [18] the change in the near-infrared transmission of semiconductor quantum wells driven by strong THz fields revealed several high-field effects like the dynamical Franz-Keldysh effect [96], but also some evidence for a ponderomotive contribution. Likewise, the experiment [19] investigating the intraexcitonic response of Cu_2O under intense THz illumination required a ponderomotive current for an accurate description. However, both experiments provided only rather indirect evidences for the role of the ponderomotive current. Their influence could only be seen by virtue of a theoretical switch-off analysis.
To clearly expose the interplay of ponderomotive and true THz response, one needs an experimental method that makes it possible to observe both effects directly. Here, we study the intersubband transition of photoexcited semiconductor quantum wells using linear THz spectroscopy. Monitoring the transmission of a broadband THz pulse, we directly observe signatures of the ponderomotive motion of the excited carriers and show that interference of ponderomotive and resonant contributions produces a characteristic Fano-like line shape in the differential transmission spectrum.
Asymmetric Fano line shapes are known to result from quantum interference between two competing optical transitions. One transition connects a discrete excited energy state with the ground state, while the other one connects a nearby continuum with the ground state [100]. Fano interferences have been observed in semiconductor heterostructures under various conditions [101–107]. Whereas the relevant continuum in typical Fano configurations is an integral part of the probed quantum object, in our system an effective continuum is provided by the light-matter interaction through the ponderomotive contribution.

4.2. Experimental realization

Figure 4.1(a) represents our experimental scheme which is based on the broadband THz setup described in section 3.2 (page 18) and Fig. 3.2. The THz pulses are generated in a 55 μm thin z-cut GaSe crystal. They are focused by a gold-coated off-axis parabolic mirror with an effective focal length of 11.6 cm on the multi quantum well (MQW) sample, with the THz field having a strong component perpendicular to the MQW plane to couple effectively to the intersubband transition. This is promoted by the 38° wedged waveguide geometry of the sample. For THz field-resolved detection phase-

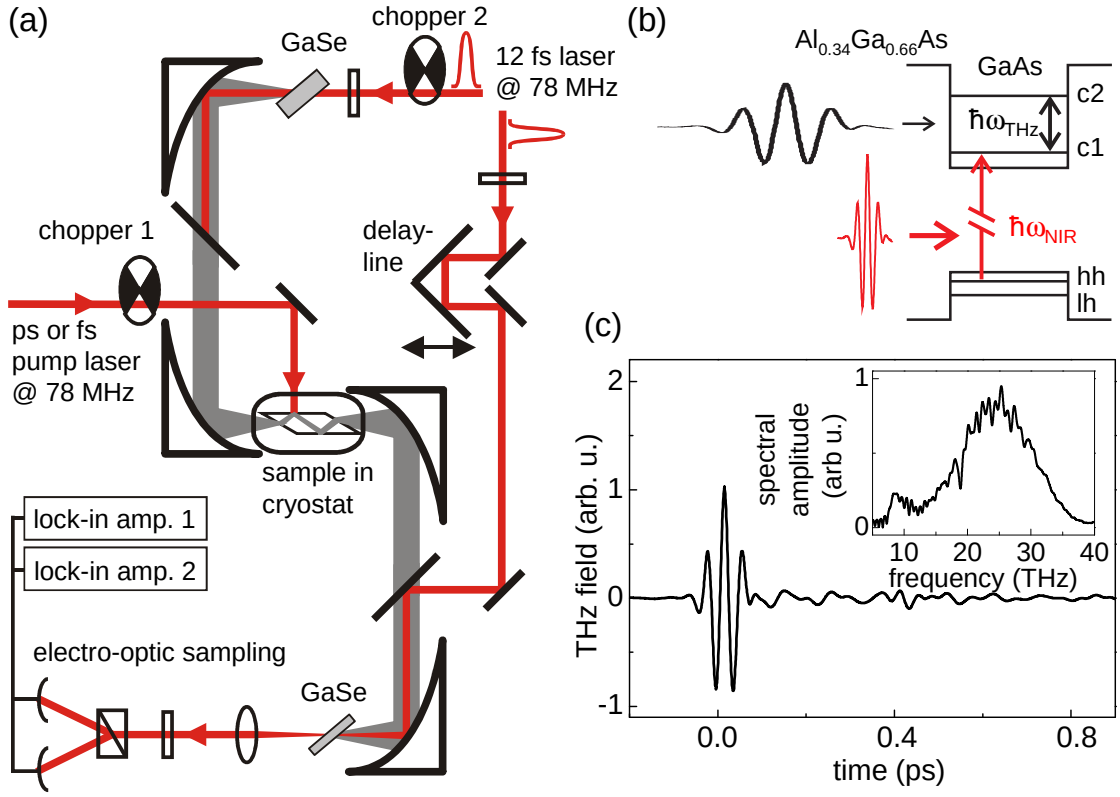

Figure 4.1.: (a) Optical interband pump intersubband THz probe experiment. The THz setup is identical to the one of Fig. 3.2 on page 21 with an additional pump laser for optical excitation of the sample. A *two lock-in amplifier technique* is employed to measure simultaneously the differential transmission and the reference without optical pump. (b) THz pulses are used to probe the c1-to-c2 conduction band transition 25 ps after photoexcitation of the hh-c1 transition at the hh($1s$) exciton resonance in the undoped MQW sample. (c) Measured THz field without sample and the corresponding broadband spectrum (inset).

matched electro-optic sampling is applied within a second 25 μm thin GaSe crystal (see section 3.2). Figure 4.1(c) shows the measured THz transient without the sample inserted. The few-cycle pulse is accompanied by a broadband THz spectrum as given in the inset.

The photoexcitation scheme is illustrated in Fig. 4.1(b). The relevant energy levels in the quantum wells are the two lowest states c1 and c2 in the conduction band, and the heavy-hole (hh) level in the valence band. The light-hole (lh) state does not play a role here. An optical interband pump pulse excites the MQW resonantly at the hh($1s$) exciton and creates carriers in the first conduction subband c1. We choose either spectrally narrow 2.5 ps or broadband 100 fs optical excitation. Both lasers are 78 MHz Ti:sapphire oscillators (*Spectra Physics: Tsunami*), locked to the repetition rate of the THz generating 12 fs laser. In each case only the first excited conduction band of the MQW is populated. In Fig. 4.2 the two different excitation conditions are depicted. The sample absorption (black line) taken from the transmission of the etched MQW

film on the ZnTe substrate (see Fig. 5.2 on page 66) is given together with a schematic spectrum for ps (blue solid line) and broadband fs (blue dashed line) laser excitation at the hh($1s$) exciton resonance. Note that the adjacent hh($2s$) and lh($1s$) states are partly excited in the latter case, but not significantly. After a time delay of 25 ps during which the optically induced interband coherences have disappeared, the weak broadband THz pulse probes the c1-to-c2 intersubband transition. All the experiments are performed at a sheet electron density of approximately $2 \times 10^{10}\,\mathrm{cm}^{-2}$ per quantum well. The sample parameters are described in section 3.5. The calculated conduction band c1-to-c2 intersubband transition lies at 27 THz and is well covered by the broadband THz probe spectrum. The sample waveguide is mounted in a liquid He continuous flow cryostat (*Cryo Industries*). The cryostat is equipped with a pair of 530 μm thick diamond windows for the THz transmission and a quartz window for the NIR optical pump laser. CVD diamond (from chemical vapor deposition) is transparent from the near ultraviolet to the far-infrared region (approx. 250 nm to above 500 μm [108]). The experiments are performed at a temperature of 6 K.

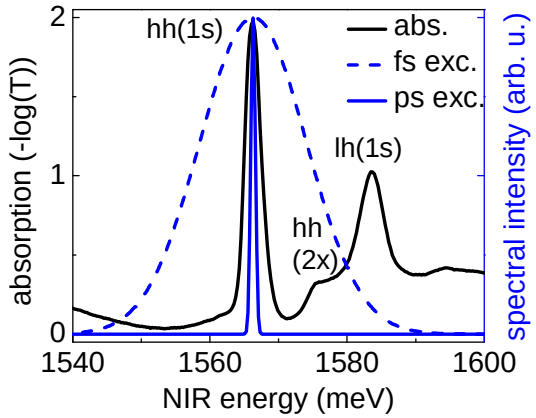

Figure 4.2.: Sample absorption (black line) taken from the etched MQW film (see Fig. 5.2 on page 66) and the scheme for the two different photoexcitation conditions at the hh($1s$) exciton, i.e. narrowband ps excitation (blue solid line) and broadband fs excitation (blue dashed line). Energetically higher states like hh($2x$) (x marks the s and p states) and lh($1s$) are not important here.

A *two-lock-in amplifier technique* is employed to measure the transmitted THz transients with and without excitation at the same time (see Fig. 4.1(a)). Before explaining this technique we define the differential transmission, i.e. the pump-induced change in the transmitted THz field:

$$\Delta E(t) = E(t)_{\text{with pump}} - E(t)_{\text{without pump}} = E(t)_{\text{with pump}} - E(t)_{\text{ref}}. \tag{4.1}$$

The visible pump and THz probe beams are chopped simultaneously with two mechanical choppers at different frequencies around 2 kHz. The first lock-in amplifier locks on the modulation of the optical pump beam. It measures the full pump-induced change in the transmitted THz field $\Delta E(t)$ when the THz beam is not blocked by the second chopper, otherwise it measures no signal. Consequently, its average signal LI_1 is half of the differential transmission:

$$\mathrm{LI}_1 = \frac{1}{2}\Delta E(t) = \frac{1}{2}[E(t)_{\text{with pump}} - E(t)_{\text{ref}}]. \tag{4.2}$$

The second lock-in amplifier which is connected to the chopper in the THz beam detects the mean value between transmission with and without photoexcitation:

$$\mathrm{LI}_2 = \frac{1}{2}[E(t)_{\text{with pump}} + E(t)_{\text{ref}}]. \tag{4.3}$$

Hence, while $\Delta E(t)$ is twice the signal LI_1, we obtain the reference without excitation $E_{\mathrm{ref}}(t)$ by subtracting the signals of both lock-in amplifiers: $E(t)_{\mathrm{ref}} = \mathrm{LI}_2 - \mathrm{LI}_1$.
This technique allows us to record $\Delta E(t)$ and $E_{\mathrm{ref}}(t)$ simultaneously under exactly the same conditions, preventing a drift in the relative phase between them. Such a phase drift can be caused by thermal changes of the whole setup including the laser system. But more likely it is due to the mechanical delay line which has a limited repeatability of 2 μm when returning to the start position caused by friction, hysteresis and backlash. Since the NIR probe light is reflected from the mirror on the delay line this uncertainty is doubled to 4 μm which has to be compared to the sample's intersubband resonance wavelength of 11 μm. Hence, measuring $\Delta E(t)$ and $E_{\mathrm{ref}}(t)$ not simultaneously but one after the other might lead to a random drift in the relative phase between them, which can be of the order of half an oscillation at the intersubband resonance. Certainly this strongly affects the computed THz absorption and could for instance turn an absorption into apparent gain.
Using the measured field transients the total THz absorption $\alpha(\omega)$ is computed via

$$\alpha(\omega) \approx \frac{\omega}{nc}\mathrm{Im}[\chi(\omega)] = 2\mathrm{Im}\left[-\mathrm{i}\frac{\Delta E(\omega)}{E_{\mathrm{ref}}(\omega)}\right]. \tag{4.4}$$

n is the refractive index and c the vacuum speed of light. Also the complex valued Fourier transforms of $\Delta E(t)$ and $E_{\mathrm{ref}}(t)$ enter. This relation follows from Maxwell's equations and is derived in appendix B on page 105 under the assumptions that (i) $|\Delta E| \ll |E_{\mathrm{ref}}|$, (ii) the unexcited sample is nonabsorptive in the investigated frequency range, and (iii) only a single-pass signal through the quantum wells is measured.

4.3. Experimental results

Figure 4.3 displays the measured quantities. In panel (a) the reference THz field transient $E_{\mathrm{ref}}(t)$ transmitted without photoexcitation is given. Compared to the incident THz field which is similar to Fig. 4.1(c), the field oscillations last longer in time due to dispersion in the sample, i.e. the pulse is chirped. Figure 4.3(b) shows the absolute value of the spectral amplitude $|E_{\mathrm{ref}}(\omega)|$. Note that compared to a similar spectrum without sample (inset of Fig. 4.1(c)) the low-frequency components below ≈ 16 THz are missing due to multiple phonon absorption processes in the GaAs substrate [109]. The spectral dip at ≈ 18.5 THz probably originates from TO+TA phonon absorption [110, p. 291] in the Si beamsplitters of the THz setup, since it is also present in the spectrum without sample (see inset of Fig. 4.1(c)).
In Fig. 4.3(c) the measured differential transmission $\Delta E(t)$ 25 ps after narrowband ps excitation at the hh($1s$) exciton position is plotted. First, one observes that the signal has a decay constant of 440 fs, whereas a decay within 240 fs is found for the reference $E_{\mathrm{ref}}(t)$ in panel (a). One has to keep in mind that the broadband reference pulse is influenced by the material's dispersion more strongly than the differential transmission that mainly consists of an oscillation around the intersubband resonance frequency.

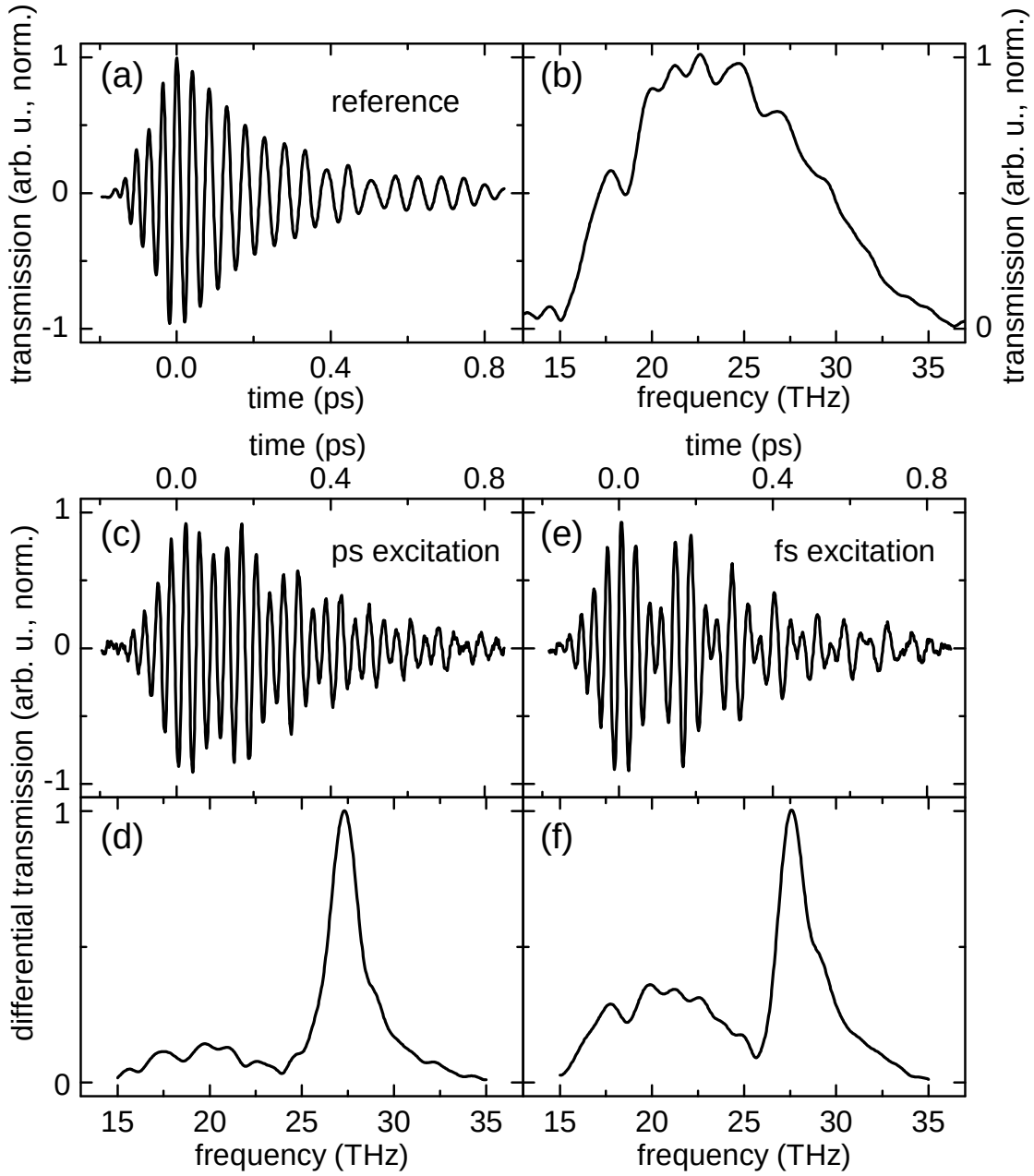

Figure 4.3.: (a) Time-resolved multiple quantum well transmission $E_{\mathrm{ref}}(t)$ without photoexcitation. (b) Corresponding absolute value $|E_{\mathrm{ref}}(\omega)|$ of the spectral amplitude. (c), (d) Differential transmission $\Delta E(t)$ and $|\Delta E(\omega)|$, respectively, after ps excitation at the hh(1s) exciton resonance. Clearly, a beating appears in the time domain and a low-frequency peak in the differential spectrum. (e), (f) Differential transmission $\Delta E(t)$ and $|\Delta E(\omega)|$, respectively, after broadband fs excitation. The beating in the time-domain and the low-frequency peak in the spectrum are more pronounced than for ps excitation.

This narrowband oscillation is preserved at all time steps in the time transients of the differential transmission, whereas the broadband transmission of Fig. 4.3(a) reveals different oscillation frequencies at different time steps. The longer oscillations in the differential transmission reveal the dephasing of the reradiated THz-induced intersubband polarization, as has been observed in the literature before [60, 61, 87]. It originates from the coherent superposition of the two conduction band states driven by the broadband THz probe pulse that covers the intersubband spacing between both states $|c1\rangle$ and $|c2\rangle$. The superposition state $|\psi(t=0)\rangle = 1/\sqrt{2}(|c1\rangle + |c2\rangle)$ is not stationary and evolves in time according to

$$|\psi(t)\rangle = \frac{1}{\sqrt{2}}\left(\mathrm{e}^{-\frac{\mathrm{i}}{\hbar}E_1 t}|c1\rangle + \mathrm{e}^{-\frac{\mathrm{i}}{\hbar}E_2 t}|c2\rangle\right) \propto |c1\rangle + \mathrm{e}^{-\frac{\mathrm{i}}{\hbar}(E_2-E_1)t}|c2\rangle. \tag{4.5}$$

The excited electron wavepacket oscillates between both states and radiates with the energy difference $E_2 - E_1$. This THz-induced polarization decays via dephasing on a time scale of a few hundred fs which is mainly due to electron-electron scattering [111, 112] instead of a population relaxation occuring on a time scale around 1 ps [113]. However, going back to Fig. 4.3(c), one can notice a clear beating signature compared to the reference $E_{\mathrm{ref}}(t)$ which is superimposed on the dephasing. The absolute value of the Fourier transform $\Delta E(\omega)$ in panel (d) shows two major contributions: (i) a sharp resonance peak at the intersubband transition frequency $\nu_{12} = 27.3$ THz and (ii) a broad low-frequency peak around 20 THz. This low-frequency peak is directly connected to the observed beating in the time-domain. Furthermore, the line shape at the intersubband resonance reminds us of a typical Fano spectrum, i.e. an undershoot at the low-frequency side of the intersubband transition peak followed by an asymmetric broad shoulder on the high-frequency side. Note that before normalizing the presented data the maximum oscillation amplitude in the time-domain transients $\Delta E(t)$ is smaller for ps (fs) photoexcitation by a factor of 34 (24) compared to the reference oscillation $E_{\mathrm{ref}}(t)$. In the frequency-domain the peak at ≈ 27 THz in the differential transmission $|\Delta E(\omega)|$ is smaller by a factor of ≈ 12 than the maximum in the reference spectrum $|E_{\mathrm{ref}}(\omega)|$. This justifies our previous assumption of $|\Delta E| \ll |E_{\mathrm{ref}}|$ which has been employed for deriving a formula for the total THz absorption $\alpha(\omega)$ (Eq. (4.4)).

When the system is excited with a broadband 100 fs laser pulse at the same hh($1s$) exciton position, the beating in the time domain is more pronounced than for the narrowband ps excitation (see Fig. 4.3(e)). Accordingly, in the frequency domain one observes a stronger low-frequency contribution and a stronger Fano asymmetry, as can be seen in Fig. 4.3(f).

In order to check whether the broad feature in the differential transmission is caused by an additional carrier transition besides the intersubband resonance, we measure the total THz absorption α simultaneously with the differential transmission. Figure 4.4(a) plots the absorption α (computed via Eq. (4.4)) for both fs and ps excitation (black solid and red dashed line, respectively). It shows that the absorption is single peaked, i.e. only the intersubband resonance appears and no Fano-like signature is observed. Moreover, there is no change in the absorption for the broadband fs excitation despite the more pronounced low-frequency peak in the differential transmission. In panel (b)

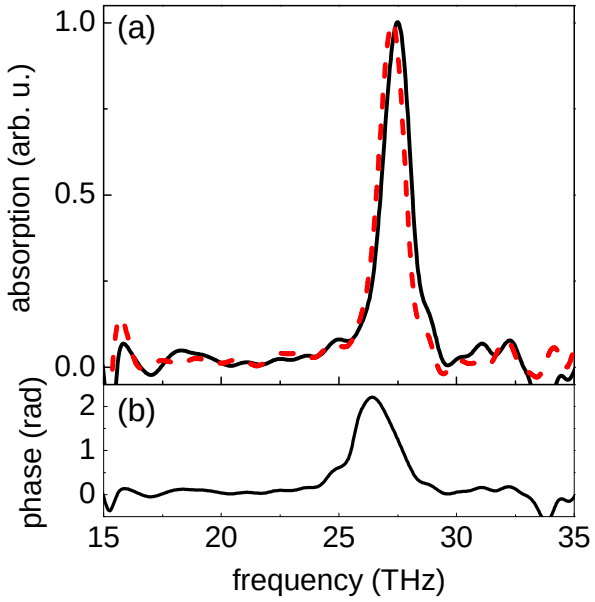

Figure 4.4.: (a) Total THz absorption showing the intersubband transition after fs (black solid line) and ps (red dashed line) excitation, respectively. (b) Corresponding phase after fs photoexcitation.

of Fig. 4.4 the corresponding phase is given for fs excitation. We clearly notice an abrupt change in phase by 126° 1 THz below the intersubband resonance. It starts at the spectral position 25.2 THz where a minimum in the differential transmission occurs (compare Fig. 4.3(f)).
The lack of an additional carrier transition is especially interesting in the case of broadband fs excitation, since also the lh($1s$) state is populated slightly by the spectrally broad pump pulse. Such a coherent excitation of two adjacent energy levels is known to lead to a superposition of states resulting in THz emission with the frequency of the hh-lh splitting [114]. In our case the hh-lh splitting energy is around 17 meV, corresponding to 4.1 THz, which is far away from the 20 THz where the broad additional peak is located in our experiment. However, an additional lh1-lh2 transition in the valence band becomes also possible when the lh($1s$) state is occupied. This valence intersubband transition is expected at around 18 THz [115] and could be responsible for the low-frequency peak in $\Delta E(\omega)$. But even when the broadband fs photoexcitation is tuned completely to the lh($1s$) exciton, the THz absorption remains unchanged. Only the low-frequency peak in $\Delta E(\omega)$ decreases by a factor of 1.7 (not shown here). Therefore, an additional lh1-lh2 transition can be experimentally ruled out. This is also supported by the fact that $\Delta E(\omega)$ does not change with the time delay between pump and probe in the range from 5 ps to 200 ps. The ratio between low-frequency peak and intersubband transition peak is constant, while the total signal decreases due to carrier recombination. Additionally, the time-resolved photoluminescence of this sample under fs excitation at different spectral positions around the hh($1s$) and lh($1s$) exciton showed no contribution from the lh1-c1 recombination that would have been

present for a significant lh1 population. Consequently, the lh($1s$) state does not seem to play a role in our experiment.
Besides these findings the experiment reveals other characteristics:

- The beating vanishes for increasing temperatures: for broadband fs excitation it is still present at liquid nitrogen temperature, but not at room temperature (RT)[1]. This is accompanied by a THz absorption line broadening from 1.3 THz (6 K) to 1.9 THz (RT), which could be the reason for the vanishing beating at elevated temperatures.

- Smaller excitation densities lead to a more pronounced low-frequency peak in the differential transmission $\Delta E(\omega)$.

- Both intersubband resonance peak and broad low-frequency peak decrease linearly with the THz probe intensity, indicating only a linear THz regime. Hence, with an estimated THz field strength in the sample of 100 V/cm we do not enter the strong THz field regime where nonlinear effects could be expected.

- Tuning the THz probe spectrum to higher energies decreases the low-frequency peak and increases the Fano-like asymmetry of the intersubband resonance at energies above the intersubband transition.

In conclusion, the beating in the time domain and the low-frequency peak in the frequency domain of the differential transmission do not appear to originate from a second real absorptive transition in the system besides the intersubband resonance. In the following section we outline a theoretical model which will explain our experimental findings.

4.4. Theoretical model

The following section describes our theoretical model that has been developed by D. Golde, M. Kira and S. W. Koch at the theory group of the Philipps-University, Marburg (Germany).
To explain our experimental findings, the THz transmission of a single quantum well positioned at $z = 0$ is computed (z is the growth direction). The quantum well is assumed to be surrounded by a material with a background refractive index n_b of GaAs. Via this approach the actual 38° wedged waveguide geometry is neglected. But since the geometry influences the intersubband resonance contribution and the

[1] Note that the laser could not follow the bandgap shift at room temperature and excited nonresonantly. For ps excitation the resonant condition could be maintained up to room temperature. However, the beating itself is much less pronounced for ps excitation and vanishes completely between 50 to 70 K.

ponderomotive contribution in the same way, the result should not be affected much by this simplification. Furthermore, since the THz wavelength is much larger than the total MQW width, all the single well contributions add up constructively to the total THz response. The total number of 60 quantum wells is taken into account when the quantitative transmission through the MQW is calculated.
The THz response follows from the wave equation

$$\left(\nabla^2 - \frac{n_b^2}{c^2}\frac{\partial^2}{\partial t^2}\right) E(\mathbf{r},t) = \mu_0 \delta(z) \frac{\partial}{\partial t} J_{\mathrm{tot}}(t), \tag{4.6}$$

where n_b is the background refractive index of the unexcited system, c is the speed of light, and μ_0 is the permeability of free space. Here, a delta function arises since the quantum well width is much smaller than the THz wavelength. On the right hand side of the equation the induced total current density $J_{\mathrm{tot}}(t) = J_{\mathrm{A}}(t) + J_{\mathrm{THz}}(t)$ consists of two contributions: J_{THz} is the current due to the intersubband transitions, and J_{A} describes the THz-field induced ponderomotive motion of the excited carriers. Here, an interband polarization is neglected ($P = 0$) since all coherences have already decayed for the considered time delay between NIR pump and THz probe of 25 ps. Such a contribution P would appear on the right hand side of the equation as source term in the form $\mu_0 \delta(z) \partial^2 P(t)/\partial t^2$.
Solving Eq. (4.6), one finds for the transmitted and reflected fields [116, 117]:

$$\begin{aligned} E_{\mathrm{T}}(\omega) &= E_{\mathrm{ref}}(\omega) - \frac{\mu_0 c}{2n_b} J_{\mathrm{tot}}(\omega) \\ E_{\mathrm{R}}(\omega) &= -\frac{\mu_0 c}{2n_b} J_{\mathrm{tot}}(\omega). \end{aligned} \tag{4.7}$$

Our measured quantity, the differential transmission $\Delta E(\omega) = E_{\mathrm{T}}(\omega) - E_{\mathrm{ref}}(\omega)$, is therefore directly proportional to the sum of ponderomotive and intersubband currents:

$$\Delta E(\omega) = -\frac{\mu_0 c}{2n_b} J_{\mathrm{tot}}(\omega) \propto J_{\mathrm{A}}(\omega) + J_{\mathrm{THz}}(\omega). \tag{4.8}$$

It can be interpreted as a field reemitted by the current density.
The ponderomotive contribution J_{A} to the total current density is defined [118, 119] via

$$J_{\mathrm{A}} = -\sum_{\lambda} \frac{e^2 n_\lambda}{m_\lambda} A_{\mathrm{THz}} \tag{4.9}$$

with the effective mass m_λ and the carrier density n_λ in band λ (λ includes both bulk-band index and subband index). Consequently, J_{A} directly follows the vector potential A_{THz} of the THz probe pulse with an opposite phase. This vector potential is related to E_{THz} in the time and frequency domain, respectively, by

$$\begin{aligned} E_{\mathrm{THz}}(t) &= -\frac{\partial}{\partial t} A_{\mathrm{THz}}(t) \\ E_{\mathrm{THz}}(\omega) &= i\omega A_{\mathrm{THz}}(\omega). \end{aligned} \tag{4.10}$$

The ponderomotive current J_{A} is believed not only to result from a wiggling motion of carriers in the quantum well plane, but also in growth direction, since in our case the THz field is nearly equally composed of both components[2]. Though the carrier motion is restricted in the growth direction z, the periodical THz-field induced tilting of the confinement potential modulates the z-dependent envelope function of the electron wave function. In this simple picture the periodic modification leads to a wiggling motion in z-direction as well. For the actual calculation the ponderomotive response in the plane and in growth direction are assumed to be equal. The uncertainty of this simplification is believed to be smaller than other uncertainties of the measurement (like, for instance, in the intersubband matrix element) [115].
In the derivation of Eq. (4.6) J_{A} and J_{THz} can be connected to different parts of the light-matter interaction Hamiltonian [118–121]. In second-quantization this minimal-substitution Hamiltonian evaluated in the Bloch basis at the level of second-order $\mathbf{k}\cdot\mathbf{p}$ theory reads within the Coulomb gauge ($\nabla\cdot\mathbf{A}_{\mathrm{THz}}=0$):

$$\hat{H}_{\mathrm{interaction}}=\sum_{\lambda,\mathbf{k}}\left[-j_{\lambda}(\mathbf{k})A_{\mathrm{THz}}(t)+\frac{e^2}{2m_0}A^2_{\mathrm{THz}}(t)\right]\hat{a}^{\dagger}_{\lambda,\mathbf{k}}\hat{a}_{\lambda,\mathbf{k}}-\sum_{\substack{\lambda,\lambda'\neq\lambda,\\ \mathbf{k}}}D_{\lambda,\lambda'}A_{\mathrm{THz}}(t)\hat{a}^{\dagger}_{\lambda,\mathbf{k}}\hat{a}_{\lambda',\mathbf{k}}. \tag{4.11}$$

Here, we have introduced the intraband current-matrix $j_{\lambda}(\mathbf{k})=-e\hbar\mathbf{k}\cdot\mathbf{e}_p/m_{\lambda}$, where $\mathbf{e}_p$ is the polarization direction of the THz field and m_0 stands for the free electron mass. $\hat{a}^{\dagger}_{\lambda,\mathbf{k}}$ and $\hat{a}_{\lambda,\mathbf{k}}$ are the fermionic creation and annihilation operators, respectively, for an electron in band λ with momentum $\hbar\mathbf{k}$. $D_{\lambda,\lambda'}$ is the interband dipole matrix element in the part of the Hamiltonian which describes interband transitions between different bands.
J_{A} follows from both the A^2 part and the interband transition part of $H_{interaction}$. The latter contribution is necessary to give the correct effective mass instead of the free electron mass m_0 in Eq. (4.9) [118]. J_{THz} results from the first term, i.e. the $\mathbf{p}\cdot\mathbf{A}$ part of the Hamiltonian.
The ponderomotive current density J_{A} leads to a real-valued linear susceptibility:

$$\chi_{\mathrm{A}}(\omega)=\frac{J_{\mathrm{A}}(\omega)}{\epsilon_0\omega^2A_{\mathrm{THz}}(\omega)}=-\sum_{\lambda}\frac{e^2n_{\lambda}}{\epsilon_0m_{\lambda}\omega^2}=-\omega^2_{\mathrm{p}}/\omega^2. \tag{4.12}$$

ω_{p} denotes the plasma frequency. The result gives the well-known Drude response of a free electron gas without damping (for example [122, p. 249]). Since the frequencies are real-valued quantities, so is the susceptibility. Consequently, J_{A} does not contribute to the THz absorption $\alpha(\omega)\propto\omega\,\mathrm{Im}[\chi(\omega)]$ (see Eq. (B.10) on page 106). Only a refractive index change is introduced to the excited material by J_{A}.
The THz current is given by [118, 119]

$$J_{\mathrm{THz}}=\frac{1}{S}\sum_{\lambda,l,l',\mathbf{k}}j^{\lambda}_{l',l}\,p^{\lambda}_{l,l',\mathbf{k}}, \tag{4.13}$$

[2] In our 38° wedged waveguide geometry the ratio between in-plane and normal-to-plane THz field polarization is $\frac{\cos(90°-38°)}{\sin(90°-38°)}=0.78$.

with the quantization area S, the matrix elements $j^{\lambda}_{l,l'}$ and the microscopic intersubband polarization $p^{\lambda}_{l,l',\mathbf{k}}$ between subbands l and l' of bulk band λ. The intersubband matrix element for a THz polarization parallel to the quantum well growth direction is calculated via

$$j^{\lambda}_{l,l'} = -\frac{i\hbar e}{m_\lambda} \int \mathrm{dz}\, \xi^{*}_{\lambda,\mathrm{l}}(\mathrm{z})\, \frac{\partial}{\partial \mathrm{z}} \xi_{\lambda,\mathrm{l}'}(\mathrm{z}), \tag{4.14}$$

where the confinement wave function $\xi_{\lambda,l}(z)$ of the carriers appears. Our calculation yields $j^{c}_{1,2} \approx 16$ eÅ.
The intersubband polarization $p^{\lambda}_{l,l',\mathbf{k}}$ is computed microscopically with an equation-of-motion approach. Since we are interested only in the THz probed conduction band c1-to-c2 transition, the sum is restricted to $\lambda = c$ and $l, l' \in \{1, 2\}$. In close analogy to the effective semiconductor Bloch equations for the interband polarization [121, 123], one finds for the time evolution of the intersubband polarization (see appendix C for a derivation):

$$\begin{aligned} i\hbar \frac{\partial}{\partial t} p^{c}_{1,2,\mathbf{k}} &= \left(\tilde{\varepsilon}^{c}_{2,\mathbf{k}} - \tilde{\varepsilon}^{c}_{1,\mathbf{k}}\right) p^{c}_{1,2,\mathbf{k}} + i\hbar \frac{\partial}{\partial t} p^{c}_{1,2,\mathbf{k}}\bigg|_{\mathrm{scatt}} \\ &+ \left(f^{c}_{1,\mathbf{k}} - f^{c}_{2,\mathbf{k}}\right) \left[j^{c}_{2,1} A_{\mathrm{THz}} - \sum_{\mathbf{q}\neq\mathbf{k}} V_{\mathbf{k}-\mathbf{q}}\, p^{c}_{1,2,\mathbf{q}} \right] + S^{\mathrm{coh}}_{\mathbf{k}}. \end{aligned} \tag{4.15}$$

$\tilde{\varepsilon}^{c}_{l,\mathbf{k}}$ are the renormalized single-particle energies (see (C.11)), $V_{\mathbf{q}}$ is the Coulomb matrix element and $f^{c}_{l,\mathbf{k}}$ are the optically excited carrier distributions in the conduction bands. Note that $f^{c}_{l,\mathbf{k}}$ is calculated from the pump pulse. Since the exact shape of the distribution is believed not to influence the result significantly, relaxation within the distribution is neglected. All scattering effects are contained in

$$i\hbar \frac{\partial}{\partial t} p^{c}_{1,2,\mathbf{k}}\bigg|_{\mathrm{scatt}} \approx -i\gamma\, p^{c}_{1,2,\mathbf{k}}, \tag{4.16}$$

which is modeled by a phenomenological dephasing constant γ to match the measured 440 fs decay. This approximation is justified, since in our case the intersubband transitions are not affected by excitonic effects due to large experimental linewidths (roughly 3.3 meV). $S^{\mathrm{coh}}_{\mathbf{k}}$ includes the coupling to optically excited interband coherences via the Coulomb interaction. However, for the large time delays of optical pump and THz probe pulses in our experiment, the optically excited coherences have decayed such that $S^{\mathrm{coh}}_{\mathbf{k}}$ vanishes.
We compute the single-particle energies of the quentum well system using standard $\mathbf{k}\cdot\mathbf{p}$ perturbation theory. For the THz-response, we include the first two conduction subbands and the first heavy-hole and light-hole subband. The experimental THz reference transient serves as input for the time-dependent fields.

4.5. Discussion

In this section we compare our experimental findings with the results obtained from the theory that has been described in the previous section.

Narrowband ps photoexcitation

We first address the case of narrowband ps excitation at the hh($1s$) exciton energy. Figure 4.5(a) compares the measured differential transmission $|\Delta E|$ (gray shaded area) with the calculated one, which is proportional to the total current density $|J_{\mathrm{tot}}| = |J_{\mathrm{THz}} + J_{\mathrm{A}}|$ (red solid line) (see Eq. (4.8)). The current density is decomposed in its individual contributions $|J_{\mathrm{A}}|$ (blue dotted line) and $|J_{\mathrm{THz}}|$ (green dashed line). Figure 4.5(b) illustrates the THz absorption, where the measurement (gray shaded area) is compared with the calculation (red line). An excellent experiment-theory agreement is obtained for both differential transmission and THz absorption.
As in the measurement, we clearly notice the double peaked Fano-like feature in the transmission spectra whereas the absorption is only single peaked. In our theory, the origin of the Fano-like feature can be investigated by looking at the individual contributions separately. J_{A} directly reflects the electric field $E_{\mathrm{THz}}(\omega)$ of the THz probe pulse, weighted with $\frac{1}{\omega}$ (see Eq. (4.10)). This is also the reason why the calculated contribution J_{A} in Fig. 4.5(a) is not smooth, but contains the particular features of the experimental reference pulse. J_{THz} consists of the intersubband resonance weighted with the pulse spectrum. The broad feature in the transmission spectrum is a direct consequence of the broad probe pulse. The Fano like line shape is caused by the phase-sensitive superposition of the broad ponderomotive and the sharp intersubband contribution, $|J_{\mathrm{tot}}| = |J_{\mathrm{A}} + J_{\mathrm{THz}}|$. A further analysis reveals that for frequencies smaller than the intersubband resonance ν_{12}, both contributions partially compensate each other while they interfere constructively for larger frequencies. This is due to a change in the sign of the real part of J_{THz} at the intersubband resonance (see appendix D on page 110 for more details). The superposition can be seen for instance at around 23 THz where both contributions are of equal strength and their sum $|J_{\mathrm{tot}}|$ nearly vanishes. As for typical Fano situations, this kind of superposition leads to a narrowing of the resonance at the low-frequency side and a broadening at the high-frequency side, resulting in the characteristic asymmetric Fano line shape. Since the ponderomotive current leads to a real-valued susceptibility (see Eq. (4.12)), there is no Fano-like behavior in the THz absorption (Fig. 4.5(b)). Note that this Fano asymmetry does not result from a quantum mechanical coupling of a discrete absorptive transition with a nearby absorptive continuum as in typical Fano situations [100–107]. In fact, in our case the continuum is provided by the light-matter interaction in form of the ponderomotive contribution and is non-absorptive. Moreover, it leads to a Fano line shape via an interference of its electric fields with those from the sharp absorptive intersubband resonance rather than involving quantum interference between coupled

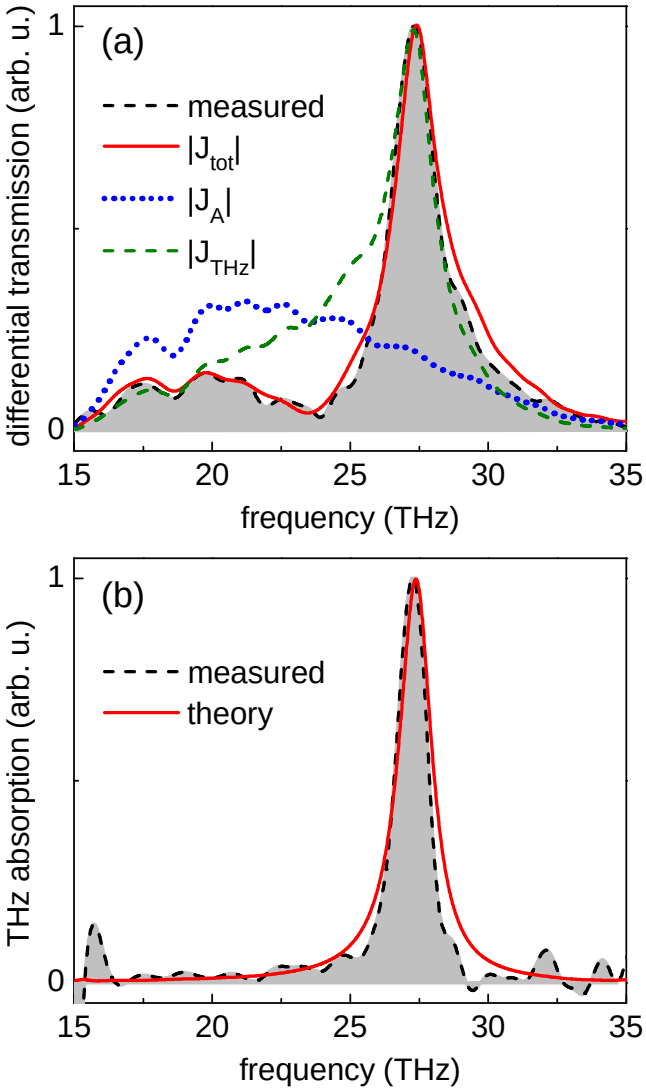

Figure 4.5.: (a) Measured spectral amplitude of the differential transmission $|\Delta E|$ (gray shaded area) and calculated total current density $|J_{\mathrm{tot}}|$ (red solid line) after narrowband ps excitation. $|J_{\mathrm{tot}}|$ is decomposed in its individual contributions, i.e. $|J_{\mathrm{A}}|$ (blue dotted line) and $|J_{\mathrm{THz}}|$ (green dashed line). (b) Measured (gray shaded area) and computed total THz absorption showing the intersubband resonance.

states.

Note that we have observed experimentally an increase in the low-frequency peak in the differential transmission relative to the intersubband peak with decreasing carrier density (not shown). However, in our theory both intersubband and ponderomotive contributions depend linearly on the carrier density in the same way (see appendix D on page 110 for more details). Therefore, our excitation intensity dependence is not explained with our simple model.

Broadband fs photoexcitation

In order to explain the more pronounced ponderomotive feature in the broadband fs experiment, we had to extend our model beyond the single-quantum-well response. Since the fs pump pulse is spectrally significantly broader than the linewidth of the 1s exciton resonance (18.2 meV vs. 3.3 meV), some frequency components are transmitted through the quantum wells and excite carriers in the substrate (see also the excitation conditions in Fig. 4.2). These carriers contribute to J_{A} which contains the carrier density according to Eq. (4.9). But there is no contribution from these additional carriers to J_{THz}, since there are no subbands in bulk material. A quantitative investigation of the interband optical excitation shows that 46% of the pump pulse is transmitted through the quantum wells and absorbed by the substrate. Hence, the total carrier density (in the wells plus substrate) is 1.85 times larger than the density in the quantum wells alone. Since J_{A} is proportional to the carrier density, we can model the substrate contribution to the THz response simply by enhancing J_{A} relative to J_{THz} by a factor of 1.85. The resulting current density is shown as the red solid line in Fig. 4.6. Again, we find an excellent agreement between experiment and theory. In the ps experiment, substrate excitations can be neglected since only 1.4 % of the pump pulse reaches the substrate.

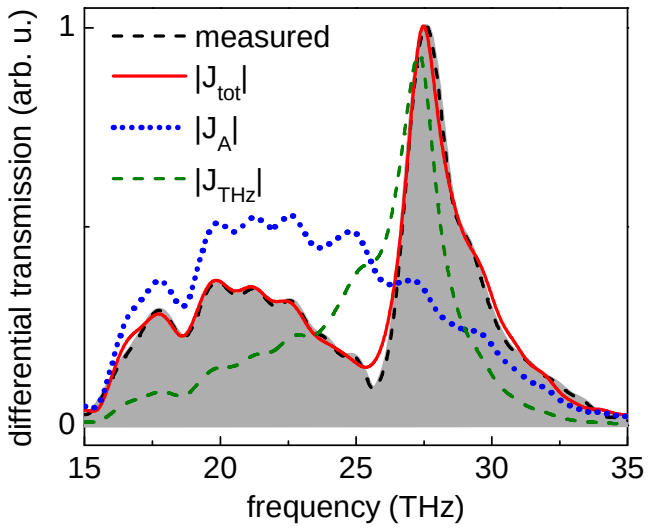

Figure 4.6.: Measured spectral amplitude of the differential transmission $|\Delta E|$ (gray shaded area) and calculated total current density $|J_{\mathrm{tot}}|$ (red solid line) after broadband fs photoexcitation. $|J_{\mathrm{tot}}|$ is decomposed in its individual contributions, i.e. $|J_{\mathrm{A}}|$ (blue dotted line) and $|J_{\mathrm{THz}}|$ (green dashed line).

Influence of THz probe spectrum on Fano line shape for fs excitation

The Fano signatures above are affected by the spectral position of the THz probe spectrum. The broadband THz setup allows us to shift the THz probe spectrum by changing the phase-matching angle. Here, we tune its center frequency away from the previous low-frequency spectrum at 23.5 THz (Fig. 4.7(a) inset, black line) to 26.5 THz (inset, gray line). Since the fs excitation reveals more pronounced features in the

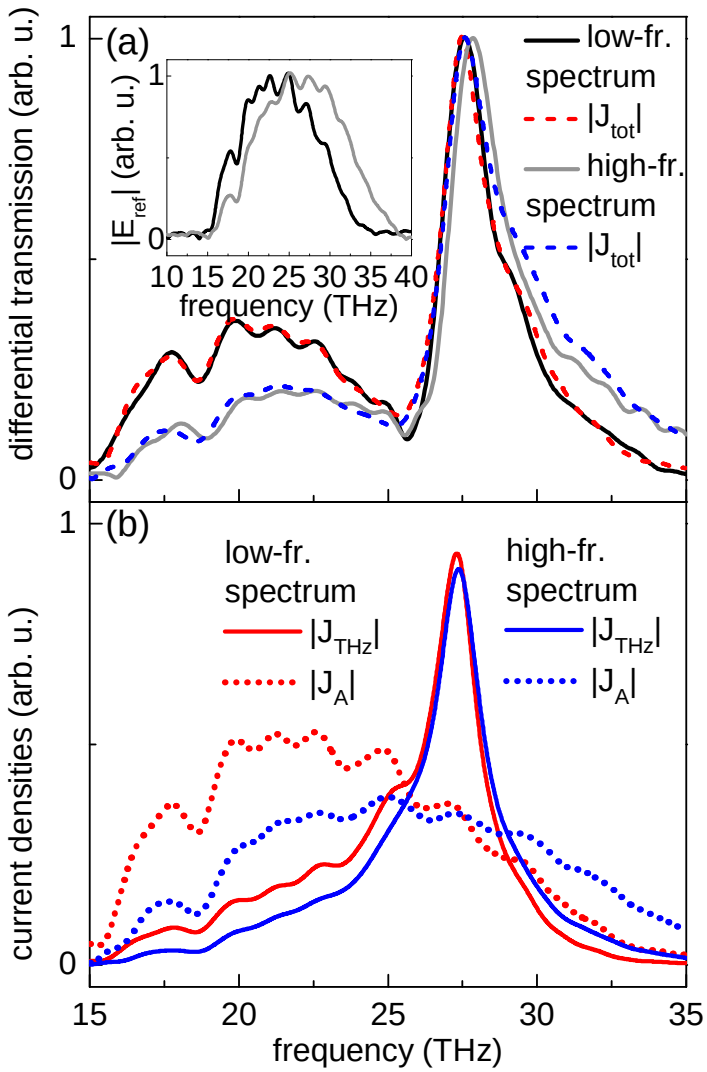

Figure 4.7.: (a) Measured spectral amplitude of the differential transmission $|\Delta E|$ after fs excitation for low-frequency (black solid line) and high-frequency (gray solid line) THz probe spectra (corresponding reference spectra in the inset). In both cases the calculated total current density $|J_{\mathrm{tot}}|$ is given (red and blue dashed line for the low- and high-frequency spectrum, respectively). (b) Decomposition of $|J_{\mathrm{tot}}|$ in $|J_{\mathrm{THz}}|$ (solid lines) and $|J_{\mathrm{A}}|$ (dotted lines) for the low- and high-frequency probe spectrum (red and blue, respectively).

differential transmission compared to the ps experiment, we restrict the discussion to the fs experiment. For the high-frequency probe spectrum the broad peak at around 20 THz decreases while the asymmetry of the intersubband resonance increases, as can be seen from Fig. 4.7(a) (measured: gray solid line; computed: blue dashed line).
The individual contributions J_{THz} and J_{A} are given in Fig. 4.7(b) for both low- and high-frequency probe spectrum. While the intersubband current densities are nearly constant for both probe spectra, the ponderomotive current changes drastically. J_{A} follows the probe spectrum and its peak value is decreased when shifted to higher frequencies. This is expected from the relation $J_{\mathrm{A}} \propto A_{\mathrm{THz}} \propto \frac{1}{\omega} E_{\mathrm{THz}}$ (Eq. (4.9) and Eq. (4.10)). Consequently, the phase-sensitive superposition $|J_{\mathrm{tot}}| = |J_{\mathrm{A}} + J_{\mathrm{THz}}|$ leads to a decrease of the low-frequency peak and an increase on the high-energy side of the intersubband resonance. Note that the ponderomotive current is limited by the spectral width of the THz probe pulses. Thus, by increasing the spectral width one would expect a broadening of the low-energy peak towards lower frequencies and analogously a broadening of the high-energy shoulder above the intersubband resonance towards higher frequencies.

Connection to FTIR spectroscopy

Since numerous measurements mainly using intensity-based spectroscopy (like FTIR) have been carried out on intersubband absorption in quantum wells (for instance [17, 124]), one could ask why the ponderomotive contribution investigated here has not been seen in the intersubband response before. Of course, the main reason is that the ponderomotive current is not absorptive. Therefore, in a standard quantum well transmission measurement in a doped system the intersubband transition will show no ponderomotive feature. However, as has been shown in our approach using field-resolved detection, employing a carrier density modulation should reveal the ponderomotive motion in the differential transmission. To this end it is not important where the carriers originate from. They can come from optical excitation, or doping. Optical excitation does not provide high carrier densities at the large spot size of the broadband FTIR probe beam. Hence, electrically modulation of the carrier density in doped samples with a Schottky gate contact [61, 125] seems best suited. Since we have no sample at hand, we only simulate the outcome of such an experiment.
An FTIR would measure the following differential intensity change $\Delta I(\omega)$ of the transmission without and with excitation, respectively:

$$\Delta I(\omega) = I_{\text{without exc.}}(\omega) - I_{\text{with exc.}}(\omega) \propto |E_{\mathrm{ref}}(\omega)|^2 - |E_{\mathrm{ref}}(\omega) + \Delta E(\omega)|^2 \qquad (4.17)$$

(here, definition (4.1) from page 44 has been inserted). For our simulation we use the field-resolved data for $E_{\mathrm{ref}}(t)$ and $\Delta E(t)$ obtained after fs photoexcitation because there the ponderomotive feature was most pronounced (shown again as gray shaded area in Fig. 4.8(a)). The simulated $\Delta I(\omega)$ is illustrated in Fig. 4.8(b). Obviously, the ponderomotive contribution is much less pronounced than in the field-resolved measurement. This is also true when comparing it to $|\Delta E(\omega)|^2$ (Fig. 4.8(a)), which gives

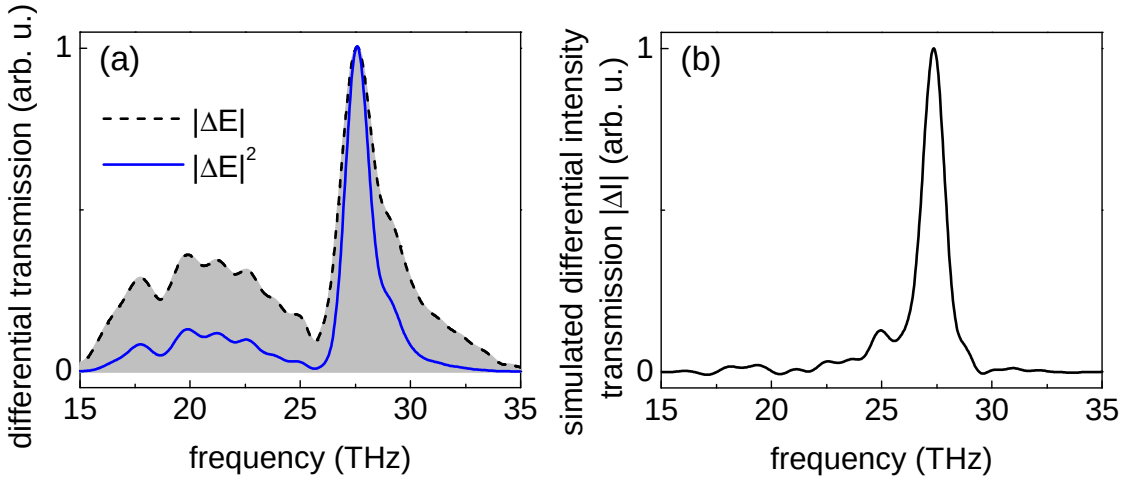

Figure 4.8.: (a) Measured spectral amplitude of the differential transmission $|\Delta E|$ after fs excitation (shaded area), taken from Fig. 4.6. Additionally, $|\Delta E|^2$ is given which can be compared to a simulated intensity-based FTIR measurement. The latter one is illustrated in (b). Here, the fs data from (a) is taken to compute $\Delta I(\omega) = I_{\text{without exc.}}(\omega) - I_{\text{with exc.}}(\omega)$.

an intensity.
The underlying physical reason is that in intensity-based measurements the phase information is lost. For the simulated differential FTIR transmission $\Delta I(\omega)$ the absolute values squared of the electric fields with and without pump, respectively, are taken first, before they interfere. In the field-based signal $|\Delta E(\omega)|^2$ the two fields interfere first, before the absolute value squared is taken. Thus, the relative phase information is conserved only in the latter case. Consequently, an intensity-based approach is not sufficient to investigate the interplay between intersubband and ponderomotive currents.

4.6. Summary and outlook

Employing field-resolved electro-optic sampling, we have measured the differential transmission change in the THz region that is induced by short-pulsed laser excitation of an undoped multiple quantum well. We have shown how the emission by the ponderomotive motion of the excited carriers can directly be identified in the linear THz response. While the THz absorption is only single peaked at the intersubband resonance, the differential transmission spectrum contains an asymmetric Fano like intersubband transition and an additional broad low-frequency peak. Using a microscopic theory for the THz response, the observed Fano-like features can unambiguously be attributed to the phase-sensitive superposition of the intersubband resonance and the ponderomotive carrier dynamics. Our results are connected to the typical Fano situation because the system has a sharp discrete intersubband resonance that interferes

with a broad continuous contribution, i.e. the ponderomotive current density. However, in our case the latter contribution is non-absorptive such that we do not observe the Fano resonance in the absorption spectrum. Finally, the applied field-resolved detection method is found to be better suited than intensity-based measurements (like FTIR spectrocopy) for revealing the ponderomotive influence to the THz response.

Various open questions could be settled in future experiments. One issue is how the ponderomotive contribution reveals itself in doped samples where the carrier density can be modulated electrically.
Another issue could be a time-resolved measurement of the build-up of the ponderomotive carrier motion, i.e. analogous measurements that have been described in this chapter, but with a much shorter time-delay between NIR pump and THz probe.
Also of interest could be whether the expected increase in the ponderomotive contribution at smaller frequencies can be seen (due to its $1/\omega$ dependence). To this end, intersubband transitions in the 1-4 THz range could be investigated, which is accessible with THz antenna structures as outlined in section 3.2.
Additionally, it would be interesting to check experimentally whether the ponderomotive contribution is independent of the angle between the THz probe polarization and the quantum well growth direction, as is assumed in our theory. Attempts in this direction have been made by measuring in a 70° wedged waveguide geometry instead of the 38° one used before. At identical excitation densities, our theory expects a decrease of the low-frequency peak in the differential transmission relative to the intersubband resonance (that should increase, of course). However, we observe an increase by a factor of 1.5 and 2 for ps and fs excitation, respectively. This contrary behavior is believed to result from the nontrivial change of the waveguide properties (compare also Fig. 2.3(b) where both waveguide standing waves are shown). This change influences the THz spot size, the THz standing wave pattern and the NIR pump and THz probe overlap.
As another point, probing a quantum wire or quantum dot THz response could reveal how the ponderomotive carrier motion depends on the confinement of carriers and the different energy-momentum dispersions.

5. THz sidebands in multi quantum wells

This chapter describes sideband generation in symmetric, undoped GaAs/AlGaAs multi quantum wells, i.e. a mixing between a near-infrared laser tuned to excitonic interband transitions and an in-plane polarized terahertz beam from a free-electron laser. The process can be described by a nonlinear susceptibility $\chi^{(3)}$ (see section 2.2 about nonlinear optics). After a short summary on what has been done in the literature, we first describe our experiment before we come to the results and the discussion. We concentrate mainly on second-order sideband generation and compare its efficiency when the THz beam is tuned either to the sample's intraexcitonic heavy-hole 1s-2p transition or to the interexcitonic heavy-hole light-hole transition. We find strong evidence that the intraexcitonic transition is of paramount influence on n=±2 sideband generation, leading to an order-of-magnitude resonant enhancement of the conversion efficiency up to 0.1% at low temperature. At room temperature the efficiency drops only by a factor of 7 for low THz powers.

Parts of this chapter have been published in *Appl. Phys. Lett.* **94**, 241105 (2009).

5.1. Introduction

Strong ac fields in the THz region are known to modify the interband absorption of semiconductor heterostructures. Besides shifts of the excitonic energies, for instance due to the ac Stark effect [95] or dynamical Franz-Keldysh effect [96], strong THz fields can lead to spectral sidebands of an interband excitation.
Terahertz-optical mixing or sideband generation [34, ch. 6.3] has been discovered rather by chance in 1997 by Kono *et al.* [20] and Černe *et al.* [126] at the free-electron lasers of the University of California Santa Barbara (UCSB). Symmetric, undoped GaAs/AlGaAs quantum wells were studied at low temperature in strong magnetic fields under simultaneous illumination with far-infrared radiation polarized in the quantum well plane. Whenever a near-infrared (NIR) excitation with frequency ω_{NIR} was resonant with the interband transition *and* the far-infrared terahertz radiation with frequency ω_{THz} was resonant with internal transitions between magnetoexcitons, additional strong and narrow spectral sidebands could be found at $\omega = \omega_{\mathrm{NIR}} \pm 2 \cdot \omega_{\mathrm{THz}}$.

These n=±2 sidebands showed a linear dependence on the NIR power and a quadratic dependence on the THz power, suggesting a four-wave mixing process between one NIR and two THz photons. For weak THz fields this process involving magnetoexcitons can be modelled using a nonlinear susceptibility $\chi^{(3)}$ and low order perturbation theory [28, 127, 128]. Kono *et al.* [20] reported conversion efficiencies between sideband power and incoming NIR power in the strong magnetic field of typically 0.05% and 0.15% for the n=−2 and n=+2 process, respectively. Highest n=±2 conversion efficiency was achieved with linear THz polarization, suggesting that both right- and left-circularly polarized THz radiation is necessary.

Hereafter, most of the following investigations have been done using intersubband transitions instead of magnetoexcitonic transitons. Groups concentrated on first-order n=±1 sideband generation based on a nonlinear $\chi^{(2)}$ process, since it should reveal a linear THz power dependence and thus a higher conversion efficiency. In a symmetric quantum well system, only even sidebands could be observed, no odd ones like n=±1. For three-wave mixing breaking inversion symmetry is required. This has been achieved at the UCSB FELs [129, 130] in a sample containing asymmetric quantum wells, i.e. two quantum wells of slightly different widths coupled by a thin barrier. Excitonic intersubband transitions were used. Since the electric field of the THz radiation has to be polarized in the growth direction, the THz beam was focused on the cleaved edge of the sample. The sideband polarization state was always the same as for the incoming NIR fundamental, as determined by the nonlinear susceptibility tensor.

Highest reported efficiencies for an n=+1 process were around 0.2% in the experiments of Carter *et al.* [131] at the UCSB FELs. They investigated a 2.2-μm-thin quantum well film with the THz beam guided in an optimized dielectric waveguide and tuned to an excitonic hole intersubband transition. At room temperature the efficiency dropped to 3×10^{-5}.

Another possibility to break inversion symmetry and allow for n=±1 sideband generation is applying a dc voltage in the growth direction of the quantum well. Employing the dc quantum-confined Stark-effect [132], exciton energies and subband spacings can be shifted via this voltage. Different quantum well devices were investigated [133–135]. Here, the sideband signal could be maximized by changing the applied voltage and thus tuning the excitonic energy levels in resonance with the fixed NIR and THz photon energy. This behavior enables a voltage-controlled switching of the sideband generation which is technologically interesting for instance in wavelength division multiplexed (WDM) optical communication networks [136, 137].

All previous work has been performed on undoped samples. In the experiments by Carter *et al.* [21] terahertz-optical mixing in n-doped GaAs/AlGaAs quantum wells was found to be sensitive to electronic intersubband transitions instead of excitonic transitions. The maximum conversion efficiency for the doped sample was similar to an identical undoped one.

Sideband generation is not restricted to quantum well systems but has also been observed in bulk GaAs [138]. First- and second-order sidebands appeared even within the bandgap where they could not be resonantly enhanced by real energy states. Since the Stanford picosecond free-electron laser was used instead of a continuous-wave laser, the

temporal shape of the sideband could be measured by changing the time delay between the NIR and FEL pulses. It could be shown that the mixing process is coherent. This could lead to an application in THz pulse diagnostics.
So far, in most of the previously discussed experiments the THz intensity was low enough to treat sideband generation perturbatively as a $\chi^{(2)}$ or $\chi^{(3)}$ process, as has been outlined in section 2.2. In this regime the Rabi energy is much smaller than $\hbar$ times the dephasing rate γ of the system: $\mu E \ll \hbar\gamma$, where μ is the dipole moment and E is the electric field. For $\mu E \geq \hbar\gamma$ nonperturbative behavior like Rabi oscillations occur. In addition, at higher field strengths, especially in the low frequency THz range, one can enter a *strong-field regime* where the Rabi frequency becomes comparable to the photon energy: $\mu E \geq \hbar\omega$. Theoretical studies in this regime [139–142] predict shifts and splittings of absorption lines, and also nonmonotonic power dependences in nonlinear mixing. This has been investigated experimentally in asymmetric GaAs/AlGaAs quantum wells [130, 134] and bulk GaAs [138]. In reference [134] the sideband power saturated at THz field strengths of 5-10 kV/cm, decreased and began to oscillate. For its description a nonperturbative method was employed, solving the Schrödinger equation within the Floquet formalism [140, 141].
Recently, phase-matched sideband generation between the output of a THz quantum cascade laser (QCL) and a telecom laser source has been reported [143, 144]. Interestingly, the mixing was performed within the 2-3 mm long QCL cavity, demonstrating a merging of a THz device with standard telecom laser technology.
All these studies show that terahertz-optical mixing is a scientifically and technologically interesting and active area of research. As already mentioned, these results could lead to applications in voltage-controlled wavelength division multiplexers in optical communication networks, in THz pulse diagnostics and in a transfer of THz dynamics to the mature NIR region where detection is much easier.

5.2. Experimental realization

Setup

For near-infrared–terahertz mixing a tunable NIR laser is needed together with a strong tunable THz source which is the Rossendorf free-electron laser in our case (see section 3.3). Since both lasers are picosecond lasers with different repetition rates of 13 MHz and 78 MHz, respectively, an effective synchronization between these light sources is essential for our coherent experiments.
In Fig. 5.1 the experimental scheme (gray shaded area on the left hand side) is indicated together with the synchronization principle (right hand side). A tunable near-infrared (NIR) Ti:sapphire laser (*Spectra Physics: Tsunami*) is focused on the sample with a spot size of roughly 60 μm. The NIR laser running at a repetition rate of 78 MHz delivers 2.5 ps long pulses which is adjusted with an autocorrelator (*APE Berlin:*

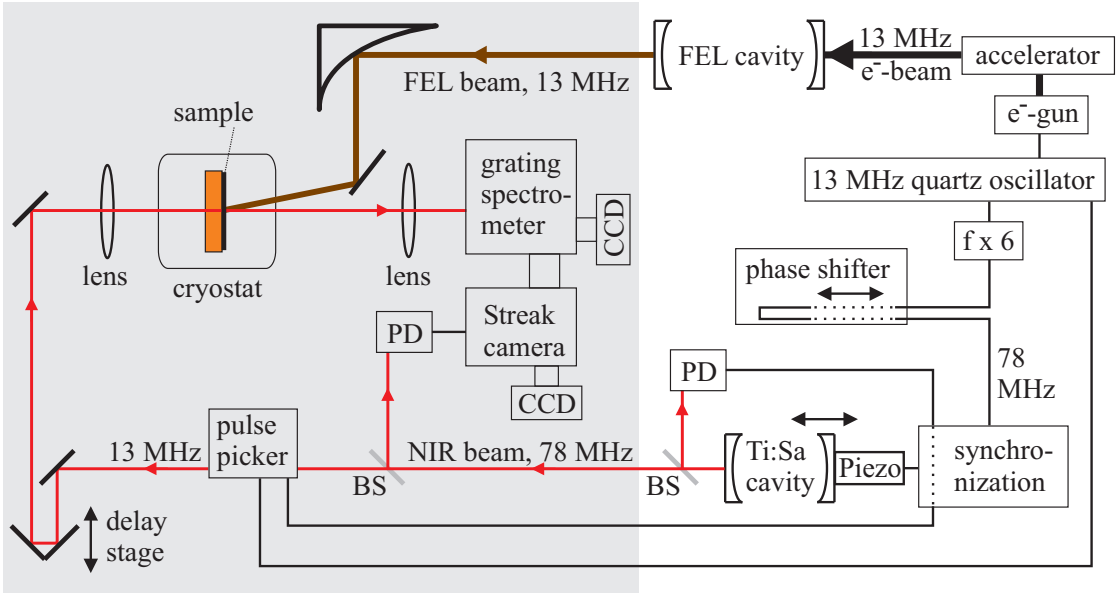

Figure 5.1.: Schematic layout of the optical setup (gray shaded area on the left hand side) and the synchronization principle (right hand side). NIR picosecond laser light is reduced in its repetition rate by a pulse picker down to the FEL repetition rate of 13 MHz. It is transmitted through the sample in a cryostat and detected with a CCD camera, attached either directly to a grating spectrometer for frequency resolution alone or to a streak camera for additional time resolution. The FEL beam is focused on the same spot on the sample as the NIR probe laser. A synchronization unit drives a piezoelectric transducer moving the NIR laser cavity end mirror to match the NIR laser repetition rate to the FEL one. A fast photo-diode (PD) behind a beam-splitter (BS) delivers the feedback signal for the synchronization loop.

PulseCheck). The laser light is transmitted through the sample and focused again on the entrance slit of a spectrometer. The CCD camera is attached either directly to the grating spectrometer for frequency resolution alone, or to the streak camera for additional time resolution (see section 3.4). In the former case the detection is more sensitive due to the low photocathode sensitivity in the streak tube (compare Fig. 3.11). As already mentioned in section 3.4 the streak camera sweep frequency has to be matched and triggered by the laser repetition frequency. The corresponding trigger signal is taken from the original NIR beam by a beamsplitter (BS) and detected with a fast Si photodiode (PD).
Sidebands only occur at the temporal overlap between NIR and FEL pulses. Via the CCD camera control software these signals can be recorded with different integration times. In addition, a background image, where the FEL pulses are coming 300 ps before the NIR pulses, is subtracted in order to suppress the stray light of the NIR laser. The peak value of the obtained signal is referred to as sideband signal in the measurements hereafter.
The sample is kept in a liquid He continuous flow cryostat (*Cryo Industries*) equipped with a 530 μm thick diamond window. CVD diamond (from chemical vapor deposition)

is transparent from the near ultraviolet to the far-infrared region (approx. 250 nm to above 500 μm [108]). The diamond window serves as entrance window for the strong FEL beam. It replaces the standard KRS-5 window that absorbs at wavelengths above 50 μm [145]. We work in the 70-200 μm wavelength range. There the FEL pulse length is around 10-25 ps. The FEL beam is focused down on the sample near normal incidence (approximately 15° from the surface normal) with an off-axis parabolic mirror of 17.8 cm focal length and overlapped with the NIR beam that is transmitted through the sample. Both FEL and NIR lasers are polarized linearly and parallel to each other. During the experiments the 78 MHz Ti:sapphire laser oscillator is phase-locked to the FEL repetition rate of 13 MHz. An ultrastable radio frequency (rf) clock based on a 13 MHz quartz oscillator drives the electron gun for the FEL. The resulting electron pulses are accelerated and after interaction in the FEL cavity with the magnetic undulator field the far-infrared light pulses are sent to the experiment. The signal from the 13 MHz quartz oscillator is now used as the reference for the NIR laser synchronization. It is multiplied by a factor of 6. The synchronization unit (*Spectra Physics: Model 3930*) takes the resulting 78 MHz signal, compares it to the current NIR laser repetition rate detected with a fast photodiode and adjusts via a feedback loop the NIR laser cavity length with a piezoelectric transducer at the Ti:sapphire cavity end mirror. Several consecutive measurements show that this synchronization has a timing jitter between FEL and NIR pulses of 1-2 ps. To control the temporal overlap between FEL and NIR pulses, a phase shifter and a variable mechanical delay stage are used before and after the NIR laser, respectively.
The pulses from the FEL and the NIR laser oscillator have different repetition rates of 13 MHz and 78 MHz, respectively, which would reduce the signal-to-noise ratio in NIR-FEL experiments. That is why an acousto-optical pulse picker (*APE Berlin: PulseSelect*) for the NIR laser is used to adjust the NIR laser repetition rate. The pulse picker gets the external trigger signal of the 13 MHz FEL clock. The temporally nearest NIR pulse is selected by diffraction in a rf driven SiO_2 crystal. One in six pulses is coupled out to the experiment while the others are suppressed. Thus, each remaining NIR pulse can interact with an FEL pulse.
The FEL peak intensity at the sample position is determined by the average power, the spot size and the FEL pulse length. The average power is measured with a power-meter (*Coherent: FieldMate* with a thermopile *PM30 sensor*). The FEL pulse length is obtained directly from the measured sideband signal when the NIR laser pulses are delayed with respect to the FEL pulses. This cross-correlation and the resulting temporal FEL pulse shape is explained below in more detail (see section 5.4). Also the spot size is determined with the actual sample by looking at the drop of the measured sideband signal when shifting the FEL spot relative to the NIR spot.

Sample

We study sideband mixing in an NIR transmission geometry. To this end we use an etched MQW film glued on a <100>-oriented ZnTe substrate, as described in section

3.5. The near-infrared transmission spectrum of the sample at a temperature of 10 K is shown in Fig. 5.2. Here, the total sample transmission with the etched quantum well film glued on the ZnTe substrate is normalized by the ZnTe substrate transmission. This spectrum is taken with a broadband fs laser (*Spectra Physics: Tsunami*) having a typical spectral width of 50 meV (25 nm). Only a small spot on the sample is probed with the laser focused down on a spot size of rougly 60 μm.
Below 1560 meV pronounced Fabry-Perot oscillations appear (with a period of $\approx$ 36 meV). At higher energies heavy-hole (hh) and light-hole (lh) exciton transitions can be distinguished [146, 147]. The most prominent transitions are related to the hh($1s$) exciton at 1566.3 meV and the lh($1s$) exciton at 1583.6 meV. At an energy of 1575 meV the onset of the hh continuum transitions can be seen, starting with the interband allowed hh($2s$) exciton state. Higher lh exciton states and the lh continuum appear above 1594 meV beginning with the lh($2s$) state.
In the transmission plot of Fig. 5.2 the hh($1s$) linewidth of 4.5 meV (FWHM) is overestimated because of the very low transmission of $\approx$ 1%. On the logarithmic scale of the absorption plot in Fig. 4.2 on page 44 the exciton line reveals a smaller linewidth of 2.7 meV. The slightly asymmetric line shape is probably due to higher excitonic states on the high-energy side. Also an inhomogeneous broadening and the inhomogeneity of the sample might contribute to the asymmetry. To some extent the spectral position of the heavy-hole exciton, but especially of the light-hole exciton varies between different spots on the sample. Hence, the laser spot averages over different spectral exciton positions which we attribute to locally different strain in the thinned quantum well film. Strain results in a shift in the GaAs bandgap and in the hh-lh splitting [148, 149]. Remember that the film is glued on ZnTe with transparent photoresist. This material combination of quantum well film, glue and substrate probably results in a change in the strain distribution with every cooldown cycle to low temperature and consecutive heating. A transmission measurement with an FTIR spectrometer (*Bruker: Equinox*

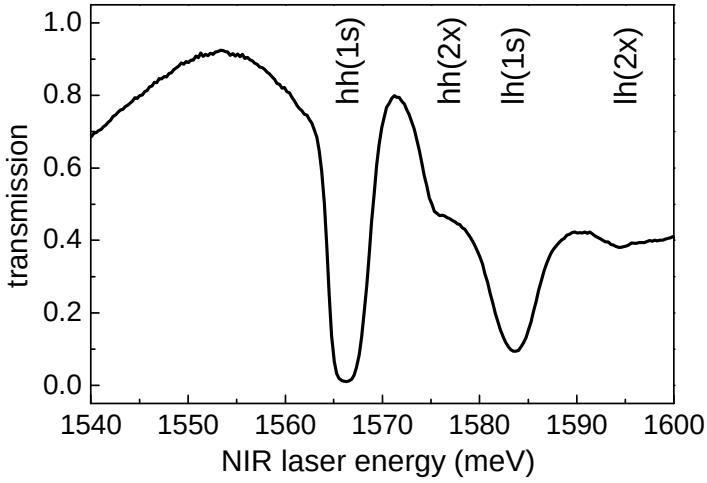

Figure 5.2.: Transmission of the etched multiple quantum well sample on the ZnTe substrate, taken at 10 K and normalized by the substrate transmission. Excitonic hh($1s$), hh($2x$), lh($1s$) and lh($2x$) transitions are indicated (x marks the s and p state).

55) also showed different hh and lh spectral positions. Furthermore, less absorption at the hh(1s) exciton and broader hh(1s) and lh(1s) linewidths were observed, which could be attributed to a much larger probe spot leading to an averaging over different spectral peak positions. Therefore, a small NIR probe spot size is favorable in our experiments to minimize the linewidth.
In our study, we demonstrate experimentally how the n=±2 sideband efficiency scales when the THz beam is tuned between interexcitonic hh(1s)-lh(1s) and intraexcitonic hh(1s-2p) transitions. To this end, we need to know the position of the hh(2p) exciton state which is optically interband forbidden, and hence does not appear in the transmission spectrum.
However, the excitonic intersubband transition between the heavy-hole 1s and 2p excitonic states is allowed and couples strongly to THz radiation [20, 96]. This allows us to measure the hh(1s-2p) transition directly [9, 90, 150, 151]. We use the setup described in section 3.2 which employs a large-area photoconductive antenna as THz emitter. Our etched sample is placed in the intermediate focus where the previous sample showing the Fano-like response has been placed (see Fig. 4.1). To obey the selection rule of the 1s-2p transition the sample is probed by the THz beam under normal incidence after resonant photoexcitation with 2.5 ps short laser pulses at the hh(1s) exciton. The transmitted THz beam is then detected by field-resolved electro-optic sampling employing a 40 μm thin <110>-oriented ZnTe crystal. Using the same experimental technique as described in section 4.2, namely chopping simultaneously near-infrared pump beam and THz probe beam, allows us to calculate the absorption α analogously (Eq. (4.4)).
In Fig. 5.3(a) the absorption α is displayed for a photoexcited carrier density of 7×10^9 cm^{-2}, a time delay between NIR pump and THz probe of 25 ps and a temperature of 6 K. First, we find an increase in absorption with lower THz photon energy. This can be simulated with a simple Drude model for free-carrier absorption, where the absorption α depends on the frequency ω and the free-carrier scattering time γ_c^{-1} via [122, p. 249]

$$\alpha \propto \frac{1}{\omega^2 + \gamma_c^2}. \tag{5.1}$$

The blue curve in Fig. 5.3(a) shows the Drude model for a momentum relaxation time of γ_c^{-1}=0.8 ps. This value lies near reported ones for a similar material system which are around 0.5 ps [152] and 0.3 ps [9].
Differently from the Drude-like free-carrier absorption we find an onset of increased absorption above an energy of 7 meV, which is due to the internal transition between the 1s and 2p bound states, as well as transitions from the 1s state to higher bound and continuum states. For a better evaluation we have subtracted the Drude-like background in Fig. 5.3(b). In a simulation in reference [93] the 1s exciton absorption spectrum is calculated for different linewidths. With increasing linewidth the peak absorption is shifted to higher energies because of transitions to higher excited states and the continuum. However, the 1s-2p transition should stay at a constant energy. Therefore, an assignment of our measured 1s absorption spectrum with its limited signal-to-noise ratio is difficult. We assume a linewidth of the 1s-2p transition of $\approx$ 3

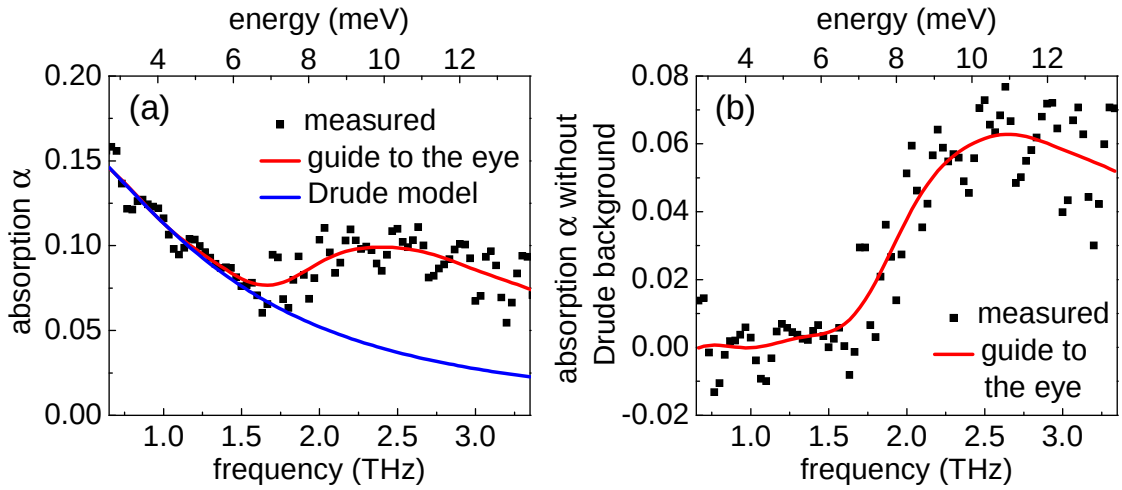

Figure 5.3.: (a) Sample absorption 25 ps after photoexcitation at the heavy-hole 1s exciton for a carrier density of 7×10^9 cm^{-2} at a temperature of 6 K. On the Drude-like free-carrier absorption (blue line) the heavy-hole 1s-2p transition and the transitions from the 1s to higher states are superimposed. (b) 1s THz absorption spectrum after subtraction of the Drude background. We deduce a 1s-2p resonance of $\approx$ 9 meV with a linewidth of $\approx$ 3 meV.

meV which corresponds to the 2.7 meV linewidth of the hh(1s) exciton absorption that was found in the NIR transmission measurement. For this linewidth we also find a good agreement of our overall absorption shape with the simulation [93]. Since the 1s-2p transition marks the onset of absorption, we deduce a 1s-2p transition energy of roughly 9 meV by comparison with reference [93]. The maximum 1s absorption occurs above that value where the absorption into higher states and the continuum is superimposed.

5.3. Temporal overlap between FEL and NIR laser via PL quenching

The sideband signal is found only at the temporal overlap between the 2.5 ps short NIR pulses and the up to 25 ps long FEL pulses. At a repetition rate of 13 MHz consecutive NIR or FEL pulses follow every 77 ns. Therefore, finding the temporal overlap is crucial.

For a first rough alignment the FEL pulses are detected with a fast and sensitive infrared detector. We use a biased superlattice detector [153, 154]. It operates at room temperature and covers the whole long-wavelength range above 40 μm of the U100 FEL with a sensitivity increasing with wavelength according to λ^4 [154]. Compared to other fast detectors like those based on the photon-drag effect [155] the superlattice detector sensitivity is up to four orders of magnitude larger at an intrinsic temporal resolution

below 1 ps [154]. It consists of an n-doped GaAs/AlAs superlattice structured into mesas. Via an L-shaped antenna and a corner cube reflector the FEL radiation is coupled into the heterostructure with the electric field in growth direction. A dc bias is applied across the superlattice with a voltage just below the onset of negative differential resistance. The frequency of the resulting Bloch oscillations is modulated under FEL illumination [156]. This leads to a change in the dc current which is extracted via a bias tee and recorded by a fast oscilloscope. The NIR laser pulses are detected with a fast photodiode and overlapped with the FEL pulse signal. This approach determines the temporal overlap with an estimated accuracy better than ± 300 ps which is limited by the oscilloscope bandwith and the detector signal risetimes.
For a fine tuning of the temporal and also the spatial overlap the actual sample is taken. To this end the sample's time-resolved photoluminescence (PL) is recorded with the streak camera. The FEL pulse can induce an ultrafast transient quenching of the excitonic PL, resulting in a dip in the heavy-hole PL dynamics that can be maximized to maximize the spatial overlap. In Fig. 5.4(a) the heavy-hole PL is displayed in a false color image after nonresonant ps laser excitation with a peak intensity of 680 kW/cm^2 at 766 nm. Here, the 38° wedged waveguide sample is used. It ensures an effective coupling of the THz beam to the intersubband transition (11 μm) where the FEL wavelength is tuned to. Without FEL the undisturbed PL decays with a time constant of approximately 880 ps. Under FEL illumination the PL decay is temporarily suppressed during and shortly after the FEL pulse. This can be observed even at very low FEL average powers of 0.4 mW, corresponding to an estimated peak intensity of 18 kW/cm^2. Figure 5.4(b) displays the extracted decay curves for the waveguide

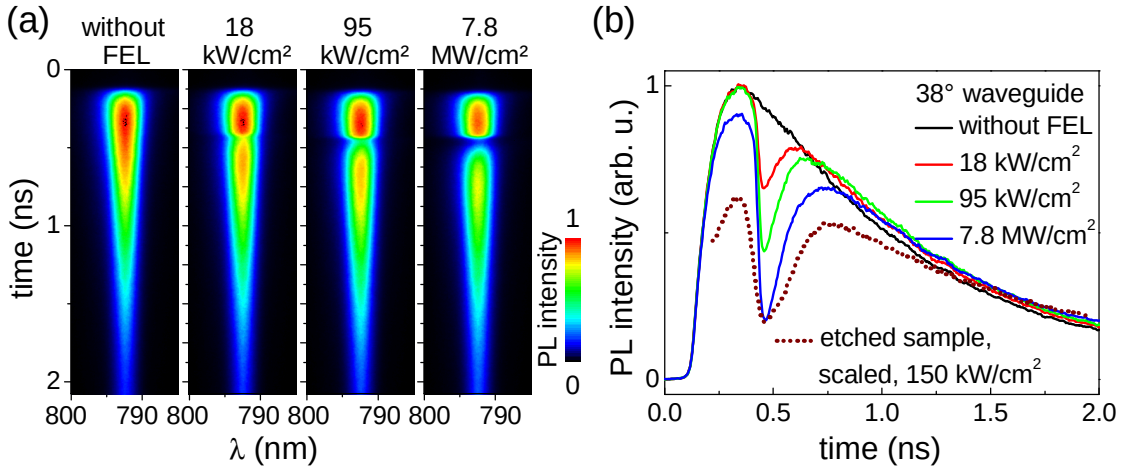

Figure 5.4.: FEL-induced quenching of the quantum well heavy hole photoluminescence at a temperature around 15 K. (a) PL false color plot without and with FEL illumination at different peak intensities for a 38° wedged waveguide and an FEL wavelength at the intersubband resonance of 11 μm. (b) Extracted PL decay curves. In addition, the PL of the etched sample is shown, illuminated under normal incidence at an FEL wavelength of 72.6 μm, corresponding to the hh(1s)-lh(1s) transition energy.

geometry. Additionally, the decay curve for the etched sample under normal incidence is given, where the FEL was tuned to 72.6 μm which corresponds to the hh($1s$)-lh($1s$) transition energy of 17.1 meV. Actually, sidebands are later observed in this configuration. In all cases a rapid drop in the PL on a time scale similar to the FEL pulse length can be seen. Due to the increased FEL pulse length at 72.6 μm the time scale on which the PL drops to a minimum is longer for the etched sample.
In the literature quenching of excitonic quantum well photoluminescence has been performed so far only for in-plane polarized far-infrared radiation [152, 157] or recently as NIR optically induced PL quenching [158]. In both cases the dominant effect was an induced heating of the free carriers which could be described by a Drude model. A significant heating of the lattice was not observed. Also no resonant PL quenching occurred in a GaAs/AlGaAs multiple quantum well when the FEL photon energy was scanned across the excitonic $1s$-$2p$ or the hh-lh transition [152]. Thus, we also suggest that our observed quenching in both intersubband active waveguide geometry and normal-incidence geometry is at least partly due to FEL-induced heating of free carriers.
After free-carrier absorption a thermalization towards an elevated temperature of the exciton population occurs on a time scale of a few hundred fs [159] directly during the relatively long FEL pulse (FWHM of 1 ps at 11.1 μm and 12 ps at 72.6 μm). A higher carrier temperature leads to a lower occupation of the center-of-mass momentum states $\mathbf{K} = 0$. Only these states decay radiatively [160]. Therefore, the PL is suppressed, but recovers while the population cools down. This cooling takes longer for increasing FEL power, as can be seen in Fig. 5.4(b). Hereafter, the PL strength even exceeds the original PL without FEL illumination since the total number of excitons has been conserved[1]. Note that for the etched sample one observes a larger PL rise time, and after the FEL-induced PL quenching also a longer cooling time and total PL decay constant. The excitation intensity was lower here by a factor of two, which could explain these differences. Also note that a high-energy tail in the spectrum after PL quenching due to hot carriers can only be seen in a logarithmic plot (not shown) and is not visible in Fig. 5.4(a).
However, in our line of argument we neglected the contribution of the electron-hole plasma to the PL [160]. Moreover, a detailed study would require to investigate PL quenching for different FEL polarizations, wavelengths and temperatures to clarify whether this effect is resonantly enhanced at internal excitonic or intersubband transitions and whether other mechanisms than free-carrier heating could be responsible. Such experiments are beyond the scope of this work. For our purpose the quenching signal allows for a clear and simple determination of the temporal overlap and has been used successfully in quantum wells, dots and superlattices.

[1] This was confirmed by integration over the additional PL temporally after the FEL-induced PL dip. The obtained area equals the area of the dip.

5.4. Experimental results and discussion

Comparison between sidebands and photoluminescence

In Fig. 5.5 the n=−2 sideband is compared with the time-integrated photoluminescence. The FEL is tuned to the hh($1s$)-lh($1s$) transition at 17.1 meV (72.6 μm) with a peak intensity of 47 kW/cm^2. The NIR laser photon energy is 1592.1 meV and the estimated photoexcited electron-hole pair density is 1×10^{10} cm^{-2}. At the temporal overlap of NIR and FEL pulses the black line shows the n=−2 sideband at 1558 meV and the broad photoluminescence at 1565 meV. The sideband is exactly found two FEL photon energies below the NIR fundamental. The linewidth of the sideband corresponds to the NIR laser linewidth and is not connected to the broad PL linewidth. Shifting the temporal overlap in such a way that the FEL pulses run ahead of the NIR pulses by 300 ps makes the sideband vanish while the broad PL is not affected (red dots). Remember that the sideband signals discussed below are recorded by subtracting such a background where the FEL pulses come before the NIR pulses.
For comparison, the green line shows the PL signal without FEL illumination. While the PL peak does not shift noticeably, the center of gravity shifts to lower energies. We attribute the resulting asymmetric PL line shape to excitons trapped on interface defects [161]. The luminescence spectra with and without FEL illumination reveal slightly different carrier temperatures T_c, that can be deduced from the slope of the high-energy tail of the PL spectrum [162]. In this region the intensity I decreases with the NIR photon energy $\hbar\omega$ according to the Maxwell-Boltzmann distribution $I \propto \exp[-\hbar\omega/(k_B T_c)]$. Exponential fits yield carrier temperatures of 20 K with and 12 K without FEL illumination. The FEL-induced carrier heating probably comes from a lattice heating since

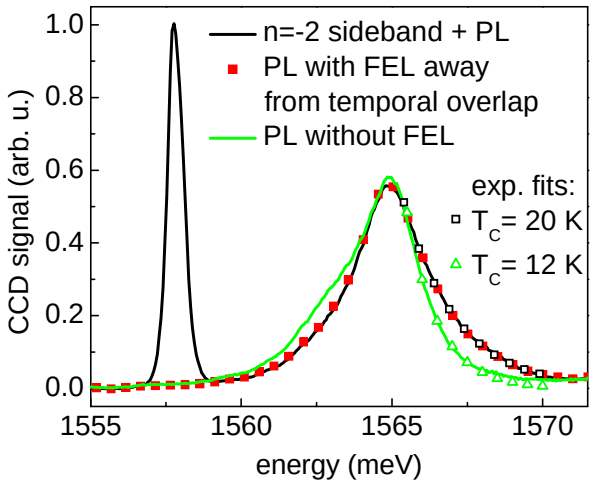

Figure 5.5.: Narrow n=−2 sideband signal and photoluminescence of the hh($1s$) state. From an exponential fit of the high-energy tail of the PL spectrum the carrier temperature T_c can be deduced (open green triangles and open black squares for 12 K and 20 K, respectively).

the PL line shape is not altered when the FEL pulses precede the NIR pulses or overlap with them. However, even the small temperature difference with and without FEL irradiation should lead to a GaAs bandgap shift of 0.6 meV [163] which is not seen. Such a temperature independent luminescence line for temperatures below 30 K has been observed before [164] and was attributed to the temperature dependent detrapping of the excitons bound to interface defects.
The difference between the spectral position of the PL at 1565 meV and the hh($1s$) exciton absorption at 1566.3 meV (see Fig. 5.2) is attributed to a small Stokes shift.

Temporal shape of the sideband signal

As already mentioned briefly (see Fig. 5.5), sideband generation is a coherent process, i.e. sidebands appear only at the temporal overlap of the involved NIR and FEL pulses. Especially, they are not found when this coherence is lost and only populations are present, which can decay via photoluminescence. The temporal behavior has been demonstrated by Zudov and coworkers [138] in bulk GaAs by employing picosecond NIR and THz pulses and shifting the temporal delay between them.
Since we have a streak camera system with a time resolution of several picoseconds, we can measure the temporal behavior of the sideband signal. Figure 5.6(a) displays the attenuated NIR fundamental pulse (black line) and the n=+2 sideband signal (red line). The FEL energy was 17.1 meV close to the heavy-hole light-hole splitting energy and the NIR energy was at the hh($1s$) transition with a pulse length of 2.5 ps. Both fundamental and sideband pulses were taken separately in the streak camera's time-resolved mode and shifted afterwards to overlap with each other. Thus, the relative

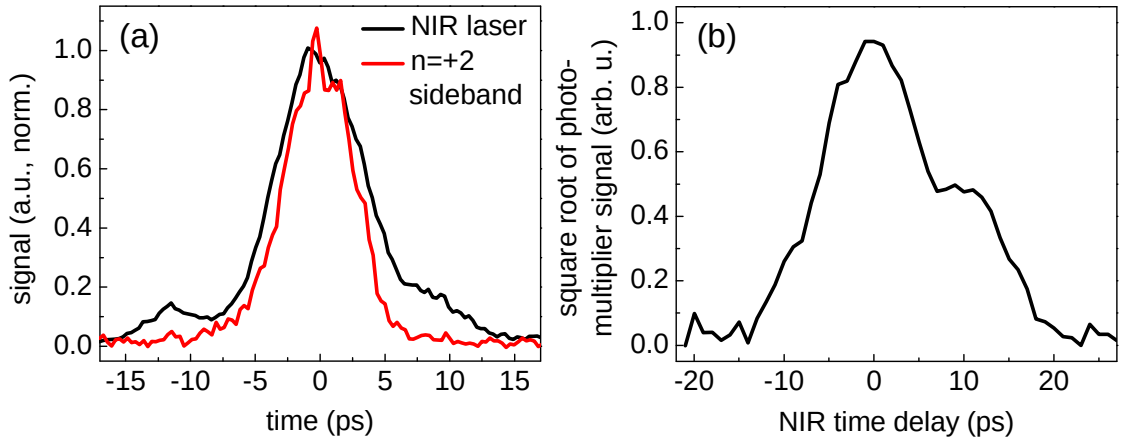

Figure 5.6.: (a) Time-resolved NIR laser pulse (black line) and n=+2 sideband signal (red line) recorded with the streak camera. Note that both signals have been recorded separately and shifted afterwards to overlap with each other. (b) FEL pulse shape extracted as the square root of the n=+2 sideband signal while the delay between NIR and FEL pulses was varied.

time delay between NIR pulse and sideband signal cannot be extracted. Note that the additional small pulses at -12 ps and +10 ps before and after the main NIR pulse are most likely artefacts from the attenuator we used.
In order to separate the weak sideband signal from the far stronger fundamental we chose a grating with 300 lines/mm which does not provide the optimal time resolution. Therefore, the apparent fundamental pulse length is of the order of 8 ps compared to the initial 2.5 ps. The sideband signal has a reduced temporal width of around 6.5 ps. However, due to the limited time resolution we cannot directly compare its temporal width with the NIR pulse. We can only state that the sideband signal is not connected to a long-lasting photoluminescence decay. Additionally, it is shorter than the involved FEL pulse that is plotted in Fig. 5.6(b). The FEL pulse shape has been taken from a cross-correlation measurement. Here, the n=+2 sideband intensity was recorded with an integrating photomultiplier tube, a Lock-In amplifier and a chopped FEL beam while the NIR laser was delayed via a mechanical delay stage. Hence, for every time delay the shorter NIR pulse samples the longer FEL pulse envelope. n=±2 sideband generation is described by a $\chi^{(3)}$ process. Assuming parallel propagation with linear and parallel polarization of both the NIR and FEL light along the x-axis, the nonlinear polarization $P^{(3)}$ for n=+2 reads (see Eq. (2.12)):

$$P_x^{(3)}(\omega_{\mathrm{NIR}} + 2\omega_{\mathrm{THz}}) = 6\epsilon_0 \chi^{(3)}_{xxxx}(\omega_{\mathrm{NIR}} + 2\omega_{\mathrm{THz}}, \omega_{\mathrm{NIR}}, \omega_{\mathrm{THz}}, \omega_{\mathrm{THz}}) E_x(\omega_{\mathrm{NIR}}) E_x(\omega_{\mathrm{THz}})^2. \tag{5.2}$$

The sideband signal $I_{n=+2}$ follows from solving the wave equation (2.5) with $P^{(3)}$ as source term. Neglecting the NIR sampling pulse width with respect to the longer FEL pulse width, the cross-correlation $I_{n=+2}(t)$ with the time delay t is quadratic in the FEL intensity. Therefore, we take the square root to obtain the FEL pulse shape of Fig. 5.6(b). The additional shoulder 10 ps after the FEL pulse maximum is believed to be mainly due to a pulse distortion from water absorption and less to a reflection within the ZnTe substrate on which the investigated quantum well film was glued. With a refractive index of 3.6 a reflection at the rear air-ZnTe boundary is expected to transmit through the quantum well film again after 12 ps. However, the additional shoulder was sometimes unexpectedly strong and had 70% of the height of the main pulse. In other measurements it vanished or an additional pulse 30-40 ps after the main one appeared. Hence, a pulse distortion via water absorption is most likely.
The obtained FEL cross-correlation signals and extracted pulse lengths are used to determine the FEL peak powers. The FEL spot size is also taken from the measured sideband signal. With the NIR probe spot fixed on the sample the FEL spot is moved to the two opposite locations on the sample where the total sideband signal drops to half of its maximum value. We assume a Gaussian spatial profile $I(x, x_0, d) \propto \exp[-2\ln(4) \cdot (x - x_0)^2/d^2]$ for both NIR and FEL pulses with different spot sizes with a FWHM d. While changing the distance z between FEL and NIR spot, the resulting intensity for the n=±2 sidebands $I_{n=\pm2}(z)$ is given by

$$I_{n=\pm2}(z) \propto \int I(x, x_0, d_{\mathrm{NIR}}) I(x, x_0 + z, d_{\mathrm{FEL}})^2 dx. \tag{5.3}$$

The unknown spot size d_{FEL} follows from comparing the measured FWHM of $I_{n=\pm 2}(z)$ with the width of the obtained intensity profile from Eq. (5.3) for the fixed NIR spot size $d_{\mathrm{NIR}} \approx 60$ μm. According to this approach the FEL spot sizes for the main FEL wavelengths used hereafter are determined to be ≈ 0.8 mm at 73 μm and ≈ 1.5 mm at 139 μm.

Sideband spectrum and intensity dependencies

In Fig. 5.7 a typical low-temperature sideband spectrum is measured under FEL illumination with the NIR laser tuned near the hh(1s) exciton energy. The FEL has been tuned to an energy of 8.9 meV near the heavy-hole 1s-2p transition with a peak intensity of 65 kW/cm^2. The NIR peak intensity is around 3 kW/cm^2. The indicated conversion efficiency is defined as the ratio between emitted sideband intensity and incoming NIR fundamental intensity which was corrected for the losses in the ZnTe substrate. Thus, it specifies the nonlinear conversion of the thinned quantum well film alone.
Different even orders of sidebands can be observed. They are found at even integer multiples n of the FEL photon energy $\hbar\omega_{\mathrm{THz}}$ on the high- and low-energy side around

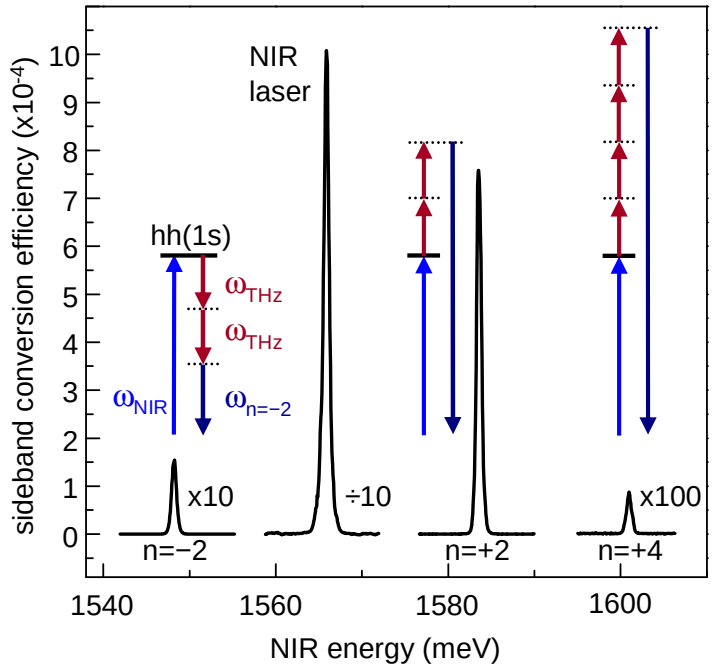

Figure 5.7.: Transmitted sideband spectrum at 10 K for an FEL peak intensity of 65 kW/cm^2 and $\hbar\omega_{\mathrm{THz}} = 8.9$ meV near the heavy-hole 1s-2p transition. For clarity, the n=−2 and n=+4 sidebands are multiplied by 10 and 100, respectively, and the NIR laser is divided by 10. Energy level diagrams illustrate the involved transitions schematically with respect to the hh(1s) transition.

the fundamental NIR laser line $\hbar\omega_{\mathrm{NIR}}$: $\hbar\omega = \hbar\omega_{\mathrm{NIR}} + n \times \hbar\omega_{\mathrm{THz}}$. This reflects energy conservation. Energy level diagrams illustrate schematically where the involved levels lie in the corresponding parametric process with respect to the hh($1s$) transition. The n=−2 sideband process for instance includes an NIR photon transition to the hh($1s$) exciton and from there two transitions to lower lying virtual energy levels mediated by FEL photons. From the lowest virtual level the n=−2 sideband photon is emitted with an energy of $\hbar\omega_{\mathrm{n=-2}} = \hbar\omega_{\mathrm{NIR}} - 2\hbar \times \omega_{\mathrm{THz}}$. The n=+2 sideband also involves two FEL photons, but the emitted sideband is higher in energy than the incoming NIR fundamental. As we will discuss later on, the n=+2 sideband is resonantly enhanced when the FEL is tuned to the heavy-hole $1s$-$2p$ transition.
Our study is restricted to sidebands in the vicinity of the NIR fundamental, i.e. to those mixing processes where exactly one NIR photon is involved. Nevertheless, also other nonlinear processes should occur, for instance where two NIR photons mix with one FEL photon. These processes lie energetically beyond the observed range.
Note that the relative intensity of the peaks depends on the spectral position of the fundamental. The highest efficiency occurs whenever a final or intermediate level involved in the mixing process is resonant with a real energy level of the system investigated. And since the sidebands of different orders are found at different spectral positions, they are resonantly enhanced differently according to the presence of a real energy level in the vicinity. This will be demonstrated later in more detail.
Due to slight asymmetry of the quantum wells resulting from MBE growth, also the odd sidebands n=±1 appear with typical intensities 1000 times smaller than n=±2 (not shown here). In a purely symmetric multiple quantum well they should be forbidden, as can be seen from Eq. (2.21) and the corresponding Fig. 2.5(a) on page 12. For our case of two interband transitions (IBTs) connected by an intermediate intersubband transition (ISBT) the susceptibility $\chi^{(2)}$ is proportional to the product of the respective dipole matrix elements μ with the ground state g: $\chi^{(2)} \propto \mu_{gn}^{\mathrm{IBT}} \mu_{nm}^{\mathrm{ISBT}} \mu_{mg}^{\mathrm{IBT}}$. In order to have resonance enhancement for the n=±1 sideband all the dipole matrix elements should be strongly allowed. In symmetric quantum wells allowed interband transitions occur between states of identical parity, whereas intersubband transitions require states of different parity (see appendix A). Consequently, the last transition matrix element μ_{mg}^{IBT} vanishes and therefore $\chi^{(2)} = 0$ when μ_{gn}^{IBT} and μ_{nm}^{ISBT} are nonzero. Only breaking the symmetry can lead to allowed odd sidebands. For even sidebands an additional transition is involved (see Eq. (2.22)). Thus, an interband transition is followed by two intersubband transitions so that the last interband transition is allowed again.
Figure 5.8(a) depicts the measured sideband efficiency as a function of the THz peak intensity at a fixed NIR peak intensity of 3 kW/cm^2. In this double logarithmic plot the n=+2 sideband signal can be fitted by a purely quadratic function for low THz intensities. Above 40 kW/cm^2 the signal begins to saturate. The saturation is probably due to an FEL-induced Autler-Townes splitting of the hh($1s$) exciton, which already starts at ≈ 50 kW/cm^2 (see Fig. 6.3(b) on page 93 in chapter 6). Hence, a decrease in the sideband signal occurs when the hh($1s$) exciton is brought out of resonance. Furthermore, the $2s$ excitonic shoulder smears out due to a beginning exciton dissociation

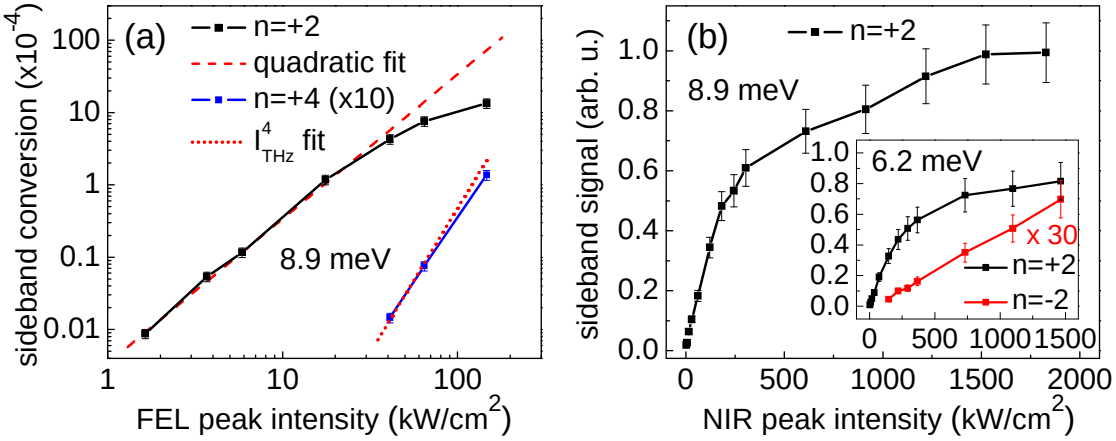

Figure 5.8.: (a) Sideband conversion efficiency as a function of the FEL intensity. Both n=+2 (black line) and n=+4 (blue line) processes show the expected dependency, as indicated by a quadratic (red dashed line) and I^4_{THz} (red dotted line) fit. The n=+4 signal was multiplied by 10. (b) Sideband signal as a function of the NIR peak intensity. The n=+2 sideband signal is linear for small NIR intensities for an FEL photon energy of 8.9 meV. For a THz energy of 6.2 meV the n=±2 sideband signals are given in the inset (the titles of the axis are identical). The n=−2 sideband (scaled by a factor of 30) does not saturate while the n=+2 one does. Probably the transition to the $2p$ state could be Pauli-blocked for n=+2 processes.

which means that a broadening and dissociation of the $2p$ state as intermediate level during the nonlinear mixing could also reduce the mixing efficiency.

The deviation from a quadratic dependence for higher THz intensities is probably not caused by a breakdown of the perturbative treatment [130, 134, 138]. In this so-called *strong-field regime* the ponderomotive potential U_p which is the time-averaged kinetic energy of an electron moving in an ac electric field becomes comparable to the THz photon energy [97, 165]. U_p is given as $U_p = e^2 E^2_{\mathrm{THz}}/(4m^*\omega^2_{\mathrm{THz}})$ with the effective mass m^* and the electric field E_{THz}. Assuming an electric field to intensity relation from a plane wave $I = \frac{1}{2}\epsilon_0 c_0 n_{\mathrm{THz}} E^2_{\mathrm{THz}}$ one obtains for a THz energy of $\hbar\omega_{\mathrm{THz}} = 8.9$ meV and an intensity of 100 kW/cm^2 (corresponding to a field strength of $E_{\mathrm{THz}} \approx 3.8$ kV/cm (30% reflection losses, $n_{\mathrm{THz}} = 3.6$ [61])) a value $U_p \approx 0.6$ meV. This is one order of magnitude smaller than the THz photon energy, which is why a perturbative description of sideband generation should still be valid.

The n=+4 sideband process requires four FEL photons. Its description is based on the nonlinear polarization $P^{(5)}$ with the susceptibility $\chi^{(5)}$. Hence, the n=+4 sideband signal should obey $I_{n=\pm4} \propto I_{\mathrm{NIR}} I^4_{\mathrm{THz}}$. This dependence is confirmed in Fig. 5.8(a) where the n=+4 signal (blue dots) is plotted together with a purely I^4_{THz} fit function. Note that only few data points are given due to the very weak signal.

The NIR dependency of the n=+2 sideband at a THz peak intensity of 8 kW/cm^2 is illustrated in Fig. 5.8(b). For small intensities the signal rises linearly with the NIR intensity. Above approximately 250 kW/cm^2 saturation starts. Our experimental comparison of n=±2 sideband generation for intraexcitonic and interexcitonic transitions

uses an NIR peak intensity of 180 kW/cm^2 which is within the linear regime. This intensity corresponds to an maximum heavy-hole exciton density of 3×10^{10} cm^{-2}. A measurement with 10% of this relatively high exciton density has also been taken, but the trends presented here stayed the same and only a reduced linewidth by a factor of 0.8 in the resonance scans hereafter has been observed.
The saturation of the sideband signal with increasing NIR excitation intensity can result from a reduced number of available free states in the conduction band via phase-space filling and Pauli-blocking of the NIR fundamental. Indeed the transmitted NIR light at the strongly absorbing hh($1s$) exciton increased by a factor of 1300 while the NIR intensity is only increased by a factor of 60 to reach 180 kW/cm^2, indicating already a significant bleaching of the hh($1s$) transition. However, the sideband power goes linearly with NIR intensity below 250 kW/cm^2 which is why the Pauli-blocking of states for the NIR fundamental does not seem to contribute significantly to the saturation. One explanation could be the increasing absorption of the THz radiation. In our case the THz energy is resonant with the $1s$-$2p$ transition. Hence, the $2p$ state can be populated, which prevents the $1s$-$2p$ transition due to Pauli-blocking in the phase space. Additionally, THz photons can be lost for the mixing process when they are absorbed in free-carrier absorption. The inset of Fig. 5.8(b) plots the $n=\pm2$ sideband signal for another FEL energy of 6.2 meV, slightly below the $1s$-$2p$ resonance, but also excited at the hh($1s$) exciton with a THz peak intensity of around 6 kW/cm^2. The decreased THz photon energy should not matter, since the $1s$-$2p$ transition has shown a linewidth of 3 meV (see Fig. 5.3). While the $n=+2$ behavior is exactly the same as before the $n=-2$ sideband signal goes linearly with NIR peak intensity. This would support the explanation that THz absorption of the $2p$ state and higher states are mainly responsible for the saturation. A THz free-carrier absorption alone and a Pauli-blocking of states for the NIR fundamental, as also proposed in reference [138], would equally influence $n=\pm2$ sideband generation. An alternative explanation for the sideband saturation with increasing NIR intensity could be a transition from an excitonic regime to an electron-hole plasma. At high excitation densities exciton formation is hindered by screening [166]. Thereby, the $1s$-$2p$ resonance that is necessary for efficient $n=+2$ generation vanishes. This leaves the non-resonant $n=-2$ sideband unaffected.

Conversion efficiency

From Fig. 5.8(a) a maximum $n=+2$ sideband conversion efficiency of 0.13% for an FEL peak intensity of 145 kW/cm^2 can be seen. This is a relatively high value which is due to resonance enhancement at the intraexcitonic hh($1s$-$2p$) transition. It lies in the range of the highest reported efficiency in the literature of 0.2% for an $n=+1$ sideband in an asymmetric coupled GaAs/$Al_{0.3}Ga_{0.7}$ quantum well structure for an FEL peak intensity of 90 kW/cm^2 [131]. By comparison, the second-order $n=+2$ sideband efficiency in this structure has been reported to lie at around 0.006%. An excitonic hole intersubband transition was exploited in that work. Therefore, the FEL radiation was

coupled into the quantum wells via the cleaved edge of the sample which was placed between sapphire plates to form a dielectric waveguide for the FEL radiation. Thus, the intrinsically more efficient lower-order nonlinear n=+1 sideband process requiring a more complicated coupling to the THz radiation shows only slightly higher efficiency in contrast to our normal-incidence THz coupling and higher-order n=+2 mixing.

Phase-matching

Nonlinear optics is limited in most cases by the phase-mismatch between the mixing beams. Applied to our case (n=+2 sideband) the phase-matching condition reads

$$\Delta k = 2 \times k_{\mathrm{THz}} + k_{\mathrm{NIR}} - k_{\mathrm{n=+2}} \approx -8.1 \times 10^4 \mathrm{m}^{-1}, \tag{5.4}$$

with $k_i = 2\pi n_i/\lambda$, λ_{THz}=139 μm, λ_{NIR}=791 nm, $\lambda_{\mathrm{n=+2}}$=782.1 nm and the corresponding refractive indices n_{THz}=3.60 [61], n_{NIR}=3.61 and $n_{\mathrm{n=+2}}$=3.62 [167]. This defines the coherence length L_c after which the intensity of the mixing signal ($\propto \sin^2(\Delta k L/2)/(\Delta k L/2)^2$, compare Eq. (2.29) which is quite a universal factor for different nonlinear mixing processes) drops to approximately 40%: $L_c = |\pi/\Delta k| \approx 40$ μm. This is much larger than the width of the active quantum well structure of 1.7 μm. Hence, nearly perfect phase-matching is present.
Nevertheless, the vector character of the phase-matching condition has been observed indirectly in the sense that the lens collecting the sideband signal in front of the spectrometer has to be moved slightly when going from n=+2 to n=−2. Additionally, the lens positions for maximum n=±2 signal were further apart for an FEL wavelength of 73 μm than for 139 μm. Since the NIR laser and the FEL beam do not travel collinearly (the FEL beam illuminates the sample under a small angle of 15° with respect to the quantum well film normal), the "+" and "−" sideband signals do not propagate parallel. However, the NIR and FEL wavelengths and thus their wavevectors differ by two orders of magnitude. It is quite surprising that this change can be seen. It also implies a significant aberration of the lens.

Polarization selection rules

With the NIR laser polarized linearly and with its photon energy at the hh(1s) exciton, highest conversion efficiency is achieved when the FEL is linearly polarized. Thereby, the efficiency is approximately identical for the FEL and NIR polarizations perpendicular or parallel to each other. Furthermore, the sideband light polarization state follows the NIR laser one, when the latter one is circular or is turned by 90° in case of linear polarization. Note that we do not distinguish between right- and left-circularly polarized light in the experiment. For circularly polarized FEL light the n=+2 sideband power drops to 0.6. A similar polarization dependence has been observed by Kono *et al.* [20] for n=±2 sidebands between magnetoexcitonic transitions. Its explanation [127]

was based on the evaluation of symmetry rules of the nonlinear susceptibility tensor $\chi^{(3)}$. Since their system consisted completely of heavy-hole intraexcitonic transitions and also an external magnetic field was applied, we probably cannot assume exactly the same selection rules in our system. However, an evaluation of the $\chi^{(3)}$ tensor and its symmetry properties that are determined by its constituent transition matrix elements (see Eq. (2.22)) between excitonic heavy-hole states and excitonic heavy-hole and light-hole states is beyond the scope of this work.

Resonance scans with the FEL photon energy tuned between inter- and intraexcitonic transition

By tuning the NIR wavelength one can get valuable information about the energy levels involved in sideband mixing. In Fig. 5.9(b) the FEL photon energy is fixed at the interexcitonic hh(1s)-lh(1s) transition at an energy of 17.1 meV. NIR and FEL peak intensities are 180 kW/cm^2 and 18 kW/cm^2, respectively. While varying the NIR photon energy the n=±2 sideband power is measured at each spectral NIR laser position. Note that the spectral position $\omega_{n=\pm2}$ of the recorded sideband signal differs always by two FEL photons from the corresponding NIR laser position ω_{NIR}. This simply reflects energy conservation.
In Fig. 5.9(b) several resonances can be seen. Their origins become clear by comparing them with the sample transmission already presented earlier (Fig. 5.2), but given again in Fig. 5.9(a) for convenience. Here, we give a qualitative description in the form of schematic energy level diagrams, illustrating the involved transitions.
The strongest resonance for the n=+2 sideband (black line) is found at 1557 meV slightly below the band edge. One FEL photon energy above we find the hh(2s) and hh(2p) states in the transmission spectrum, serving as an intermediate state for the mixing. The relative strength of the resonance peak shows that the 1s-2p transition couples strongly to the THz radiation, although the NIR laser is only resonant with a virtual level within the bandgap. The corresponding final state lies in the continuum above the lh. The whole process including virtual and real energy levels is depicted in the schematic level diagram. The sideband resonance signal at the hh(1s) state is smaller, although one FEL photon is resonant with the hh(1s)-lh(1s) transition. However, for small in-plane wavevectors this transition is weak [168]. The third resonance at the lh(1s) position is less pronounced, since the FEL-induced transitions couple the lh exciton to continuum states and not to sharper excitonic states like in the aforementioned cases. Note that the 2s heavy-hole state does not lead to a pronounced feature in the sideband resonance scan, although it is an NIR interband optically allowed transition.
The n=−2 sideband spectrum is consistent with this picture, showing highest conversion signal when the NIR laser is tuned 17.1 meV above the hh(2p) state. Hence, we find that the hh(2p) state as an intermediate state for the nonlinear mixing dominates both the n=+2 and n=−2 sideband spectra.
To make use of the obviously enhanced THz coupling to the hh(2p) state, we now ad-

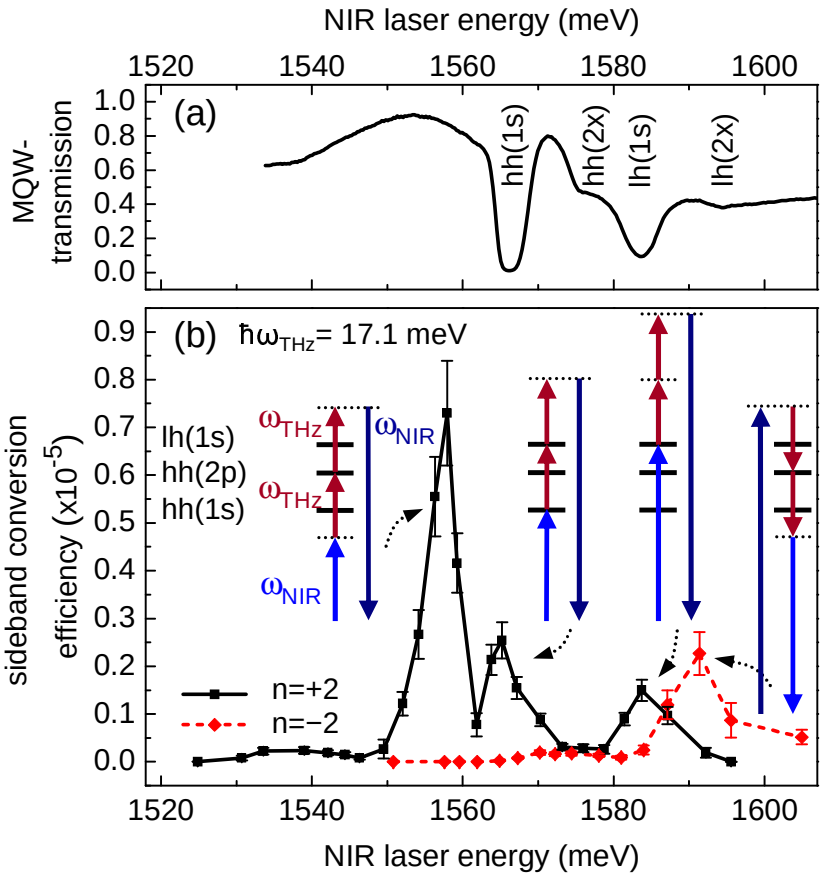

Figure 5.9.: (a) Multi quantum well film transmission spectrum from Fig. 5.2 (x marks the s and p state). (b) Sideband spectra for n=+2 (black line) and n=−2 (red dashed line) for an NIR peak intensity of 180 kW/cm^2, an FEL peak intensity around 18 kW/cm^2 and an FEL energy of 17.1 meV, corresponding to the hh(1s)-lh(1s) transition. Schematic level diagrams indicate the involved transitions.

dress the case where the FEL energy is fixed at 8.9 meV near the estimated hh(1s-2p) resonance. The corresponding NIR sideband spectrum is given in Fig. 5.10. At the lh(1s) state the n=+2 spectrum shows a weak resonance at ≈ 1582 meV (black curve) whose origin is the same as discussed before. However, the signal has increased by a factor of three which can be explained by resonance enhancement of the lh(1s-2p) transition. An even greater enhancement by a factor of 20 can be seen at the heavy-hole 1s exciton compared to the aformentioned case of resonance with the interexcitonic hh(1s)-lh(1s) transition. Now the FEL photon energy is resonant with the hh(1s-2p) transition and also approximately with the subsequent hh(2p)-lh(1s) transition. Furthermore, the final NIR transition involves the lh(1s) state which is also pronounced in the NIR transmission spectrum and thus has a large dipole transition matrix element. This also means that the emitted sideband photon can be absorbed at the lh(1s) state reducing the conversion efficiency. Nevertheless, all virtual levels taking part in the nonlinear mixing are resonantly enhanced because they overlap with real energy

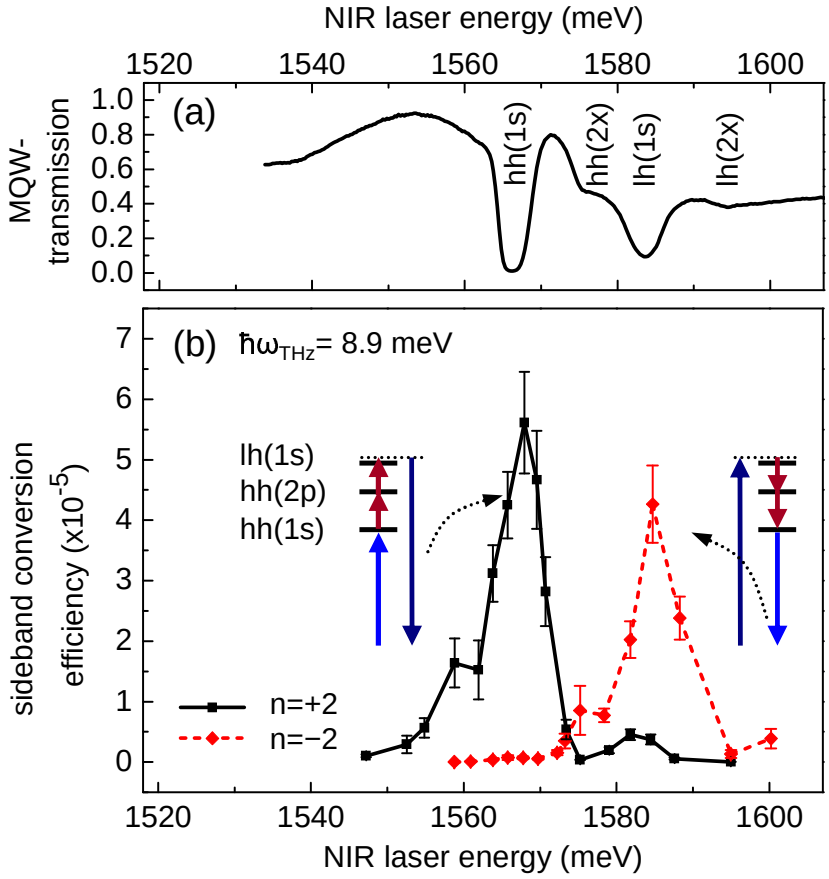

Figure 5.10.: (a) Multi quantum well film transmission spectrum from Fig. 5.2 (b) Sideband spectra for n=+2 (black line) and n=−2 (red dashed line) for an NIR peak intensity of 180 kW/cm^2, an FEL peak intensity around 18 kW/cm^2 and an FEL energy of 8.9 meV, corresponding to the intraexcitonic hh(1s-2p) transition. Energy level diagrams illustrate the involved transitions.

levels which have large transition matrix elements. This results in an efficient n=−2 generation as well. It is now of equal strength compared to the n=+2 signal, despite the fact that the emitted sideband can now be absorbed by the heavy-hole 1s exciton transition.

The additional small shoulders at 1575 meV (for n=−2) and at 1559 meV (for n=+2) cannot be assigned with absolute certainty to a particular resonance. For the n=+2 sideband such a mixing process would include a parity forbidden hh(1s-2s) intermediate transition in order to end up at the NIR optically allowed hh(2s) final transition. Likewise, for the n=−2 mixing the first transition involves the hh(2s) state from where a forbidden hh(1s-2s) intermediate transition would be necessary. Those processes could become possible by assuming a hybridized state in the strong THz field consisting of mixed hh(2s) and hh(2p) contributions and thus relaxing the selection rules. Furthermore, the final hh(2p) state could become NIR optically allowed. Other forbidden intraband transitions have been observed [169] and appeared also in electric fields [170, 171].

They were attributed to valence band mixing of the heavy- and light-hole bands [172]. In Fig. 5.11 the measured normalized n=+2 resonance scans are given for a THz energy at the hh(1s-2p) transition and different THz peak intensities. With increasing THz intensity we observe a broadening of the resonance at the hh(1s) exciton which is probably due to saturation, as has been observed for the overall peak height at the hh(1s) resonance before in Fig. 5.8(a). There we have seen that at an FEL peak intensity of ≈ 90 kW/cm^2 the signal was lower by a factor of 2.9 compared to what is expected from an quadratic increase extrapolated from low FEL peak intensities. We have attributed this deviation to a beginning Autler-Townes splitting that might bring the levels out of resonance. Here (Fig. 5.11) we observe the saturation at the hh(1s) resonance in the normalized power dependent scans, whereas the lh(1s) resonance at 1583 meV for 90 kW/cm^2 has not saturated yet, but has increased as expected by a factor of 3 when comparing it with the low THz peak intensity measurement (8 kW/cm^2). Note that the error bars for the peak uncertainty of $\pm 15\%$ have been omitted in the figure for clarity. Within this uncertainty it is not clear whether the additional peak at 1562 meV for 90 kW/cm^2 is real. Probably, it does not directly show an Autler-Townes split peak, since the splitting measured later on in chapter 6 at a comparable FEL peak intensity is much smaller with only 2.5 meV.

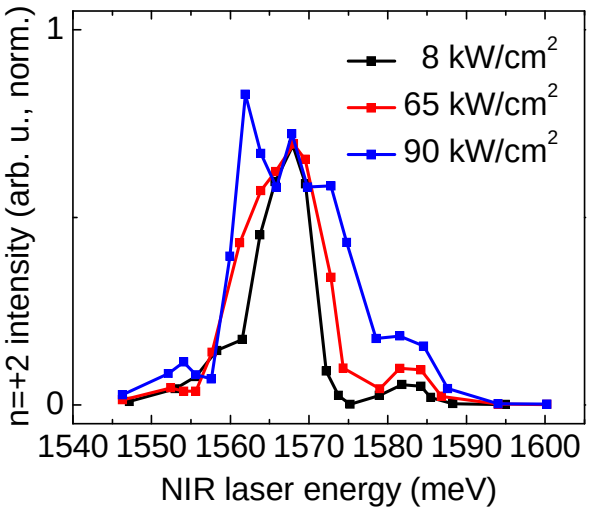

Figure 5.11.: Normalized n=+2 resonance spectra for different FEL peak intensities at an FEL photon energy of $\hbar\omega_{\mathrm{THz}} = 8.9$ meV. With increasing intensity we observe a saturation at the hh(1s) exciton at ≈ 1567 meV.

Room temperature resonance scan

At a temperature of 77 K there is no drop in the THz sideband conversion efficiency compared to the low-temperature measurement. At room temperature (RT) of 290 K the transmission spectrum changes significantly as can be seen in Fig. 5.12(a). The solid line represents the RT measurement while the dotted line gives again the low temperature transmission from Fig. 5.2 for comparison. The latter one has been shifted by 94 meV to lower energies due to the temperature dependent GaAs bandgap. The RT transmission shows much broader linewidths and a reduced absorption at the heavy-hole and light-hole excitons. Furthermore, higher excitonic states like the hh(2s) and lh(2s) states cannot be distinguished any more due to a significant broadening. Additionally, the hh-lh splitting decreases with increasing temperature from 17 meV to 14

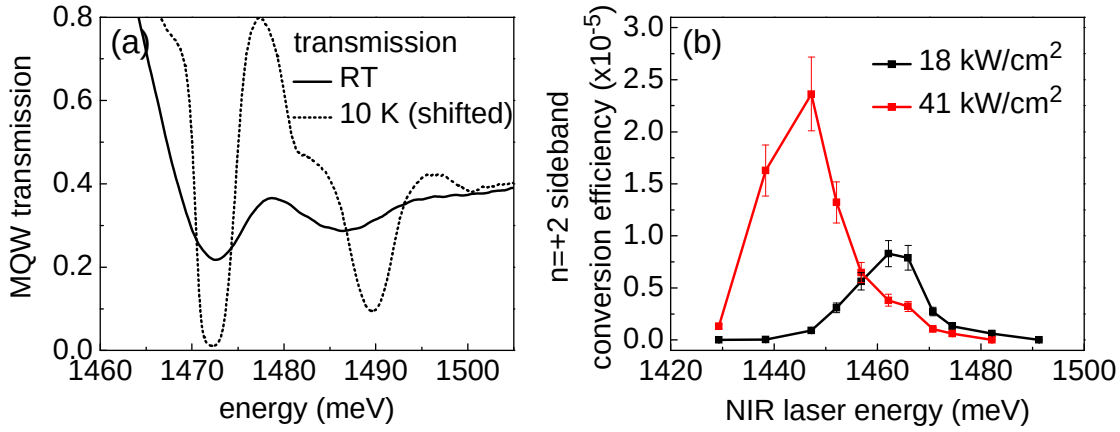

Figure 5.12.: (a) Sample transmission at room temperature (RT, solid line) and for comparison again at 10 K shifted by 94 meV to lower energy (dotted line, from Fig. 5.2). (b) n=+2 sideband resonance taken above room temperature for an NIR intensity of 180 kW/cm^2, an FEL intensity of 18 kW/cm^2 (black line) and 41 kW/cm^2 (red line). The FEL energy is fixed at 8.9 meV. Due to pronounced lattice heating, the sideband spectra appear shifted to lower energies.

meV because of a temperature dependent effective mass and barrier height [173].
Figure 5.12(b) depicts the n=+2 sideband resonance scan for a THz intensity of 18 kW/cm^2 (black line) and 41 kW/cm^2 (red line). The FEL photon energy is kept at the low-temperature intraexcitonic hh(1s-2p) transition at 8.9 meV, though the hh-lh splitting has decreased. However, with the broader absorption lines, the need for matching the THz energy exactly with the energy levels is relaxed. The sideband resonance scan does not show fine structures like in the low-temperature case, but more or less one broad line. The broadening stems from broader excitonic resonances in the transmission spectrum. Nevertheless, at a lower THz intensity of 18 kW/cm^2 we still find an efficiency which is only reduced by a factor of 7 compared to the 10 K measurement. Note that both spectra differ in the spectral position from the transmission measurement taken at 290 K. To overlap them with the transmission measurement, they have to be shifted to higher energies by 7 meV and 24 meV, respectively. This shift in bandgap is due to a pronounced FEL-induced lattice heating by roughly 17 K and 52 K for 18 kW/cm^2 and 41 kW/cm^2, respectively. Those values are obtained by calculating the temperature dependent GaAs bandgap shift via $E_{gap} = (1.519 - 5.405 \cdot 10^{-4} \times T^2/(T + 204))$ eV [163]. The enhanced lattice heating is also the reason why we could not go to higher FEL intensities without damaging the sample.

5.5. Summary and outlook

In summary, we have demonstrated efficient $n=\pm 2$ sideband generation in a symmetric GaAs/AlGaAs multiple quantum well film. We have employed a relatively simple geometry with the THz beam under normal incidence. Thus, we could couple effectively to inter- and intraexcitonic transitions between heavy- and light-hole states without using complicated dielectric waveguide geometries for effective THz coupling [131]. At a temperature of 10 K relatively high conversion efficiencies of the 1.7 μm thin quantum well film above 0.1% were measured despite somewhat broad linewidths. By tuning the THz energy in resonance with the hh($1s$-$2p$) transition we showed that this intraexcitonic transition dominates the sideband spectra through resonance enhancement. Choosing the THz energy to be resonant with the interexcitonic transition between hh and lh states results in a one order of magnitude lower conversion efficiency. Slightly above room temperature the sideband efficiency dropped only by a factor of 7 with respect to low temperatures for low THz powers.
The investigated structure could find application in optical modulators. For this purpose a voltage controlled switching of the sideband process would be favorable which can be achieved by shifting the sample's exciton transitions via the quantum-confined Stark effect [132] by an applied bias [133].

6. Autler-Townes splitting

This chapter deals with another fundamental effect induced by intense THz fields from the free-electron laser. We report an FEL-induced splitting of the energetically lowest heavy-hole 1s excitonic absorption line in the multiple quantum well investigated in the preceding chapters. This effect is monitored in the near-infrared transmission of a broadband laser while the FEL wavelength is tuned around the intraexcitonic heavy-hole 1s-2p transition. We discuss the FEL intensity- and wavelength-dependent splitting and show that it can be described qualitatively as an *ac* or *optical Stark effect* or an *Autler-Townes splitting* where the 1s and 2p states get "dressed" by the THz field. Our measurements also show some evidence of the dynamical Franz-Keldysh effect.
After a brief literature overview we introduce a simple theoretical model for the optical (ac) Stark effect that is the basis for the subsequent discussion.

6.1. Introduction

Intense electric fields alter the optical properties of quantum well heterostructures. We first take a look at these effects in the presence of static electric fields.
For dc fields in growth direction the well-known *quantum-confined Stark effect* (QCSE) [132, 174, 175] is most important. It leads to a tilting of the quantum well confinement potential which separates the electron and hole envelope wave functions spatially on opposite sides of the quantum well. As a result the exciton absorption is red-shifted and broadened for fields of the order of 50 kV/cm. Electroabsorption modulators with NIR light modulation up to 50 GHz [176] are based on this effect.
In-plane dc electric fields accelerate free carriers and lead to the so-called *Franz-Keldysh effect* [177, 178] that is also observed in bulk semiconductors. Tunneling of carriers into the bandgap results in absorption below the bandgap and oscillations in the absorption above the gap. However, in reference [175] this effect was very small and most pronounced was a broadening and finally a destruction of the exciton resonances for fields of the order of 10 kV/cm due to field ionization of the excitons.
For ac electric fields polarized in the quantum well plane the *dynamic Franz-Keldysh effect* (DFKE) [179–181] gives rise to a blueshift of the band edge and an exponential absorption tail below the bandgap. It occurs in a regime where the time-averaged kinetic energy (i.e. the ponderomotive energy) of an electron in the ac field of field strength E

and frequency ω becomes comparable to the photon energy[1]: $U_p = e^2E^2/(4m^*\omega^2) \approx \hbar\omega$ (effective mass m^*). The blueshift in the bandgap is equal to the ponderomotive energy, since the carriers in the band structure of the semiconductor gain this additional energy in the ac field. Small photon energies, i.e. in the MIR or THz range, are favorable to observe the DFKE. This effect has been studied by Nordstrom *et al.* in 1998 [96] in the *excitonic* absorption of InGaAs multiple quantum wells under normal incident THz radiation tuned near the 1*s*-2*p* excitonic transition. In bulk GaAs and ZnSe under intense (10^9 W/cm^2) mid-infrared illumination the DKFE could be seen more clearly by Chin *et al.* in 2000 [97] and Kono *et al.* in 2004 [165].
Intense ac electric fields also cause the *ac* or *optical Stark effect*. In analogy to the ac Stark effect for medium light intensity in atoms [182], it causes a shift (quadratic in the field strength) of the levels in a two-level system: when the light frequency ω is larger than the resonance frequency ω_{21} between the levels, the levels are attracted and for smaller light frequencies $\omega < \omega_{21}$ they are repelled. Such shifts have been observed in the linear absorption of quantum wells for intense NIR illumination [183] and intersubband resonant CO_2 laser irradiation [184]. Together with the DFKE it was investigated by Nordstrom and coworkers [96] for in-plane polarized THz radiation tuned to the intraexcitonic 1*s*-2*p* transition in InGaAs quantum wells.
When the light is resonant with the transition energy the optical Stark effect couples the involved states and alters their energy, i.e. the states get "dressed" by the light-matter interaction. Dressed states have been investigated extensively in atomic spectroscopy since the 1950s where the so-called *Autler-Townes splitting* [22] has been observed. Here, a molecular system probed by microwaves showed a splitting of the microwave absorption line when resonantly pumped with a strong radio-frequency field. In three-level systems this also leads to electromagnetically induced transparency (EIT) which has been investigated in GaAs quantum wells [185, 186]: A coupling field induced quantum interference between the dressed states is responsible for an absorption change with respect to the resonance of the undriven system. In a similar scheme also gain without inversion has been studied in quantum wells [187].
Despite some theoretical work [140, 142, 188, 189] it took a long time until the first observation of an Autler-Townes splitting in a quantum well structure, since the magnitude of the effect is rather small compared to the linewidths of the transitions. However, in 2004 Carter *et al.* [190, 191] were able to observe a splitting of a hole intersubband transition (interexcitonic transition) using near-infrared linear absorption. Their system consists of InGaAs quantum wells where a splitting of the first heavy-hole (hh) subband occurred when it is coupled by intense THz radiation to the second hh subband. Also in electronic intersubband transitions of modulation-doped InGaAs wells an ac Stark splitting could be seen directly in the THz region by Dynes *et al.* in 2005 [95]. Hereafter, such a splitting was also observed in zero-dimensional semiconductor quantum dots for near-infrared pump and probe light [192–194].
Dressed states induced by a strong THz field resonant to the intraexcitonic hh(1*s*-2*p*)

[1] The necessary field strength for this regime depends on the photon energy. For NIR light with $\hbar\omega = 1.55$ eV ($\widehat{=}$ 800 nm $\widehat{=}$ 375 THz) a field strength of $E = 36$ MV/cm is needed. For a frequency of $\nu = 1$ THz a field strength of $E = 5$ kV/cm is sufficient.

transition have been reported by Jameson and coworkers only recently in 2009 [195]. They concentrated on the dephasing time of the heavy-hole $2p$ state. However, the experimental evidence of an Autler-Townes splitting was rather weak.
In our work we pursue a similar approach. Nevertheless, we will present clear evidence of a splitting whose dependence on the FEL wavelength and power turns out to be well described by the following model.

6.2. Theoretical model

Already a simple model of a two-level atom interacting with an oscillating light field can provide a valuable basis for the discussion of the optical Stark effect. Hence, we consider a single hydrogen-like atom with two levels $1, 2$ of energy $\hbar\omega_2 > \hbar\omega_1$. The following standard treatment is based on reference [121, ch. 2] (see also [28, sec. 5.5]). The time-dependent Schrödinger equation including the light-matter coupling according to Eq. (2.13) (page 9) reads

$$i\hbar\frac{\partial\psi(\mathbf{r},t)}{\partial t} = [\hat{H}_0 - \hat{\mu}\cdot\tilde{E}(t)]\psi(\mathbf{r},t). \tag{6.1}$$

As before, $\hat{H}_0$ denotes the unperturbed Hamiltonian, $\hat{\mu} = -e\hat{z}$ is the dipole moment operator, $-e$ is the electronic charge and $\tilde{E}(t)$ is the z-polarized electric field.
We expand the time-dependent wave function into the eigenfunctions $\psi_m(\mathbf{r})$ of the unperturbed stationary Schrödinger equation:

$$\psi(\mathbf{r},t) = \sum_{m=1,2} a_m(t)e^{-i\omega_m t}\psi_m(\mathbf{r}). \tag{6.2}$$

$\hbar\omega_m$ are the stationary eigenstate energies. Inserting Eq. (6.2) into Eq. (6.1), multiplying by $\psi_n^*(\mathbf{r},t)$ from the left and integrating over space yields

$$i\hbar\frac{da_n}{dt} = -\tilde{E}(t)\sum_{m=1,2} e^{-i\omega_{mn}t}\mu_{nm}a_m. \tag{6.3}$$

$\mu_{nm} = \langle\psi_n|\hat{\mu}|\psi_m\rangle = \int\psi_n^*(\mathbf{r})\hat{\mu}\psi_m(\mathbf{r})d^3r$ is the dipole matrix element, and $\omega_{mn} = \omega_m - \omega_n$.
For the two-level atom in a monochromatic field of the form $\tilde{E}(t) = \frac{1}{2}E(\omega)[\exp(-i\omega t) + c.c.]$ we finally end up with two coupled differential equations:

$$i\hbar\frac{da_1(t)}{dt} = -\tilde{E}(t)e^{-i\omega_{21}t}\mu_{12}a_2 = -\mu_{12}\frac{E(\omega)}{2}\left[e^{-i(\omega+\omega_{21})t} + e^{i(\omega-\omega_{21})t}\right]a_2 \tag{6.4}$$

$$i\hbar\frac{da_2(t)}{dt} = -\tilde{E}(t)e^{-i\omega_{12}t}\mu_{21}a_1 = -\mu_{21}\frac{E(\omega)}{2}\left[e^{-i(\omega-\omega_{21})t} + e^{i(\omega+\omega_{21})t}\right]a_1. \tag{6.5}$$

In the *rotating wave approximation* (RWA) we neglect the rapidly oscillating terms $\exp[-i(\omega+\omega_{21})t]$ and $\exp[i(\omega+\omega_{21})t]$, since we are interested only in the light-induced

changes around the resonance $\omega \approx \omega_{21}$.
We consider a finite detuning $\Delta = \omega - \omega_{21}$ from the resonance case so that Eqs. (6.4) and (6.5) read

$$\frac{da_1(t)}{dt} = i\frac{\mu_{12}E(\omega)}{2\hbar}e^{i\Delta t}a_2 \tag{6.6}$$

$$\frac{da_2(t)}{dt} = i\frac{\mu_{21}E(\omega)}{2\hbar}e^{-i\Delta t}a_1. \tag{6.7}$$

Taking the time derivative of Eq. (6.6) and replacing all expressions with a_2 by a_1, one obtains the single differential equation

$$\frac{d^2a_1}{dt^2} = i\Delta\frac{da_1}{dt} - \frac{\Omega^2 a_1}{4}, \tag{6.8}$$

where $\Omega = |\mu_{21}E(\omega)|/\hbar$ is the *Rabi frequency*.
A solution can be found in the form of

$$a_1(t) = a_1(0)e^{i\Omega' t} \tag{6.9}$$

$$a_2(t) = a_2(0)e^{-i\Omega' t} \tag{6.10}$$

with $\Omega' = \frac{\Delta}{2} \pm \frac{1}{2}\sqrt{\Delta^2 + \Omega^2}$. The initial conditions are determined by $a_1(0)$ and $a_2(0)$. Inserting the solution back into the wave function (6.2) yields:

$$\psi(\mathbf{r},t) = a_1(0)e^{-i(\omega_1 - \frac{\Delta}{2} \pm \frac{1}{2}\sqrt{\Delta^2+\Omega^2})t}\psi_1(\mathbf{r}) + a_2(0)e^{-i(\omega_2 + \frac{\Delta}{2} \pm \frac{1}{2}\sqrt{\Delta^2+\Omega^2})t}\psi_2(\mathbf{r}). \tag{6.11}$$

Obviously, the former energy levels are split and shifted by the strong applied electric field, resulting in new "dressed" states with the energies:

$$\hbar\omega_1' = \hbar\left[\omega_1 - \frac{\Delta}{2} \pm \frac{1}{2}\sqrt{\Delta^2+\Omega^2}\right] \tag{6.12}$$

$$\hbar\omega_2' = \hbar\left[\omega_2 + \frac{\Delta}{2} \pm \frac{1}{2}\sqrt{\Delta^2+\Omega^2}\right]. \tag{6.13}$$

We explain the consequences of these results on the basis of our experimental system. The hh($1s$) and hh($2p$) excitonic states in our multiple quantum well sample constitute our artificial "two-level atom". We probe the hh($1s$) absorption via weak broadband NIR light during intense THz illumination in order to investigate the splitting of this line (more experimental details in the next section). In Fig. 6.1(a) the two involved excitonic energy levels are sketched. Note that only the hh($1s$) state is NIR optically active, while the hh($2p$) state is NIR optically "dark". But as already demonstrated in the sideband generation measurement in the preceding chapter, THz radiation couples very effectively to the heavy-hole $1s$-$2p$ transition (frequency ω_{21}). When intense THz fields are applied with the resonant frequency $\omega_{\mathrm{THz}} = \omega_{21}$ both $1s$ and $2p$ levels split symmetrically into two states of energy $\hbar\omega_{1(2)} \pm \hbar\Omega/2$, as illustrated in Fig. 6.1(a). This splitting of the initial single $1s$ absorption line into two lines is probed via broadband NIR laser pulses. The level separation is completely given by the Rabi frequency

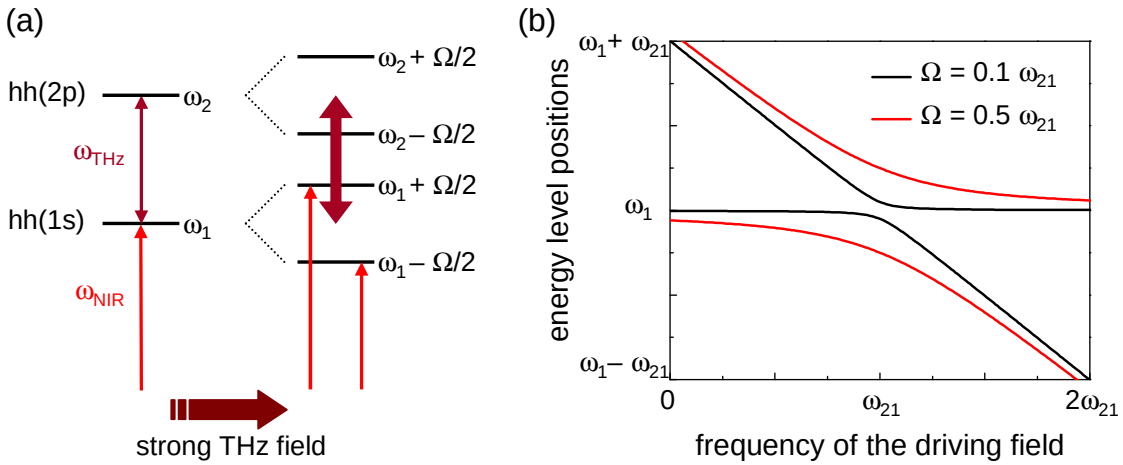

Figure 6.1.: (a) Realization of an optical Stark splitting on the basis of the involved excitonic energy levels in our experimental approach. Under strong THz irradiation at the intraexcitonic hh(1s-2p) resonance ($\omega_{\mathrm{THz}} = \omega_{21}$) each level splits in two levels separated by the Rabi energy $\hbar\Omega$. Only the lowest hh(1s) state is probed via NIR light while the hh(2p) state is NIR optically forbidden. (b) Calculation (from Eq. (6.12)) of the positions of the dressed states evolving from the unperturbed state ω_1 as a function of the FEL photon frequency ω_{THz} for two different Rabi frequencies Ω. At the resonance $\omega_{\mathrm{THz}} = \omega_{21}$ the initial level splits symmetrically.

$\Omega \propto E_{\mathrm{THz}}$, i.e. it is linear in the applied THz field strength. Intense THz fields are mandatory to observe such a splitting, and additionally, the linewidths should be small in order to distinguish the two split lines.
In Fig. 6.1(b) the calculated positions of the dressed states evolving from the lowest initial level ω_1 are plotted as a function of the THz light frequency. This calculation is based on Eq. (6.12), where the Rabi frequency is chosen with respect to the resonance frequency ω_{21} as $\Omega = 0.1\omega_{21}$ (black line) and $\Omega = 0.5\omega_{21}$ (red line), respectively. In both cases we observe a clear *anticrossing* of the dressed states when increasing the THz frequency from zero to $2\omega_{21}$. At the resonance $\omega_{\mathrm{THz}} = \omega_{21}$ the splitting is smallest, but symmetric with respect to the position of the initial level. As mentioned before, close to the resonance the splitting increases with the Rabi frequency, i.e. the THz field strength. Far away from the resonance the dressed states approach the unperturbed states. Thereby, the largest oscillator strength is related to the NIR transition that is closest to the undriven excitonic transition at the energy $\hbar\omega_1$. Hence, for coupling-frequencies below resonance ($\omega_{\mathrm{THz}} < \omega_{21}$) this dressed state lies energetically below the initial undriven state, i.e. the levels that are coupled (here the hh(1s) and hh(2p) states) are repelled. For $\omega_{\mathrm{THz}} > \omega_{21}$ they are attracted (*optical Stark shift*, observed for instance in [96]).
The physical origin of the splitting in our two-level atomic system can be understood in a picture based on the composite atom-field eigenstates [27, ch. 22]. We consider the case where the THz light frequency ω_{THz} is close to the resonance ω_{21} between the two states $|1\rangle$ and $|2\rangle$ (hh(1s) and hh(2p) state, respectively, in Fig. 6.1(a)). Without light-matter interaction the composite atom-field eigenstate $|1, N\hbar\omega_{\mathrm{THz}}\rangle$ is nearly degenerate

with $|2,(N-1)\hbar\omega_{\mathrm{THz}}\rangle$ and $|1,(N+1)\hbar\omega_{\mathrm{THz}}\rangle$ is nearly degenerate with $|2,N\hbar\omega_{\mathrm{THz}}\rangle$, where N is the number of photons of the light field in the mode ω_{THz}. With interaction the degeneracy between the states is lifted. They are shifted and separated in energy by $\hbar\Omega$ according to our previous calculation. The dressed states that result from the interaction between the two-level system and the intense, nearly-resonant THz field are a linear combination of the initially degenerate states that are weighted detuning-dependent (see [27, ch. 22.3] for more details).
Note that our treatment of the two-level system does not include damping phenomena, since we are only interested in the energy level positions and not in the temporal dynamics [28, sec. 5.5]. The density matrix formalism can include relaxation processes for populations and coherences (see [27, sec. 22.2] or [28, p. 224]), resulting in the so-called *Optical Bloch Equations* [28, sec. 5.4]. We have also neglected other energy levels apart from the two considered states where the coupling to the radiation field is expected to be strongest. We did not include the ground state from which we probe the system since it is energetically far away and hence does not couple to the strong THz field. Those additional levels could have been incorporated in a density matrix formalism. This has not been done here since the atomic-like system would still be too simplistic to realistically describe the present experiment. A careful treatment would be based on the *Semiconductor Bloch Equations* like in the references [119, 188, 195].

6.3. Experimental realization and results

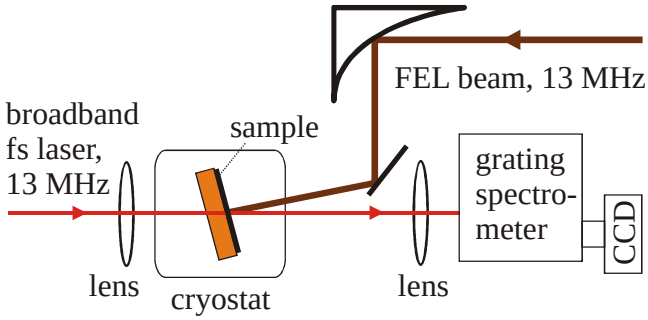

Figure 6.2.: Setup for Autler-Townes splitting. A broadband NIR laser reduced to a repetition rate of 13 MHz, probes the NIR absorption of the etched GaAs/AlGaAs sample while the hh($1s$) state is dressed by intense FEL radiation (see Fig. 6.1(a)). The transmitted light is analyzed by a spectrometer and a CCD camera.

As briefly described above we look at the hh($1s$) exciton line to study its splitting that is induced by intense THz radiation tuned to the intraexcitonic hh($1s$-$2p$) transition. We investigate the same etched GaAs/AlGaAs multiple quantum well sample on the ZnTe substrate as in the chapter before, where we have considered sideband generation. A schematic layout of the setup is displayed in Fig. 6.2. Since we employ the same setup as for sideband generation with minor differences, we refer the reader to section 5.2 on page 63 for a more detailed description of the sample and the setup. While sideband generation required a narrowband ps NIR laser, a broadband fs NIR laser is now used to probe the sample's transmission around the hh($1s$) exciton. As broadband laser we employ the 12 fs

Ti:sapphire laser introduced on page 19. Its 78 MHz repetition rate is actively synchronized to the 13 MHz FEL repetition rate via a feedback loop (*Femtolasers: Femtolock*) controlling the position of the oscillator output coupler. A pulse picker for the NIR laser reduces its repetition rate to 13 MHz to match the FEL repetition rate. The NIR probe light is attenuated to a peak intensity below 100 W/cm^2 in order not to modify the sample's absorption spectrum. It is then focused on the sample with a spot size of roughly 60 μm. Note that the pulse length at the quantum well sample is estimated to be of the order of 300 fs after transmission through some meters of air, several lenses and the pulse picker SiO_2 crystal. The NIR laser is transmitted through the sample at an angle of $\approx 15^\circ$ to the sample's surface normal and focused on the entrance slit of the spectrometer. A CCD camera attached to the spectrometer detects the dispersed light. The FEL beam is focused down onto the sample near normal incidence via an off-axis parabolic mirror of 17.8 cm focal length. The sample is kept in a cryostat as before at a temperature of approximately 10 K.

The CCD camera detects a transmission spectrum which changes under FEL illumination when NIR and FEL pulses overlap in time. A background image is subtracted with the NIR laser being blocked. The transmission is then normalized by the transmission without sample and the baseline is scaled to a common baseline for all spectra such that the resulting spectra look quite similar to the one of Fig. 5.2 on page 66. From that the absorption is calculated as the negative logarithm of the transmission and presented hereafter. Note that the baseline in different spectra is influenced differently by Fabry-Perot oscillations within the sample, therefore the baselines do not overlap completely. Also note that the strain in the etched quantum well film causes a shift of the heavy-hole and especially the light-hole exciton absorption lines, as described before in section 5.2. To compensate this shift of up to 1 meV for the hh($1s$) resonance, the spectra are horizontally displaced accordingly in order to overlap them with respect to the NIR energy. We believe that this does not modify our results, since only the relative separation between the levels that we probe is important and should be kept constant. Nevertheless, it was not possible to investigate always the same small spot on the multiple quantum well film and, as noticed before, subsequent cool down and heating of the sample from measurement day to measurement day probably changes the strain distribution in the etched film that is glued to the ZnTe substrate. Hence, in the spectra presented hereafter the lh($1s$) position varies up to 0.8 meV at a lh($1s$) linewidth of ≈ 4 meV (FWHM). Again, we think that this 5% variation with respect to the hh($1s$)-lh($1s$) separation does not change the interpretation of our results significantly.

Directly after having recorded an image where NIR and FEL pulses overlap in time, the NIR laser pulse is delayed by 300 ps to probe the sample after the FEL pulse has passed through it. An image recorded at this temporal delay serves as reference from which we determine the FEL-induced lattice heating by comparing the spectral position of the hh($1s$) absorption peak with its position without FEL illumination. The temperature dependent bandgap shift is then compensated by a horizontal displacement. Consequently, any shifts in the absorption lines hereafter are not related to a lattice heating. We like to emphasize that only at the highest THz peak intensities the

sample temperature increases to 25 K (corresponding to a bandgap redshift of $\approx$ 1.3 meV), whereas it is below 15 K in most of the data presented here.
The determination of the THz peak intensities requires the knowledge of the precise FEL spot size and pulse length. The pulse length is extracted from a cross-correlation measurement between the FEL pump and the NIR probe pulses where the Autler-Townes splitting itself is used as the signal parameter. An example is given later on. The FEL spot sizes are measured with a razor blade that is moved in the focus perpendicular to the FEL beam while the transmitted power is detected. One obtains the spatial beam profile by differentiating the obtained function between transmitted power and position of the blade. For an FEL wavelength of 140 μm ($\widehat{=}$ 8.8 meV) for instance a spot diameter of 1.2 mm is deduced[2].

Experimental results

Figure 6.3 presents an overview over the measured absorption spectra for different FEL wavelengths and peak intensities at the temporal overlap between FEL and NIR pulses. We briefly describe the main features before we concentrate on specific details.
The FEL photon energies are chosen in the range from $\hbar\omega_{\mathrm{THz}} = 6.1$ meV (panel (a)) to $\hbar\omega_{\mathrm{THz}} = 14$ meV (panel (d)). Hence, this range covers the estimated intraexcitonic hh($1s$-$2p$) transition energy of $\approx$ 9 meV (see Fig. 5.3). In Fig. 6.3(a) the absorption is shown for an FEL photon energy of $\hbar\omega_{\mathrm{THz}} = 6.1$ meV, below the $1s$-$2p$ transition, which is displayed schematically in the inset. The black curve is the reference without FEL illumination. The observed spectral peaks are assigned again to the respective excitonic transitions (see Fig. 5.2 on page 66). The colored curves below represent the spectra taken at different THz peak intensities which are written above the respective curve in the same color (values are given in kW/cm^2). All spectra are shifted vertically for clarity. At the same FEL photon energy the relative peak intensities are accurate within 5-10%, since only the THz average power is changed. However, when switching between FEL wavelengths the FEL pulse structure changes either by adjacent water vapor absorption lines, reflections in the optics or a possible standing wave pattern in the 500 μm thin ZnTe substrate onto which the sample is glued. Additionally, the powermeter might show a different response. We estimate the absolute THz peak intensity to be accurate within 30%.
In the region from 1570 to 1575 meV one clearly observes a small additional peak that appears at THz peak intensities of $\approx$ 90 kW/cm^2 energetically above the hh($1s$) exciton. This peak moves away from the hh($1s$) resonance with increasing THz peak intensity. Additionally, this peak appears to shift the hh($2s$) shoulder (denoted with hh($2x$)) to higher energies which reminds us of an anticrossing-like behavior indicating a mixing between the additional peak and the hh($2s$) and continuum levels. At higher

[2] This value is 20% smaller than the value that has been extracted directly from the sideband signal in the chapter before (see page 73). This difference could be explained when assuming that the sideband measurement has not been performed directly in the focus. This does not change the former results, since the spot size directly at the sample is important and enters in the peak power.

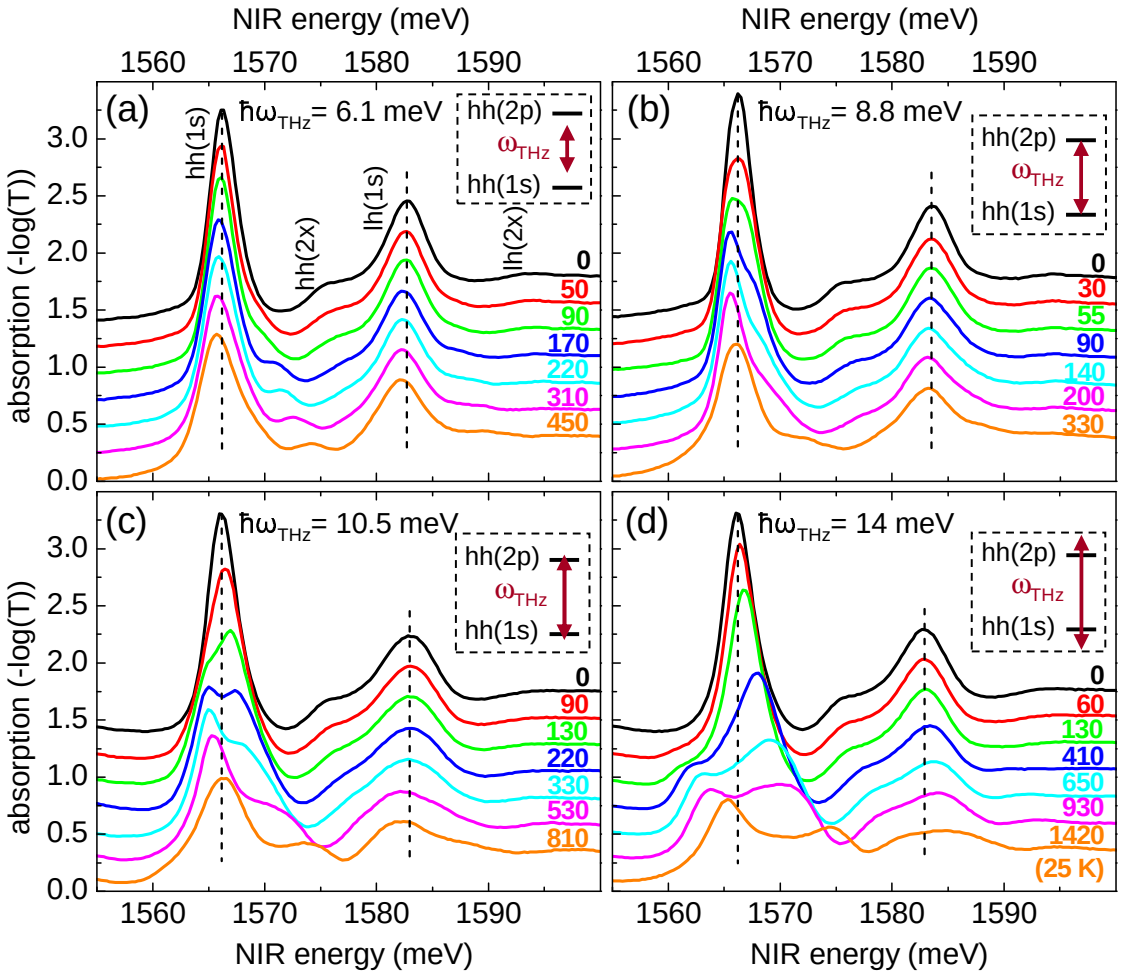

Figure 6.3.: Near-infrared sample absorption at 10 K under FEL illumination for different FEL photon energies of $\hbar\omega_{\mathrm{THz}} = 6.1$ meV (a), 8.8 meV (b), 10.5 meV (c) and 14 meV (d), around the expected hh($1s$-$2p$) resonance at ≈ 9 meV. In panel (a) the observed NIR resonances without FEL illumination (black line) are assigned to the hh($1s$), hh($2x$), lh($1s$) and lh($2x$) states (x denotes the s and p states). All curves are shifted for clarity and each color corresponds to a certain FEL peak intensity (given on the right side in kW/cm^2). The inset of each graph illustrates the detuning of $\hbar\omega_{\mathrm{THz}}$ from the expected resonance between the two levels hh($1s$) and hh($2p$). As most remarkable feature one clearly notices a splitting of the hh($1s$) absorption line depending on the FEL peak intensity and photon energy. The vertical dashed black lines mark the undriven hh($1s$) and lh($1s$) exciton positions. Note that all curves have been corrected for an FEL-induced lattice heating. In panel (d) it is responsible for an increased temperature of 25 K for a peak intensity of 1420 kW/cm^2 (18 K for 930 kW/cm^2), whereas in all remaining curves in (a)-(d) the temperature is below 15 K.

THz peak intensities the $2s$ absorption vanishes. Also the lh($1s$) line seems to develop an additional high-energy peak in the energy range of 1585-1590 meV, while its $2s$ absorption gets less pronounced. As can be seen by the vertical dashed black lines, the hh($1s$) and lh($1s$) peaks move slightly to lower energies for higher THz peak intensities. We like to repeat that a spectral shift of the curves is not due to FEL-induced lattice heating, that has been accounted for in a reference measurement, and which has been corrected for in the curves. A line broadening at higher THz peak intensities, as well as the vanishing of the hh($2s$) exciton shoulder could be explained by a beginning field-ionization of the excitons. This shortens the exciton lifetime and leads to broader absorption lines, as has been observed for strong in-plane dc electric fields before [175].
When illuminating the sample with FEL light tuned close to the intraexcitonic resonance, as depicted in Fig. 6.3(b), a hh($1s$) splitting in two lines of nearly equal height can be seen vaguely in a broadening of the $1s$ resonance at 55 kW/cm^2 with a following more distinct line separation at 90 kW/cm^2. Overall this indication of an Autler-Townes splitting seems to have a smaller line separation than in panel (a) before at comparable peak intensites.
Slightly above the resonance (see Fig. 6.3(c)) we notice a peak below the hh($1s$) exciton absorption at higher FEL peak intensities. It appears at 1565 meV with a nearly constant height while the main hh($1s$) resonance peak is shifted with THz power. The splitting between both peaks is again smaller than before at comparable peak intensities. But at 220 kW/cm^2 it is symmetric around the initial $1s$ resonance. At the highest THz peak intensity the main peak lies again at the initial hh($1s$) exciton, whereas the additional peak is found 8 meV above. At the lh($1s$) position we notice a similar splitting, but much weaker. Note that the $1s$-$2p$ resonance linewidth deduced before from Fig. 5.3 (page 68) is ≈ 3 meV. Hence, the photon energy in panel (c) is still very close to this intraexcitonic $1s$-$2p$ resonance (≈ 9 meV).
Above resonance as plotted in Fig. 6.3(d) we now observe a small peak growing at around 1562 meV *below* the hh($1s$) exciton line, whereas a similar peak grew on the high-energy side in panel (a) for a THz photon energy below the intraexcitonic resonance. For increasing THz intensities the peak at 1562 meV grows and shifts towards the initial position of the hh($1s$) line while this line is broadened and shifted to 1575 meV for the highest FEL peak intensity. Additionally, the light-hole $1s$ exciton moves to larger energies instead of smaller ones like in panel (a). Again, we notice a small peak above the lh($1s$) resonance that moves from 1590 meV at 410 kW/cm^2 to higher NIR energies and shifts the lh($2s$) shoulder. Note that higher THz peak intensities are employed than in the other graphs of this figure, i.e. the additional peak below the hh($1s$) exciton line is small here at comparable intensities.
In the following section we concentrate on the splitting of the hh($1s$) exciton line that we assign to an Autler-Townes splitting. We compare it with the theoretical model derived in the previous section. Although we also observe a very weak splitting of the broad lh($1s$) exciton line, we do not comment on that since the effects are rather small compared to the splitting at the heavy-hole exciton.

6.4. Discussion

Anticrossing behavior

In order to gain some insight into the splitting we fit the experimental hh($1s$) absorption line with two lines. The fit function we use is neither a Lorentzian nor a Gaussian, since the measured hh($1s$) line shape is somewhat asymmetric because of higher excitonic states on the high-frequency side. The basis of our phenomenological fit function is a Voigt profile. The original Voigt profile describes a line broadened by two different types of mechanisms. One type leads to a Gaussian distribution, the other one to a Lorentzian distribution. The Voigt profile is then a convolution of a Gaussian with a Lorentzian line. It is often approximated by a pseudo-Voigt function, i.e. a linear combination of a Gaussian and a Lorentzian line function. In addition, we need two of these pseudo-Voigt profiles separated by 1 meV[3] since the measured absorption line is asymmetric with respect to a vertical line through its center (compare for instance the black line in Fig. 6.3(a)). However, when fitting the peaks measured under different FEL illumination, we do not change the relative separation between the two constituent profiles that make up our "custom-made" pseudo-Voigt line. Also the ratio of their height and the ratio of their widths is kept constant and only adjusted for both peaks together.
In Fig. 6.4 we summarize the measured hh($1s$) absorption peaks (black solid line) for different FEL photon energies at a common FEL peak intensity of $\approx$ 130 kW/cm^2. While the black dashed line denotes the reference taken with the FEL pulses 300 ps before the temporal overlap with the NIR probe pulses, the red line represents a fit that is the sum of two pseudo-Voigt profiles given as blue and green curves.
In panel (a) of this figure we are energetically above the intraexcitonic resonance energy of $\approx$ 9 meV. We notice the additional small peak (green line) energetically below the undriven exciton absorption (black dashed line), and the main peak fitted by the blue line lies above it. Approaching the resonance with a THz photon energy of 10.5 meV (b) the small green peak has grown and moved towards the reference, whereas the main peak has decreased. Both peaks are nearly of the same height. Closest to the resonance, at 8.8 meV in panel (c), the blue peak has already decreased to half of the height of the green peak that has grown. At lower THz photon energies (d) and (e) the blue peak decreases further and is driven away from the undriven exciton line, while the initially small green peak is now closest to the undriven hh($1s$) line. Note that for a photon energy of 6.1 meV (e) the peak is essentially at the same position as before for a photon energy of 7.6 meV (d). This could be explained by the slightly different THz peak intensities we look at.
In this picture we also notice that the state dressed by the THz field that is closest to the undriven absorption always has the largest absorption strength, whereas the peak is smallest when it is far away. When both peaks are centered symmetric around

[3] A monolayer fluctuation inside the GaAs wells is not responsible here since it would result in two peaks separated by 2 meV.

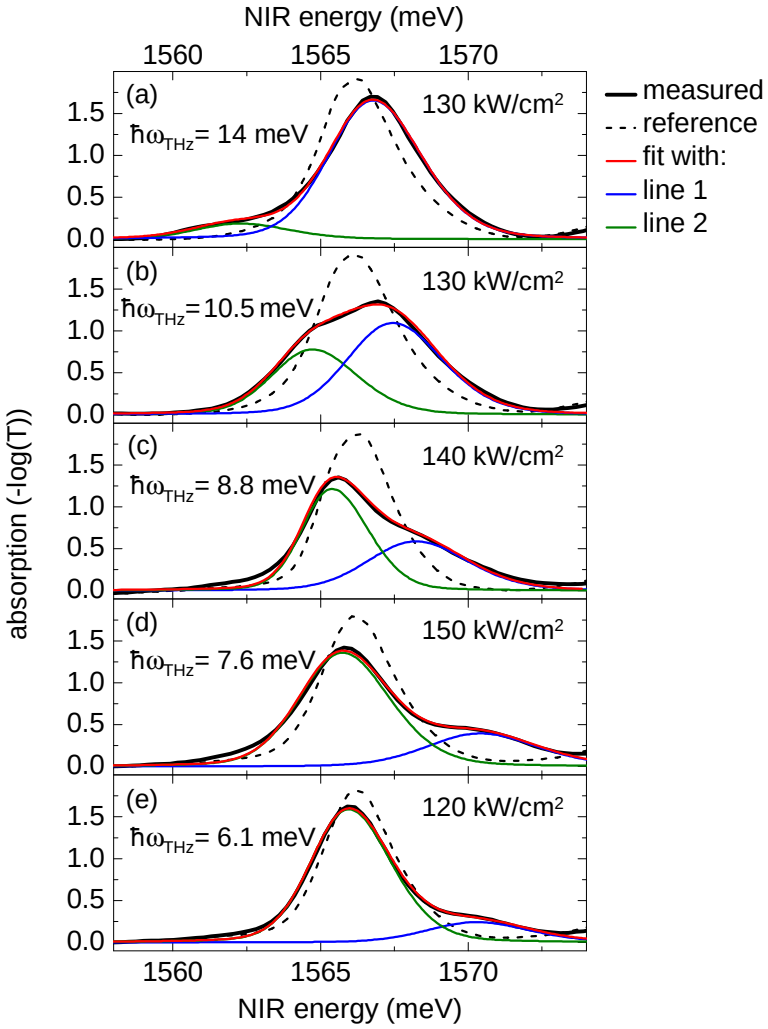

Figure 6.4.: Measured hh(1s) absorption spectra (black solid line) for different FEL photon energies as given in the graphs, and at an FEL peak intensity of ≈ 130 kW/cm^2. The black dashed line is a reference where the NIR pulses come 300 ps after the FEL pulses. The red line is a fit based on two peaks with a phenomenological line shape (shown as blue and green line, respectively). We clearly see an anticrossing behavior. With respect to a symmetric splitting the intraexcitonic resonance (≈ 9 meV) appears to be closer to 10.5 meV (b) than to 8.8 meV (c) for the FEL peak intensity used here.

the initial hh(1s) absorption, which should be the case at the intraexcitonic resonance, the absorption strength is shared equally between the two dressed states. Since the intraexcitonic resonance was found to lie at around 9 meV, we would expect a symmetric splitting in graph (c) that should be closest to the resonance. However, the symmetric splitting is rather fulfilled in graph (b) for a higher photon energy. This symmetric splitting is also maintained for a broad range of THz peak intensities (see Fig. 6.3(c)). On the other hand, when going to smaller THz peak intensities also the splitting for 8.8 meV becomes symmetric, which can be seen vaguely in the 55 kW/cm^2 curve of Fig. 6.3(b). This small discrepancy might be a first indication that further effects have

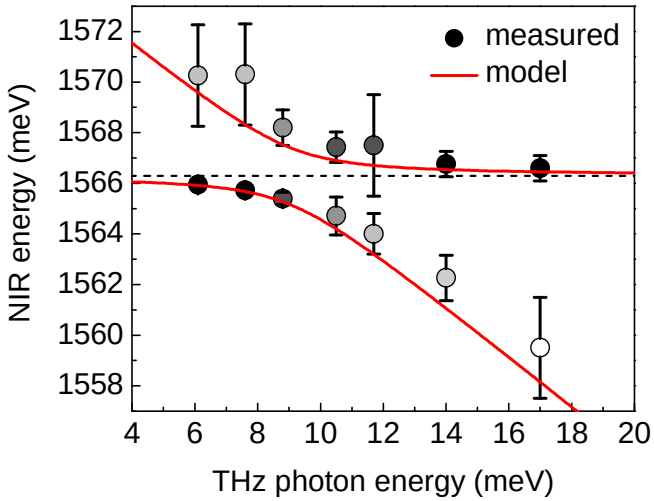

Figure 6.5.: Measured peak positions as a function of the THz photon energy for a THz peak intensity of ≈ 130 kW/cm^2. The peak positions are taken from the fits with pseudo-Voigt profiles. The error bars denote deviations from several measurements and the uncertainty in the THz peak intensity. The red lines represent the calculated level positions according to Eq. (6.12) (page 88) for a resonance energy of $\hbar\omega_{21} = 9$ meV and a Rabi frequency $\Omega = 0.25\omega_{21}$. The horizontal black dashed line marks the position of the undriven hh($1s$) exciton. The absorption strength for each data point is indicated on a grayscale. Note that the peak at 1560 meV for $\omega_{\mathrm{THz}} = 17$ meV is quite weak.

to be taken into account.
In Fig. 6.5 the measured peak positions are plotted for several THz photon energies at a common THz peak intensity of ≈ 130 kW/cm^2. The peak positions are obtained by fitting the absorption with two pseudo-Voigt functions. For each peak the absorption strength is presented on a grayscale, and it is largest for peaks close to the undriven exciton line (marked by the horizontal black dashed line). The red line is calculated from Eq. (6.12) (page 88) for a hh($1s$-$2p$) resonance energy of $\hbar\omega_{21} = 9$ meV and a Rabi frequency $\Omega = 0.25\omega_{21}$. As can be seen from the overall agreement, the measured splitting is described reasonably well with the simple formulas of a two-level atom in RWA-approximation, despite a Rabi frequency that is 25% of the resonance frequency of the system. However, there seems to be a small systematic deviation, since most data points lie energetically above the model curves. A better agreement could be obtained with a resonance energy of 10.2 meV which shifts the red curves to higher THz photon energies, but which does not agree well with our measured $1s$-$2p$ transition energy. Another effect that should also be present in our geometry with the in-plane polarized THz beam is the dynamical Franz-Keldysh effect (DKFE). It leads to a blueshift of the main absorption edge proportional to the squared THz electric field $\mathrm{E}^2_{\mathrm{THz}}$ and to $\omega^{-2}_{\mathrm{THz}}$ [96, 179]. At the THz peak intensity of 130 kW/cm^2 it does not seem to play a significant role, since it would mainly blueshift the peaks for the low THz photon energies (Fig. 6.5) due to its $\omega^{-2}_{\mathrm{THz}}$ dependency. But its influence can be seen more clearly at higher THz pump powers, as we will investigate in the next section.

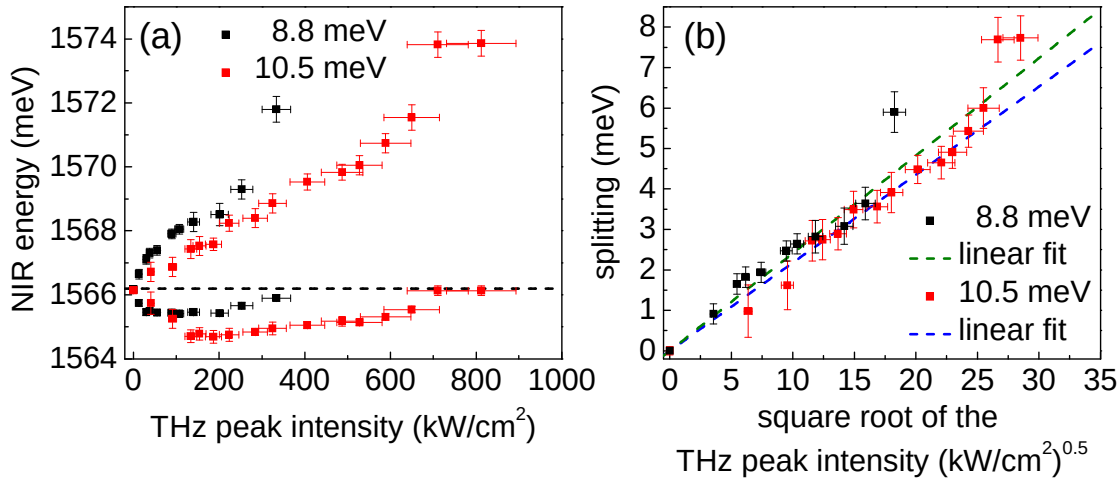

Figure 6.6.: (a) Positions of the Autler-Townes split lines evolving from the hh($1s$) exciton as a function of the THz peak intensity for an FEL photon energy of 8.8 meV (black dots) and 10.5 meV (red dots) around the intraexcitonic hh($1s$-$2p$) resonance ($\approx$ 9 meV). The positions are obtained by a fit with two pseudo-Voigt functions. The vertical error bars are related to the error in the fit, the horizontal ones to the uncertainty in the FEL peak intensity. The black dashed horizontal marks the undriven exciton line. (b) Extracted splitting, i.e. the distance between the two peaks from (a), as a function of the square root of the THz peak intensity for 8.8 meV (black dots) and 10.5 meV (red dots). Both data sets can be fitted linearly, which is expected for an Autler-Townes splitting on the resonance.

Dependence on the THz peak intensity

Now we evaluate the splitting around the intraexcitonic resonance with respect to the THz peak intensity. In Fig. 6.6(a) the positions of the split lines are plotted that evolve from the initial hh($1s$) exciton as a function of the THz peak intensity for the near-resonant FEL photon energies of 8.8 meV (black dots) and 10.5 meV (red dots). The horizontal dashed line denotes the undriven exciton position. The vertical error bars are related to the uncertainty in the spectral position of the peaks when fitting the absorption with the phenomenological Voigt line shape explained before. The horizontal error bars are the 10% uncertainty in the FEL peak intensity.
The Autler-Townes splitting is symmetric around the initial undriven exciton position only for small FEL peak intensities. For an FEL photon energy of 10.5 meV the range of a symmetric splitting is larger than for 8.8 meV. For both photon energies the energetically lower peak starts to move back to higher NIR energies above a THz peak intensity of around 200 kW/cm^2. This blueshift appears to go linearly with the THz peak intensity as expected from the DFKE [96]. At a THz peak intensity of 330 kW/cm^2 for 8.8 meV and 710 kW/cm^2 for 10.5 meV, respectively, the high-energy peak is shifted faster than it can be explained via the DKFE. However, below these intensities we believe that we observe an interplay between the DKFE and the ac Stark effect. While the ac Stark effect leads to a splitting of the absorption line the DKFE shifts all absorption features uniformly to higher NIR energies. Hence, the absolute spectral

positions of the peaks are influenced by the DKFE, but the splitting as separation between the peaks should not be affected.
In Fig. 6.6(b) the separation between the two peak positions from panel (a) is plotted as a function of the square root of the FEL peak intensity, i.e. a parameter proportional to the electric field. First we notice that the splittings for both photon energies around the intraexcitonic resonance is quite similar. Since the $1s$-$2p$ transition is driven nearly resonantly[4], we expect a line separation that is given by the Rabi frequency, i.e. a splitting proportional to the THz field strength E_{THz} (compare Eq. (6.12) for negligible detunings $\Delta \approx 0$). The green dashed line is a linear fit of the measured splitting for 8.8 meV, where the last data point has been excluded. The same is done for 10.5 meV (blue dashed line), neglecting the last two data points. Apparently, the expected behavior for an Autler-Townes splitting is observed in both cases in nearly the same way. This is also consistent with the DKFE, since this effect should not alter the splitting, but shifts both split lines equally.
The single data point for 8.8 meV at 330 kW/cm^2 might be mistaken, since the behavior below that intensity is similar to that for a THz photon energy of 10.5 meV. However, the two data points at the highest THz peak intensity above 700 kW/cm^2 could mark the onset of another regime. Assuming an electric field to intensity relation of a plane wave $I = \frac{1}{2}\epsilon_0 c_0 n E^2$ with $n \approx 3.61$ [61] we can estimate a THz field strength in the sample (30% reflection) of $E_{\mathrm{THz}} \approx 10$ kV/cm. At these field strengths field-ionization of the excitons should start which results in a line broadening [175] that should affect the Autler-Townes splitting. Another important point is that the peak separation of roughly 8 meV is quite large. It corresponds to 90% of the initial resonance energy $\omega_{21} \approx 9$ meV. In addition, the Rabi energy, which was 25% of the resonance energy at a peak intensity of 130 kW/cm^2 before, should be $\hbar\Omega \approx 0.6\hbar\omega_{21} \approx 5.4$ meV. This is already a large part of the resonance energy and hence a region where the rotating wave approximation is not valid anymore.
Here, we like to give an estimation for the splitting close to the resonance, i.e. the Rabi energy, and compare it with our measurement. We evaluate the splitting at an FEL photon energy of $\hbar\omega_{\mathrm{THz}} = 10.5$ meV and at a peak intensity of 200 kW/cm^2 where it is symmetric around the undriven exciton line (see Fig. 6.6(a)) and where the peak separation is close to the linear fit of all data points in Fig. 6.6(b). The measured value for the peak separation or Rabi energy is $\hbar\Omega \approx 3$ meV. When assuming an electric field to intensity relation of a plane wave as above, we find $E_{\mathrm{THz}} \approx 5.4$ kV/cm. For evaluating the Rabi energy $\hbar\Omega = |\mu_{21} E_{\mathrm{THz}}|$ we also need to know the transition matrix element μ_{21}. Since the exciton as an electron-hole pair behaves like an hydrogen atom, we take the hydrogen $1s$-$2p$ transition matrix element $\mu_{21} = 0.745 \times e\, a_0^*$ [73, p. 197] and adjust its strength via the effective Bohr radius a_0^* in our excitonic system. The effective Bohr radius is defined via $a_0^* = m_e \epsilon a_0/\mu^*$ [122, p. 382] with the ordinary Bohr radius $a_0 = 0.529$ Å, the permittivity $\varepsilon \approx 13$ and the reduced mass $\mu^* = m^* m_h/(m^* + m_h)$ which is composed of the effective mass for electrons $m^* = 0.067 m_e$ and for the heavy-hole $m_h = 0.53 m_e$ [110, p. 70]. With these values we find an effective Bohr radius

[4] We are nearly resonant with both THz photon energies due to the large $1s$-$2p$ line broadening of ≈ 3 meV at the 9 meV intraexcitonic transition energy.

of $a_0^* \approx 116$ Å, a transition matrix element of $\mu_{21} \approx 86$ eÅ and hence a Rabi energy of 4.7 meV. However, the effective Bohr radius is larger than the quantum well width of 82 Å. Therefore, we expect the exciton wave function to be modified, resulting in an ellipsoidal charge distribution and a smaller Rabi energy. In reference [195] the hh($1s$) splitting was also investigated for a THz beam tuned to the $1s$-$2p$ resonance in a quantum well consisting of 12 nm wide GaAs wells with 16 nm wide $Al_{0.3}Ga_{0.7}As$. For a THz field amplitude of ≈ 5 kV/cm they observed a vague splitting of ≈ 2.5 meV, from which a transition matrix element of 50 eÅ can be calculated. Though their quantum well width is larger by almost 50% compared to our system, their matrix element μ_{21} and their effective Bohr radius is smaller by a factor of 1.7. Using their calculated value $\mu_{21} = 50$ eÅ we find a Rabi energy of 2.7 meV, which is in very good agreement with our measurement.
Thus, on one hand our measured Rabi energy of 3 meV (at $E_{\mathrm{THz}} \approx 5.4$ kV/cm) is 36% smaller than a rough estimation of 4.7 meV where an effective Bohr radius a_0^* enters that is too large compared to the actual well width of $0.71a_0^*$. On the other hand the comparison with a value from the literature in a similar system with a larger well width gives a Rabi energy that is 10% smaller than the measured one and lies within the estimated 30% uncertainty in determining the FEL peak intensity ($\approx$ 15% field error). Hence, we also find a good quantitative agreement in our experiment.

Temporal behavior of the Autler-Townes splitting

Finally, we shift the time delay between the NIR probe pulses and the strong THz pulses and look at the absorption spectra, as depicted in Fig. 6.7(a). Here, the recorded spectra for a nearly resonant THz photon energy of 10.5 meV and a THz peak intensity of 500 kW/cm^2 are shown for different time delays with an offset in vertical and horizontal direction. First, the NIR pulses are delayed by -32 ps, i.e. they probe the sample *before* the FEL pulse arrives. After uniform delay steps of ≈ 2.7 ps the absorption is probed again and hence the NIR pulse is swept over the FEL pulse. Note that the dotted curves denote absorption spectra that have been interpolated between adjacent spectra in order to present the data continuously with respect to the time delay. In panel (b) of the figure a contour plot of the data in (a) is displayed in a slightly larger time range. The positions of the respective exciton levels are indicated above the plot. White lines next to the time delay axis mark interpolated spectra, and in the rainbow color scale high absorption is dark red, low absorption is black. From both plots we find that the FEL laser pulse modifies the absorption spectrum significantly via the Autler-Townes effect on a time scale of a few tens of picoseconds. Both the hh($1s$) and lh($1s$) absorption are drastically reduced and recover instantaneously after the FEL pulse has passed. In the contour plot we also clearly see that one of the dressed states stays at the former hh($1s$) exciton line while the other one is pushed away to higher NIR energies. The same can be seen for the lh($1s$) exciton, but much weaker. During the FEL pulse we also notice a small sub-bandgap absorption. This absorption tail can be attributed to the dynamical Franz-Keldysh effect which obviously also follows the

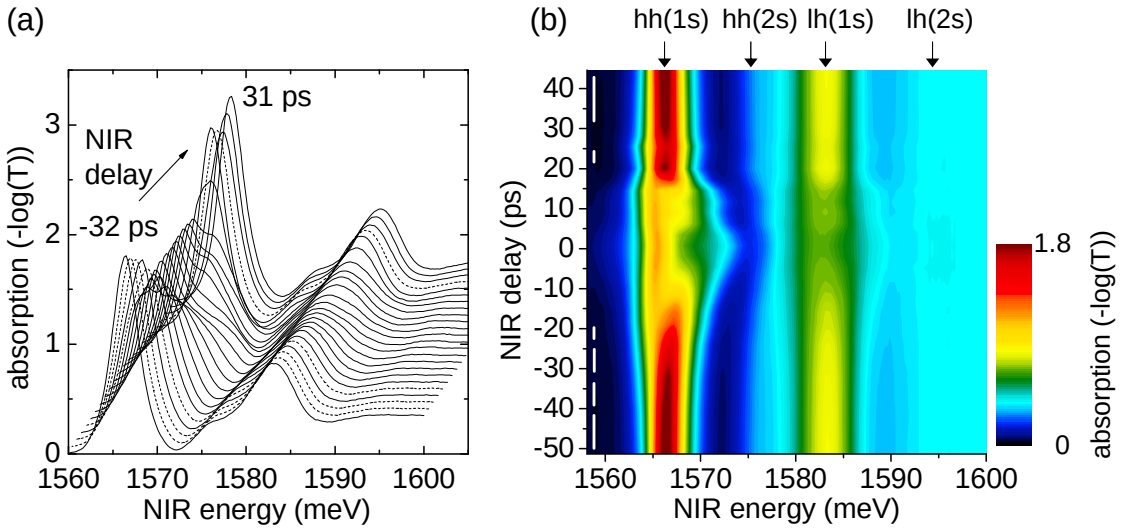

Figure 6.7.: (a) Measured absorption for different time delays between the NIR pulses and the FEL pulses at an FEL photon energy of 10.5 meV and a peak intensity of 500 kW/cm^2. The traces are equally spaced in time with a separation of $\approx$ 2.7 ps, starting at -32 ps (NIR pulses come before FEL pulses). They are offset both in vertical and horizontal direction for clarity. Note that several traces had to be linearly interpolated from the adjacent traces (marked as dashed lines). (b) Contour plot of (a) for a larger time range in a rainbow color scale with dark red (black) areas denoting high (low) absorption. On the left side white vertical lines next to the time axis mark traces that are linearly interpolated from adjacent traces. The excitonic levels are marked above the plot. We find a splitting of the hh($1s$) absorption only during the FEL pulse which is nicely seen in panel (b) in a $\approx$ 30 ps broad region around zero time delay. The FEL pulse also induces a slight sub bandgap absorption (probably due to the DKFE), a dissociation of the hh($2s$) exciton and a broadening of the lh($1s$) absorption.

FEL pulse instantaneously.
From the obtained spectra with respect to different NIR time delays we can deduce the FEL pulse structure by comparing the measured Autler-Townes splitting for every time delay step with a splitting that has been recorded for a certain THz average power at the temporal overlap. Hence, we can assign a certain FEL average power to every NIR time delay. Finally, we get an FEL pulse intensity envelope as shown in Fig. 6.8 with this (tedious) sampling method. The pulse is somehow distorted which might be due to a reflection of the FEL pulse on the rear side of the ZnTe sample substrate. From this FEL pulse envelope we find a pulse width of $\approx$ 27 ps (FWHM). The FEL spectrum presented in the inset is quite symmetric with a width of 0.75 μm (FWHM). From this spectral width we can deduce a Fourier-limited FEL pulse width of 27 ps when assuming a Gaussian FEL pulse shape with a time-bandwidth product of 0.441. This lower limit for the pulse width is in nice agreement with the measured value.

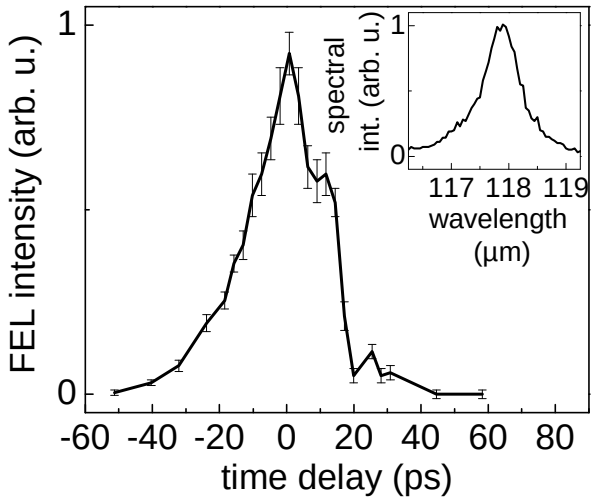

Figure 6.8.: FEL pulse intensity envelope for a THz photon energy of 10.5 meV and a peak intensity of 500 kW/cm^2. It has been sampled by assigning an FEL average power to the Autler-Townes splitting at a certain time delay between the NIR and FEL pulses (see Fig. 6.7). Error bars give the uncertainty in assigning the splitting to a certain average power. From the FEL spectrum (see inset) a Fourier pulse limit of 27 ps (FWHM) is deduced, which agrees with the FWHM of the measured pulse envelope.

6.5. Summary

In summary, we have observed an Autler-Townes splitting of the hh(1s) exciton probed in the NIR transmission of a GaAs/AlGaAs multiple quantum well when exposed to intense, in-plane polarized THz radiation. Compared to previous work, this is the first clear observation of such a splitting that is induced by THz radiation resonant to the intraexcitonic hh(1s-2p) transition. It starts for THz peak intensities of 50-100 kW/cm^2 which corresponds to THz field strengths of 3-4 kV/cm. We measure a clear anticrossing of the coupled levels, i.e. the dressed states, as a function of the FEL photon energy. Near the intraexcitonic resonance the separation between the two split peaks reveals a linear dependence with respect to the THz field amplitude, as predicted by a simple two-level model. Deviations from this behavior start when the Rabi frequency is 60% of the resonance frequency. It is surprising that the adjacent absorption features of the lh(1s) state or the hh(2s) state do not disturb the separation between the two dressed states. The only effect that appears to mix with the Autler-Townes splitting is the dynamical Franz-Keldysh effect that initiates a blueshift of all absorption features and hence does not interfere much with the actual splitting of the coupled levels. We have concentrated on the splitting of the hh(1s) exciton absorption line, although a similar, but much weaker effect could be observed partly at the lh(1s) exciton.
Finally, we could demonstrate that the splitting occurs on a picosecond timescale when we shifted the time delay between the NIR probe pulses and the intense THz pulses. Thereby, a principal application could be the modulation of light at very high frequencies.

A. Interband and intersubband optical selection rules

In this section we deduce the selection rules for optical transitions in a *symmetric* GaAs/AlGaAs quantum well, following reference [24, sec. 1.II], [122, sec. 17.1] and [196, ch. VII]. In analogy to chapter 2.1 we assume that the carrier wave function in a single quantum well grown in z-direction can be written as $\Psi_{\nu,n}(\mathbf{r}) = u_\nu(\mathbf{r}) f_n(\mathbf{r})$ with a lattice periodic Bloch function $u_\nu(\mathbf{r})$ and a slowly varying envelope function $f_n(\mathbf{r})$ (*envelope function approximation*). Here, ν and n are the band and subband indices, respectively.
According to *Fermi's Golden Rule* the transition rate W_{if} for an optical transition between an initial state i of energy E_i and a final state f of energy $E_f > E_i$ is given by

$$W_{if} = \frac{2\pi}{\hbar} |\langle \Psi_i | V | \Psi_f \rangle|^2 \delta(E_f - E_i - \hbar\omega). \tag{A.1}$$

$\hbar\omega$ is the photon energy. $V = \frac{1}{2m^*}(\mathbf{p} + e\mathbf{A})^2 \approx \frac{e}{m^*}\mathbf{p}\cdot\mathbf{A}$ is the light-matter interaction Hamiltonian for an electron of charge $-e$. We have neglected the nonlinear term $\mathbf{A}^2$ in the vector potential and used the Coulomb gauge $\nabla\cdot\mathbf{A} = 0$ so that $\mathbf{A}$ commutes with $\mathbf{p}$. In the *dipole approximation* where the wavelength is much larger than any structural parameter, $\mathbf{A}(t) = \mathbf{e}A_0\sin(\omega t)$ varies like the electric field $\mathbf{E}$ due to the relation $\mathbf{E}(t) = -\frac{\partial}{\partial t}\mathbf{A}(\mathbf{t})$. $\mathbf{e}$ is the polarization direction of the electric field. Inserting V back in Eq. (A.1) the transition rate is determined by the following transition matrix elements

$$\langle \Psi_i | \mathbf{e}\cdot\mathbf{p} | \Psi_f \rangle = \overbrace{\langle u_\nu | \mathbf{e}\cdot\mathbf{p} | u_{\nu'} \rangle}^{(a)} \overbrace{\langle f_n | f_{n'} \rangle}^{(b)} + \overbrace{\langle u_\nu | u_{\nu'} \rangle}^{(c)} \overbrace{\langle f_n | \mathbf{e}\cdot\mathbf{p} | f_{n'} \rangle}^{(d)}, \tag{A.2}$$

where the indices ν (n) and ν' (n') denote the initial and final band (subband), respectively. The selection rules for the *interband transitions* can be deduced from terms (a) and (b), since (a) is only nonzero when $\nu \neq \nu'$.
We first evaluate the terms (c) and (d). Term (c), $\langle u_\nu | u_{\nu'} \rangle = \delta_{\nu\nu'}$, does not vanish when transitions in the same band ν occur, for example in the conduction band. Hence, term (d) controls the strength of those *intersubband transitions*. We express the envelope wave function that is normalized to the sample area S as $f_{n\mathbf{k}_\perp} = \frac{1}{\sqrt{S}}\exp[i(k_x x + k_y y)]\phi_n(z)$. Thereby we find for term (d) [196, p. 243]:

$$\begin{aligned} \left\langle f_{n\mathbf{k}_\perp} | \mathbf{e}\cdot\mathbf{p} | f_{n'\mathbf{k}'_\perp} \right\rangle &= \frac{1}{S}\int \mathrm{e}^{-\mathrm{i}\mathbf{k}_\perp\mathbf{r}_\perp}\phi_n^*(z)[e_x p_x + e_y p_y + e_z p_z]\phi_{n'}(z)\mathrm{e}^{\mathrm{i}\mathbf{k}'_\perp\mathbf{r}_\perp}\, d\mathbf{r} \\ &= (e_x\hbar k_x + e_y\hbar k_y)\delta_{nn'}\delta_{\mathbf{k}_\perp\mathbf{k}'_\perp} + e_z \langle \phi_n | p_z | \phi_{n'} \rangle \delta_{\mathbf{k}_\perp\mathbf{k}'_\perp}. \end{aligned} \tag{A.3}$$

The first term accounts for *intrasubband* transitions within the same subband n at a constant $\mathbf{k}_\perp$-position where the initial and final states coincide, i.e. $\omega = 0$ [196, p. 243]. These transitions are the analogue of the free-carrier absorption and require phonons or defects for momentum conservation.
The second term requires z-polarized light to induce an intersubband transition at a constant wavevector $\mathbf{k}_\perp$. In a *symmetric* quantum well the midplane is a symmetry plane and therefore $\langle\phi_n|p_z|\phi_{n'}\rangle$ is nonzero when the *intersubband selection rule*

$$n - n' = \text{odd integer} \tag{A.4}$$

is fulfilled. In *asymmetric* quantum wells also transitions are allowed with $n - n' =$ even integer.

For the interband transition rules between the valence and the conduction band we evaluate term (a) in Eq. (A.2). Typical III-V semiconductors like GaAs have conduction bands with s-like symmetry and valence bands with p-like symmetry. Interband matrix elements of the form $\langle x|p_x|s\rangle = \langle y|p_y|s\rangle = \langle z|p_z|s\rangle$ are nonzero [122, p. 410]. Hence, interband transitions can be excited by light polarized in growth direction or in the quantum well plane.
The overlap integral of term (b) from Eq. (A.2) reads

$$\left\langle f_{n\mathbf{k}_\perp} | f_{n'\mathbf{k}'_\perp} \right\rangle = \langle\phi_n|\phi_{n'}\rangle\, \delta_{\mathbf{k}_\perp \mathbf{k}'_\perp}\,. \tag{A.5}$$

In *symmetric* type-I[1] quantum wells of finite depth the resulting *interband selection rule* for electron-hole transitions allows only transitions at a constant $\mathbf{k}_\perp$ wavevector for which

$$n - n' = \text{even integer}. \tag{A.6}$$

For rectangular wells of infinite depth the selection rule is intensified to $n = n'$, but usually these transitions are also strongest in finitely deep rectangular GaAs/AlGaAs wells [196, p. 250]. In *asymmetric* wells also transitions are allowed for which $n - n' =$ odd integer.

[1] In type-I heterostructures like GaAs/AlGaAs quantum wells the electrons and holes are confined to the same material layer, i.e. to GaAs in this case. In type-II quantum wells like InP/$In_{0.52}Al_{0.48}As$ the electrons and holes are spatially separated.

B. Derivation of the total THz absorption

A derivation is given for the total THz absorption of a multi quantum well probed by broadband THz pulses after photoexcitation (we follow closely [115]). The corresponding experiment is described in chapter 4 where the the two THz fields, namely differential THz transmission $\Delta E(t) = E_{\text{with pump}}(t) - E_{\text{without pump}}(t)$ and the reference without optical excitation $E_{\text{ref}}(t) = E_{\text{without pump}}(t)$ are measured simoultaneously. We consider a single quantum well that is anti-reflection coated. Hence, propagation effects within the actual wedged waveguide sample with two internal passes through the active layers are neglected, as well as reflections at the sample boundaries. Therefore, the reference field $E_{\text{ref}}(t)$ is identical with the incident THz field.
The transmitted electric THz field through an infinitely narrow quantum well film can be derived from Maxwell's equations [117]:

$$E_{\text{T}}(t) = E_{\text{with pump}}(t) = E_{\text{ref}}(t) - \mu_0 \frac{c}{2n} \frac{\partial P(t)}{\partial t}, \tag{B.1}$$

where $P(t)$ is the macroscopic intersubband THz polarization in the quantum well and n is the background refractive index. We have assumed a lossless medium when the excitation is not present ($P_{\text{without pump}} = 0$).
Hence, the measured differential transmission $\Delta E(t) = E_{\text{with pump}}(t) - E_{\text{ref}}(t)$ is given in Fourier space by

$$\Delta E(\omega) = \mu_0 \frac{c}{2n} \mathrm{i}\omega P(\omega). \tag{B.2}$$

We are interested in the linear THz response where the polarization is related to the electric field via the susceptibility χ:

$$P(\omega) = \varepsilon_0 \chi(\omega) E_{\text{ref}}(\omega). \tag{B.3}$$

Inserting Eq. (B.3) in (B.2) leads to an expression for χ:

$$\chi(\omega) = -\frac{\mathrm{i}2nc}{\omega} \frac{\Delta E(\omega)}{E_{\text{ref}}(\omega)}. \tag{B.4}$$

Expressing the transmitted THz field with pump E_{T} and the reflected THz field E_{R} in Fourier frequency space yields [117]:

$$E_{\text{T}}(\omega) = E_{\text{ref}}(\omega) + \mathrm{i}\mu_0 \frac{c}{2n} \omega P(\omega) = E_{\text{ref}}(\omega) + \frac{\mathrm{i}\omega}{2nc} \chi(\omega) E_{\text{ref}}(\omega) \tag{B.5}$$

$$E_{\text{R}}(\omega) = \mathrm{i}\mu_0 \frac{c}{2n} \omega P(\omega) = \frac{\mathrm{i}\omega}{2nc} \chi(\omega) E_{\text{ref}}(\omega). \tag{B.6}$$

Using these expressions we obtain the transmission and reflection coefficients as

$$T(\omega) = \frac{E_{\mathrm{T}}(\omega)}{E_{\mathrm{ref}}(\omega)} = 1 + \frac{\mathrm{i}\omega}{2nc}\chi(\omega) \tag{B.7}$$

$$R(\omega) = \frac{E_{\mathrm{R}}(\omega)}{E_{\mathrm{ref}}(\omega)} = \frac{\mathrm{i}\omega}{2nc}\chi(\omega). \tag{B.8}$$

The absorbed intensity by the quantum well is given as the difference in the incident intensity and the reflected and transmitted intensities: $I_{\mathrm{abs}} = I_{\mathrm{ref}} - I_{\mathrm{T}} - I_{\mathrm{R}}$. Defining the total THz absorption α as fraction of the absorbed intensity compared to the incident = reference intensity and using Eqs. (B.7), (B.8) and (B.4) yields

$$\begin{aligned}\alpha(\omega) &= \frac{I_{\mathrm{abs}}(\omega)}{I_{\mathrm{ref}}(\omega)} = 1 - |T(\omega)|^2 - |R(\omega)|^2 = \frac{\omega}{nc}\mathrm{Im}[\chi(\omega)] - 2\left(\frac{\omega}{2nc}\right)^2 |\chi(\omega)|^2 \\ &= 2\mathrm{Im}\left[-\mathrm{i}\frac{\Delta E(\omega)}{E_{\mathrm{ref}}(\omega)}\right] - 2\left|\frac{\Delta E(\omega)}{E_{\mathrm{ref}}(\omega)}\right|^2 .\end{aligned} \tag{B.9}$$

In the approximation $|\Delta E| \ll |E_{\mathrm{ref}}|$ the second term is neglected and the total THz absorption $\alpha(\omega)$ consists only of the imaginary part of χ and reads

$$\alpha(\omega) \approx \frac{\omega}{nc}\mathrm{Im}[\chi(\omega)] = 2\mathrm{Im}\left[-\mathrm{i}\frac{\Delta E(\omega)}{E_{\mathrm{ref}}(\omega)}\right]. \tag{B.10}$$

This Eq. (4.4) is finally used to calculate the THz absorption in chapter 4.

C. Semiconductor Bloch Equations

We deduce the equations of motion for the intersubband polarization and the subband occupations within the conduction band of a quantum well structure. These equations are necessary to compute the response of our quantum well system when exposed to THz probe light after NIR photoexcitation. This derivation is done in close analogy to the one for the interband polarization that results in the so-called *Semiconductor Bloch Equations* [123], [121, p. 211].
The full Hamiltonian for a quantum well system that is exposed to optical and THz light is given by [115]:

$$\hat{H} = \overbrace{\sum_{\lambda,\mathbf{k}} \epsilon_{\lambda,\mathbf{k}} \hat{a}^\dagger_{\lambda,\mathbf{k}} \hat{a}_{\lambda,\mathbf{k}}}^{\substack{\text{kinetic energy} \\ \text{with band structure}}} + \overbrace{\frac{1}{2} \sum_{\substack{\lambda,\lambda', \\ \mathbf{k},\mathbf{k}',\mathbf{q}\neq\mathbf{0}}} V_q \hat{a}^\dagger_{\lambda,\mathbf{k}+\mathbf{q}} \hat{a}^\dagger_{\lambda',\mathbf{k}'-\mathbf{q}} \hat{a}_{\lambda',\mathbf{k}'} \hat{a}_{\lambda,\mathbf{k}}}^{\substack{\text{carrier}-\text{carrier} \\ \text{Coulomb interaction}}}$$
$$\underbrace{- E_{\text{opt}}(t) \sum_{\lambda,\lambda',\mathbf{k}} d_{\lambda,\lambda'}(\mathbf{k}) \hat{\mathbf{a}}^\dagger_{\lambda,\mathbf{k}} \hat{\mathbf{a}}_{\lambda',\mathbf{k}}}_{\substack{\text{coupling to optical field} \\ (\textbf{interband} \text{ transition})}} + \underbrace{A_{\text{THz}}(t) \sum_{\substack{\lambda,\mathbf{k}, \\ \mathbf{l},\mathbf{l}'}} j^\lambda_{l,l'} \hat{a}^\dagger_{\lambda,l,\mathbf{k}} \hat{a}_{\lambda,l',\mathbf{k}}}_{\substack{\text{coupling to THz field} \\ (\textbf{intersubband} \text{ transition})}} . \quad \text{(C.1)}$$

The first term describes the kinetic energy of the carriers in the band structure. At the valence band it reads $\epsilon_{v,\mathbf{k}} = \hbar^2 k^2/(2m_v)$, and at the lowest conduction band $\epsilon_{c,\mathbf{k}} = E_{\text{gap}} + \hbar^2 k^2/(2m_c)$. λ is the band index containing bulk band index, and, as long as a summation over l is not explicitly given (last term), subband index l. $\hat{a}^\dagger_{\lambda,\mathbf{k}}$ and $\hat{a}_{\lambda,\mathbf{k}}$ are the fermionic creation and annihilation operators, respectively, for an electron in band λ with momentum $\hbar\mathbf{k}$. The second sum stands for the carrier-carrier Coulomb interaction. $V_q = V^{\lambda,\lambda'}_{ll',\mathbf{q}}$ is the Coulomb matrix element in $\mathbf{k}$ space [121, p. 123] which reads with the envelope functions $\xi_\lambda(z)$ of the confined carrier wave functions [115]:

$$V^{\lambda,\lambda'}_{ll',\mathbf{q}} = \frac{e^2}{2\epsilon_0 \epsilon S q} \iint \mathrm{d}z\, \mathrm{d}z' \xi^*_{l,\lambda}(z) \xi^*_{l',\lambda'}(z') e^{-q|z-z'|} \xi_{l',\lambda'}(z') \xi_{l,\lambda}(z), \quad \text{(C.2)}$$

with the quantization area S, the permittivity ϵ_0 of free-space and the relative permittivity ϵ.
The first two terms of Eq. (C.1) make up the electron gas Hamiltonian, whereas the third and fourth term describe the light-matter interaction. The *interband* contribution is given by term three with its dipole matrix element d and the electric field $E(t)$. Its

form originates from the xE gauge. Coupling of the THz field to *intersubband* transitions is better described in the pA current gauge with the THz vector potential $A(t)$. This contribution is shown as the last term. j is the intersubband matrix element from Eq. (4.14) on page 52. Comparing this THz interaction Hamiltonian with the one from Eq. (4.11), we have dropped the A^2 part here. This part does contribute to the total energy, but it does not contribute to the equations of motion[1].
The temporal evolution of the expectation value of an arbitrary operator $\hat{O}$ is calculated via the commutator of $\hat{H}$ and $\hat{O}$ in the Heisenberg equation of motion:

$$\frac{\partial}{\partial t}\langle\hat{O}\rangle = \frac{i}{\hbar}\langle[\hat{O},\hat{H}]\rangle. \tag{C.3}$$

We are especially interested in the coupled equations of motion for the intersubband polarization $p^c_{1,2,\mathbf{k}} = \langle\hat{a}^\dagger_{c,1,\mathbf{k}}\hat{a}_{c,2,\mathbf{k}}\rangle$ and the occupation numbers for the two conduction subbands $n^c_{1,\mathbf{k}} = \langle\hat{a}^\dagger_{c,1,\mathbf{k}}\hat{a}_{c,1,\mathbf{k}}\rangle$ and $n^c_{2,\mathbf{k}} = \langle\hat{a}^\dagger_{c,2,\mathbf{k}}\hat{a}_{c,2,\mathbf{k}}\rangle$, respectively. To this end we have to calculate the commutator between those quantities and the Hamiltonian $\hat{H}$, where we make use of the anti-commutation rules for the Fermionic creation and annihilation operators ([121, p. 90]): $[\hat{a}_{\lambda,\mathbf{k}},\hat{a}^\dagger_{\lambda',\mathbf{k}'}]_+ = \hat{a}_{\lambda,\mathbf{k}}\hat{a}^\dagger_{\lambda',\mathbf{k}'} + \hat{a}^\dagger_{\lambda',\mathbf{k}'}\hat{a}_{\lambda,\mathbf{k}} = \delta_{\lambda,\lambda'}\delta_{\mathbf{k},\mathbf{k}'}$ and $[\hat{a}_{\lambda,\mathbf{k}},\hat{a}_{\lambda',\mathbf{k}'}]_+ = [\hat{a}^\dagger_{\lambda,\mathbf{k}},\hat{a}^\dagger_{\lambda',\mathbf{k}'}]_+ = 0$. Note that the commutator for the Coulomb interaction term contains four-operator expressions. Trying to solve those expressions in the equations of motion leads to an infinite hierarchy of equations [121, p. 131]. This well-known problem is avoided by splitting the four-operator terms into products of densities and polarizations plus the unfactorized rest. Thereby the equation of motion from Eq. (C.3) can be separated into the *Hartree-Fock* and the *scattering* contributions [123] and [121, p. 214]:

$$\frac{\partial}{\partial t}\langle\hat{O}\rangle = \frac{\partial}{\partial t}\langle\hat{O}\rangle_{\text{Hartree}-\text{Fock}} + \frac{\partial}{\partial t}\langle\hat{O}\rangle_{\text{scatt}}. \tag{C.4}$$

With this approximation, a lengthy, but straightforward calculation yields [115]:

$$\begin{aligned} i\hbar\frac{\partial}{\partial t}p^{vc}_{1,1,\mathbf{k}} &= (\tilde{\varepsilon}^c_{1,\mathbf{k}} + \tilde{\varepsilon}^v_{1,\mathbf{k}})\,p^{vc}_{1,1,\mathbf{k}} - (1 - n^c_{1,\mathbf{k}} - n^v_{1,\mathbf{k}})\hbar\tilde{\omega}^R_{1,1,\mathbf{k}} + (p^c_{1,2,\mathbf{k}})^*\hbar\tilde{\omega}^R_{1,2,\mathbf{k}} \\ &\quad + p^{vc}_{1,2,\mathbf{k}}\left((j^c_{2,1})^* A_{\text{THz}} - \sum_{\mathbf{q}\neq\mathbf{k}} V^{cc}_{12,\mathbf{k}-\mathbf{q}}(p^c_{1,2,\mathbf{q}})^*\right) + i\hbar\frac{\partial}{\partial t}p^{vc}_{1,1,\mathbf{k}}\bigg|_{\text{scatt}} \qquad \text{(C.5)} \\ i\hbar\frac{\partial}{\partial t}p^{vc}_{1,2,\mathbf{k}} &= (\tilde{\varepsilon}^c_{2,\mathbf{k}} + \tilde{\varepsilon}^v_{1,\mathbf{k}})\,p^{vc}_{1,2,\mathbf{k}} - (1 - n^c_{2,\mathbf{k}} - n^v_{1,\mathbf{k}})\hbar\tilde{\omega}^R_{1,2,\mathbf{k}} + p^c_{1,2,\mathbf{k}}\hbar\tilde{\omega}^R_{1,1,\mathbf{k}} \\ &\quad + p^{vc}_{1,1,\mathbf{k}}\left(j^c_{2,1}A_{\text{THz}} - \sum_{\mathbf{q}\neq\mathbf{k}} V^{cc}_{12,\mathbf{k}-\mathbf{q}}p^c_{1,2,\mathbf{q}}\right) + i\hbar\frac{\partial}{\partial t}p^{vc}_{1,2,\mathbf{k}}\bigg|_{\text{scatt}} \qquad \text{(C.6)} \end{aligned}$$

[1] This term commutes with the operators for the polarizations and occupations in the Heisenberg equation of motion [115].

$$
\begin{aligned}
i\hbar\frac{\partial}{\partial t}p^c_{1,2,\mathbf{k}} &= (\tilde{\varepsilon}^c_{2,\mathbf{k}} - \tilde{\varepsilon}^c_{1,\mathbf{k}})\, p^c_{1,2,\mathbf{k}} + p^{vc}_{1,2,\mathbf{k}}\hbar(\tilde{\omega}^R_{1,1,\mathbf{k}})^* - (p^{vc}_{1,1,\mathbf{k}})^*\hbar\tilde{\omega}^R_{1,2,\mathbf{k}} \\
&\quad + (n^c_{1,\mathbf{k}} - n^c_{2,\mathbf{k}})\left(j^c_{2,1}A_{\mathrm{THz}} - \sum_{\mathbf{q}\neq\mathbf{k}} V^{cc}_{12,\mathbf{k}-\mathbf{q}}p^c_{1,2,\mathbf{q}}\right) + i\hbar\frac{\partial}{\partial t}p^c_{1,2,\mathbf{k}}\bigg|_{\mathrm{scatt}} \qquad \text{(C.7)} \\
\hbar\frac{\partial}{\partial t}n^c_{1,\mathbf{k}} &= -2\mathrm{Im}\left[(p^{vc}_{1,1,\mathbf{k}})^*\hbar\tilde{\omega}^R_{1,1,\mathbf{k}} + (p^c_{1,2,\mathbf{k}})^*\left(j^c_{2,1}A_{\mathrm{THz}} - \sum_{\mathbf{q}\neq\mathbf{k}} V^{cc}_{12,\mathbf{k}-\mathbf{q}}p^c_{1,2,\mathbf{q}}\right)\right] \\
&\quad + \hbar\frac{\partial}{\partial t}n^c_{1,\mathbf{k}}\bigg|_{\mathrm{scatt}} \qquad \text{(C.8)} \\
\hbar\frac{\partial}{\partial t}n^c_{2,\mathbf{k}} &= -2\mathrm{Im}\left[(p^{vc}_{1,2,\mathbf{k}})^*\hbar\tilde{\omega}^R_{1,2,\mathbf{k}} + p^c_{1,2,\mathbf{k}}\left((j^c_{2,1})^*A_{\mathrm{THz}} - \sum_{\mathbf{q}\neq\mathbf{k}} V^{cc}_{12,\mathbf{k}-\mathbf{q}}(p^c_{1,2,\mathbf{q}})^*\right)\right] \\
&\quad + \hbar\frac{\partial}{\partial t}n^c_{2,\mathbf{k}}\bigg|_{\mathrm{scatt}} \qquad \text{(C.9)} \\
\hbar\frac{\partial}{\partial t}n^v_{1,\mathbf{k}} &= -2\mathrm{Im}\left[(p^{vc}_{1,1,\mathbf{k}})^*\hbar\tilde{\omega}^R_{1,1,\mathbf{k}} + (p^{vc}_{1,2,\mathbf{k}})^*\hbar\tilde{\omega}^R_{1,2,\mathbf{k}}\right] + \hbar\frac{\partial}{\partial t}n^v_{1,\mathbf{k}}\bigg|_{\mathrm{scatt}}. \qquad \text{(C.10)}
\end{aligned}
$$

In these *Semiconductor Bloch Equations* we have simplified the notation by introducing the generalized Rabi frequency $\tilde{\omega}^R_{l,l',\mathbf{k}} = \frac{1}{\hbar}[d^{c,v}_{l',l}E(t) + \sum_{\mathbf{q}\neq\mathbf{k}} V^{vc}_{l,l',|\mathbf{k}-\mathbf{q}|}p^{vc}_{l,l',\mathbf{q}}]$ and the renormalized single particle energies (see [121, p. 215])

$$\tilde{\varepsilon}^\lambda_{l,\mathbf{k}} = \epsilon^\lambda_{l,\mathbf{k}} - \sum_{\mathbf{q}} V^{\lambda,\lambda}_{l,l,|\mathbf{k}-\mathbf{q}|}n^\lambda_{l,\mathbf{q}}. \qquad \text{(C.11)}$$

The first two equations of motion, (C.5) and (C.6), describe the interband dynamics. In our case, we are interested in the THz response probed by a weak THz beam 25 ps after NIR photoexcitation. Then, the dynamics is fully governed by the intersubband polarization $p^c_{1,2,\mathbf{k}}$ in Eq. (C.7), while the interband polarizations have vanished. Since only the lowest conduction subband is populated by the NIR pump beam and since a THz induced change in the subband population is a second-order effect, we eliminate the population dynamics and identify the occupation number with the pump-pulse induced carrier distribution function, i.e. $n^c_{l,\mathbf{k}} = f^c_{l,\mathbf{k}}$. Finally, we end up with the simplified intersubband equation of motion:

$$
\begin{aligned}
i\hbar\frac{\partial}{\partial t}p^c_{1,2,\mathbf{k}} &= (\tilde{\varepsilon}^c_{2,\mathbf{k}} - \tilde{\varepsilon}^c_{1,\mathbf{k}})\, p^c_{1,2,\mathbf{k}} + (f^c_{1,\mathbf{k}} - f^c_{2,\mathbf{k}})\left(j^c_{2,1}A_{\mathrm{THz}} - \sum_{\mathbf{q}} V_{\mathbf{k}-\mathbf{q}}p^c_{1,2,\mathbf{q}}\right) \\
&\quad + i\hbar\frac{\partial}{\partial t}p^c_{1,2,\mathbf{k}}\bigg|_{\mathrm{scatt}}. \qquad \text{(C.12)}
\end{aligned}
$$

D. Simple solution for the total current density explaining Fano signatures

For a simple case one can solve the above equations analytically [115]. We assume an incoherent carrier distribution in the first conduction band $c1$ and $f^c_{2,\mathbf{k}} = 0$ before the THz pulse probes the $c1$-to-$c2$ transition. Moreover, we neglect renormalization effects and Coulomb interaction, take the two conduction bands to have the same dispersion $\tilde{\varepsilon}^c_{2,\mathbf{k}} - \tilde{\varepsilon}^c_{1,\mathbf{k}} = E_{12} = \text{const.}$ (and hence an identical effective mass m) and assume a δ-like THz probe pulse in the time domain, i.e. $A_{\mathrm{THz}}(\omega) = A_0 = \text{const.}$ is real. In addition, the scattering term is modeled by a phenomenological dephasing constant γ (see Eq. (4.16)). With these simplifications the equation of motion for the intersubband polarization reads (see Eq. (4.15) or Eq. (C.12)):

$$i\hbar\frac{\partial}{\partial t}p^c_{1,2,\mathbf{k}} = (\tilde{\varepsilon}^c_{2,\mathbf{k}} - \tilde{\varepsilon}^c_{1,\mathbf{k}})\, p^c_{1,2,\mathbf{k}} - i\gamma\, p^c_{1,2,\mathbf{k}} + f^c_{1,\mathbf{k}}\, j^c_{2,1} A_{\mathrm{THz}}. \tag{D.1}$$

This differential equation is solved via Fourier transformation $\frac{\partial}{\partial t} \rightarrow -i\omega$:

$$p^c_{1,2,\mathbf{k}}(\omega) = \frac{(j^c_{1,2})^* f^c_{1,\mathbf{k}} A_0}{E_{12} - \hbar\omega - i\gamma} \tag{D.2}$$

Inserting this equation in the definition of J_{THz} (Eq. 4.13) and adding the ponderomotive current density J_{A} (Eq. 4.9) leads to the following simple analytic expression for the total current density:

$$J_{\mathrm{tot}}(\omega) = \alpha n_{\mathrm{tot}} \frac{E_{12} - \hbar\omega}{(E_{12} - \hbar\omega)^2 + \gamma^2} + i \cdot \alpha n_{\mathrm{tot}} \frac{\gamma}{(E_{12} - \hbar\omega)^2 + \gamma^2} - \beta\omega^2_{\mathrm{PL}}. \tag{D.3}$$

We used the abbreviations $\alpha \propto |j_{1,2}|^2 A_0$ and $\beta \propto A_0$. The plasma frequency squared $\omega^2_{\mathrm{p}} = \sum_\lambda \frac{e^2 n_\lambda}{\epsilon_0 m_\lambda}$ is proportional to the total carrier density n_{tot}. The first two terms consisting of real and imaginary contributions originate from J_{THz}, the last term comes from J_{A}, which gives only a real-valued current as already mentioned (see Eq. (4.12)). Note that both current contributions depend in the same way linearly on the total carrier density n_{tot} in the conduction bands.
One notices that the real part of the first line, i.e. $\mathrm{Re}(\mathrm{J_{THz}})$, changes its sign at the intersubband resonance $\hbar\omega = E_{12}$. This asymmetry is responsible for the Fano-like line

shape in $|J_{\mathrm{tot}}(\omega)|$, because J_{THz} and J_{A} interfere either destructively or constructively, dependíng on whether the frequency is below or above the intersubband resonance. Note that the structure of J_{THz} with its Lorentzian terms is similar to that of the linear susceptibility (2.20) on page 10 (see also Fig. 2.4) since J_{THz} and $\chi^{(1)}$ are proportional and describe a discrete transition.

Bibliography

[1] J. Faist, F. Capasso, D. L. Sivco, C. Sirtori, A. L. Hutchinson, and A. Y. Cho, "Quantum cascade laser," Science **264**, 553 (1994).

[2] B. Ferguson and X.-C. Zhang, "Materials for terahertz science and technology," Nature Mater. **1**, 26 (2002).

[3] H. Schneider and H. C. Liu, "Quantum well infrared photodetectors: physics and applications," in *Springer Series in Optical Sciences* (Springer, Heidelberg, 2006), Vol. 126.

[4] P. L. Gourley, "Microstructured semiconductor lasers for high-speed information processing," Nature **371**, 571 (1994).

[5] S. Nakamura, T. Mukai, and M. Senoh, "Candela-class high-brightness InGaN/AlGaN double-heterostructure blue-light-emitting diodes," Appl. Phys. Lett. **64**, 1687 (1994).

[6] Y. Arakawa and H. Sakaki, "Multidimensional quantum well laser and temperature dependence of its threshold current," Appl. Phys. Lett. **40**, 939 (1982).

[7] R. Dingle, W. Wiegmann, and C. H. Henry, "Quantum states iof confined carriers in very thin $Al_xGa_{1-x}As$-GaAs-$Al_xGa_{1-x}As$ heterostructures," Phys. Rev. Lett. **33**, 827 (1974).

[8] E. A. Zibik, T. Grange, B. A. Carpenter, N. E. Porter, R. Ferreira, G. Bastard, D. Stehr, S. Winnerl, M. Helm, H. Y. Liu, M. S. Skolnick, and L. R. Wilson, "Long lifetimes of quantum-dot intersublevel transitions in the terahertz range," Nature Mater. **8**, 803 (2009).

[9] R. A. Kaindl, M. A. Carnahan, D. Hägele, R. Lövenich, and D. S. Chemla, "Ultrafast terahertz probes of transient conducting and insulating phases in an electron-hole gas," Nature **423**, 734 (2003).

[10] K. Kishino, A. Kikuchi, H. Kanazawa, and T. Tachibana, "Intersubband transition in $(GaN)_m/(AlN)_n$ superlattices in the wavelength range from 1.08 μm to 1.61 μm," Appl. Phys. Lett **81**, 1234 (2002).

[11] M. Helm, F. M. Peeters, F. DeRosa, E. Colas, J. P. Harbison, and L. T. Florez, "Far-infrared spectroscopy of minibands and confined donors in $GaAs/Al_xGa_{1-x}As$ superlattices," Phys. Rev. B **43**, 13 983 (1991).

[12] D. Mittleman (ed.), *Sensing with terahertz radiation* (Springer, Berlin, 2003).

[13] M. Tonouchi, "Cutting-edge terahertz technology," Nature Photon. **1**, 97 (2007).

[14] D. H. Auston, K. P. Cheung, and P. R. Smith, "Picosecond photoconducting Hertzian dipoles," Appl. Phys. Lett. **45**, 284 (1984).

[15] R. Huber, A. Brodschelm, F. Tauser, and A. Leitenstorfer, "Generation and field-resolved detection of femtosecond electromagnetic pulses tunable up to 41 THz," Appl. Phys. Lett. **76**, 3191 (2000).

[16] B. N. Murdin, "Far-infrared free-electron lasers and their applications," Contemp. Phys. **50**, 391 (2009).

[17] L. C. West and S. J. Eglash, "First observation of an extremely large-dipole infrared transition within the conduction band of a GaAs quantum well," Appl. Phys. Lett. **46**, 1156 (1985).

[18] J. R. Danielson, Y.-S. Lee, J. P. Prineas, J. T. Steiner, M. Kira, and S. W. Koch, "Interaction of strong single-cycle terahertz pulses with semiconductor quantum wells," Phys. Rev. Lett. **99**, 237 401 (2007).

[19] S. Leinß, T. Kampfrath, K. v. Volkmann, M. Wolf, J. T. Steiner, M. Kira, S. W. Koch, A. Leitenstorfer, and R. Huber, "Terahertz coherent control of optically dark para excitons in Cu_2O," Phys. Rev. Lett. **101**, 246 401 (2008).

[20] J. Kono, M. Y. Su, T. Inoshita, T. Noda, M. S. Sherwin, S. J. Allen, and H. Sakaki, "Resonant terahertz optical sideband generation from confined magnetoexcitons," Phys. Rev. Lett. **79**, 1758 (1997).

[21] S. G. Carter, V. Ciulin, M. Hanson, A. S. Huntington, C. S. Wang, A. C. Gossard, L. A. Coldren, and M. S. Sherwin, "Terahertz-optical mixing in undoped and doped GaAs quantum wells: From excitonic to electronic intersubband transitions," Phys. Rev. B **72**, 155 309 (2005).

[22] S. H. Autler and C. H. Townes, "Stark effect in rapidly varying fields," Phys. Rev. **100**, 703 (1955).

[23] J. H. Davies, *The physics of low-dimensional semiconductors* (Cambridge University Press, Cambridge, 1998).

[24] M. Helm, "The basic physics of intersubband transitions," in *Semiconductors and semimetals*, H. C. Liu and F. Capasso, eds. (Academic Press, San Diego, 2000), Vol. 62, chap. 1, pp. 1–99.

[25] J. Faist, C. Sirtori, F. Capasso, L. Pfeiffer, and K. W. West, "Phonon limited intersubband lifetimes and linewidths in a two-dimensional electron gas," Appl. Phys. Lett. **64**, 872 (1993).

[26] K. L. Vodopyanov, V. Chazapis, C. C. Phillips, B. Sung, and J. S. Harris, "Intersubband absorption saturation study of narrow III-V multiple quantum wells in the $\lambda = 2.8 - 9$ μm spectral range," Semicond. Sci. Technol. **12**, 708 (1997).

[27] Y. R. Shen, *The principles of nonlinear optics* (John Wiley & Sons, Inc., Hoboken, New Jersey, 2003).

[28] R. Boyd, *Nonlinear optics* (Academic Press, New York, 1992).

[29] V. G. Dmitriev, G. G. Gurzadyan, and D. N. Nikogosyan, *Handbook of nonlinear optical crystals* (Springer, Berlin, 1999).

[30] C. Kübler, R. Huber, S. Tübel, and A. Leitenstorfer, "Ultrabroadband detection of multi-terahertz field transients with GaSe electro-optic sensors: Approaching the near infrared," Appl. Phys. Lett. **85**, 3360 (2004).

[31] C. Jung, B. K. Rhee, and D. Kim, "Simple method for determining the crystalline axes of nonlinear uniaxial crystal with second-harmonic generation," Appl. Opt. **39**, 5142 (2000).

[32] M. Born and E. Wolf, *Principles of optics* (Pergamon Press, Oxford, 1975).

[33] K. L. Vodopyanov and L. A. Kulevskii, "New dispersion relationships for GaSe in the 0.65-18 μm spectral region," Opt. Commun. **118**, 375 (1995).

[34] S. G. Carter, J. Černe, and M. S. Sherwin, "Optical response of semiconductor nanostructures in terahertz fields generated by electrostatic free-electon lasers," in *Terahertz spectroscopy: Principles and applications*, S. L. Dexheimer, ed. (CRC Press Tayler & Francis Group, 2008), Vol. 131, chap. 6.

[35] G. Gallot, J. Zhang, R. W. McGowan, T.-I. Jeon, and D. Grischkowsky, "Measurements of the THz absorption and dispersion of ZnTe and their relevance to the electro-optic detection of THz radiation," Appl. Phys. Lett. **74**, 3450 (1999).

[36] L. Ho, M. Pepper, and P. Taday, "Terahertz spectroscopy: signatures and fingerprints," Nature Photon. **2**, 541 (2008).

[37] B. C. Smith, *Fundamentals of Fourier Transform Infrared Spectroscopy* (CRC Press, Boca Raton, Florida, 1996), 4th edn.

[38] A. Dreyhaupt, S. Winnerl, T. Dekorsy, and M. Helm, "High-intensity terahertz radiation from a microstructured large-area photoconductor," Appl. Phys. Lett. **86**, 121 114 (2005).

[39] A. Dreyhaupt, S. Winnerl, M. Helm, and T. Dekorsy, "Optimum excitation conditions for the generation of high-electric-field terahertz radiation from an oscillator-driven photoconductive device," Opt. Lett. **31**, 1546 (2006).

[40] F. Peter, S. Winnerl, S. Nitsche, A. Dreyhaupt, H. Schneider, and M. Helm, "Coherent terahertz detection with a large-area photoconductive antenna," Appl. Phys. Lett. **91**, 081 109 (2007).

[41] Q. Wu and X.-C. Zhang, "Free-space electro-optic sampling of terahertz beams," Appl. Phys. Lett. **67**, 3523 (1995).

[42] Q. Wu and X.-C. Zhang, "Ultrafast electro-optic field sensors," Appl. Phys. Lett. **68**, 1604 (1996).

[43] S. Ehret and H. Schneider, "Generation of subpicosecond infrared pulses tunable between 5.2 μm and 18 μm at a repetition rate of 76 MHz," Appl. Phys. B **66**, 27 (1998).

[44] A. Sell, A. Leitenstorfer, and R. Huber, "Phase-locked generation and field-resolved detection of widely tunable terahertz pulses with amplitudes exceeding 100 MV/cm," Opt. Lett. **33**, 2767 (2008).

[45] A. Bonvalet, M. Joffre, J.-L. Martin, and A. Migus, "Generation of ultrabroadband femtosecond pulses in the mid-infrared by optical rectification of 15 fs light pulses at 100 MHz repetition rate," Appl. Phys. Lett. **67**, 2907 (1995).

[46] R. A. Kaindl, D. C. Smith, M. Joschko, M. P. Hasselbeck, M. Woerner, and T. Elsaesser, "Femtosecond infrared pulses tunable from 9 to 18 μm at an 88-MHz repetition rate," Opt. Lett. **23**, 861 (1998).

[47] R. A. Kaindl, F. Eickemeyer, M. Woerner, and T. Elsaesser, "Broadband phase-matched difference frequency mixing of femtosecond pulses in GaSe: Experiment and theory," Appl. Phys. Lett. **75**, 1060 (1999).

[48] T. Zentgraf, R. Huber, N. C. Nielsen, D. S. Chemla, and R. A. Kaindl, "Ultrabroadband 50-130 THz pulses generated via phase-matched difference frequency mixing in $LiIO_3$," Opt. Express **15**, 5775 (2007).

[49] K. Liu, J. Xu, and X.-C. Zhang, "GaSe crystals for broadband terahertz wave detection," Appl. Phys. Lett. **85**, 863 (2004).

[50] B. S. Williams, "Terahertz quantum cascade lasers," Nature Photon. **1**, 517 (2007).

[51] D. A. G. Deacon, L. R. Elias, J. M. J. Madey, G. J. Ramian, H. A. Schwettman, and T. I. Smith, "First operation of a free-electron laser," Phys. Rev. Lett. **38**, 892 (1977).

[52] P. G. O'Shea and H. P. Freund, "Free-electron lasers: status and applications," Science **292**, 1853 (2001).

[53] M. Wagner, *Erzeugung, Charakterisierung und Anwendung ultrakurzer THz-Pulse*, Master's thesis, University of Konstanz (2006).

[54] D. Stehr, *Infrared studies of impurity states and ultrafast carrier dynamics in semiconductor quantum structures*, Ph.D. thesis, Forschungszentrum Dresden-Rossendorf and Technical University Dresden (2007).

[55] B. Schenkel, J. Biegert, U. Keller, C. Vozzi, M. Nisoli, G. Sansone, S. Stagira, S. D. Silvestri, and O. Svelto, "Generation of 3.8-fs pulses from adaptive compression of a cascaded hollow fiber supercontinuum," Opt. Lett. **28**, 1987 (2003).

[56] R. M. Hoff and J. C. Irwin, "Resonant Raman scattering in GaSe," Phys. Rev. B **10**, 3464 (1974).

[57] W. Shi, Y. J. Ding, N. Fernelius, and K. Vodopyanov, "Efficient, tunable and coherent 0.18-5.27-THz source based on GaSe crystal," Opt. Lett. **27**, 1454 (2002).

[58] F. Eickemeyer, *Ultrafast dynamics of coherent intersubband polarizations in quantum wells and quantum cascade laser structures*, Ph.D. thesis, Humboldt-University Berlin (2002).

[59] M. Joffre, A. Bonvalet, A. Migus, and J.-L. Martin, "Femtosecond diffracting Fourier-transform infrared interferometer," Opt. Lett. **21**, 964 (1996).

[60] A. Bonvalet, J. Nagle, V. Berger, A. Migus, J.-L. Martin, and M. Joffre, "Femtosecond infrared emission resulting from coherent charge oscillations in quantum Wells," Phys. Rev. Lett. **76**, 4392 (1996).

[61] J. N. Heyman, R. Kersting, and K. Unterrainer, "Time-domain measurement of intersubband oscillations in a quantum well," Appl. Phys. Lett. **72**, 644 (1998).

[62] A. Nahata, D. H. Auston, T. F. Heinz, and C. Wu, "Coherent detection of freely propagating terahertz radiation by electro-optic sampling," Appl. Phys. Lett. **68**, 150 (1995).

[63] A. Nahata, A. S. Weling, and T. F. Heinz, "A wideband coherent terahertz spectroscopy system using optical rectification and electro-optic sampling," Appl. Phys. Lett. **69**, 2321 (1996).

[64] Q. Wu and X.-C. Zhang, "7 terahertz broadband GaP electro-optic sensor," Appl. Phys. Lett. **70**, 1784 (1997).

[65] C. Winnewisser, P. U. Jepsen, M. Schall, V. Schyja, and H. Helm, "Electro-optic detection of THz radiation in $LiTaO_3$, $LiNbO_3$, and ZnTe," Appl. Phys. Lett. **70**, 3069 (1997).

[66] P. C. M. Planken, H.-K. Nienhuys, H. J. Bakker, and T. Wenckebach, "Measurement and calculation of the orientation dependence of terahertz pulse detection in ZnTe," J. Opt. Soc. Am. B **18**, 313 (2001).

[67] A. Leitenstorfer, S. Hunsche, J. Shah, M. C. Nuss, and W. H. Knox, "Detectors and sources for ultrabroadband electro-optic sampling: Experiment and theory," Appl. Phys. Lett. **74**, 1516 (1999).

[68] C. Kübler, R. Huber, and A. Leitenstorfer, "Ultrabroadband terahertz pulses: generation and field-resolved detection," Semicond. Sci. Technol. **20**, S128 (2005).

[69] `http://www.fzd.de/db/Cms?pNid=471`, Last checked: 28th October 2009.

[70] D. Stehr, M. Wagner, H. Schneider, M. Helm, A. M. Andrews, T. Roch, and G. Strasser, "Two-color pump-probe studies of intraminiband relaxation in doped GaAs/AlGaAs superlattices," Appl. Phys. Lett. **92**, 051 104 (2008).

[71] C. A. Brau, *Free-electron lasers* (Academic Press, Boston, 1990).

[72] K. Wille, *Physik der Teilchenbeschleuniger und Synchrotronstrahlungsquellen* (B. G. Teubner, Stuttgart, 1992).

[73] P. W. Milonni and J. H. Eberly, *Lasers* (John Wiley & Sons, Inc., New York, 1988).

[74] P. Michel, F. Gabriel, E. Grosse, P. Evtushenko, T. Dekorsy, M. Krenz, M. Helm, U. Lehnert, W. Seidel, R. Wünsch, D. Wohlfarth, and A. Wolf, "First lasing of the ELBE MID-IR FEL," in *Proceedings of the 26th International FEL Conference Trieste* (2004).
http://accelconf.web.cern.ch/accelconf/f04/papers/MOAIS04/MOAIS04.pdf

[75] P. Evtushenko, *Electron beam diagnostics at the ELBE free-electron laser*, Ph.D. thesis, Forschungszentrum Dresden-Rossendorf and Technical University Dresden (2004).

[76] G. Margaritondo, *Elements of synchrotron light* (Oxford University Press, Oxford, 2002).

[77] D. A. Jaroszynski, D. Oepts, A. F. G. van der Meer, P. W. van Amersfoort, and W. B. Colson, "Consequences of short electron-beam pulses in the FELIX project," Nucl. Instrum. & Methods Phys. Res. A **296**, 480 (1990).

[78] D. A. Jaroszynski, R. J. Bakker, A. F. G. van der Meer, D. Oepts, and P. W. van Amersfoort, "Experimental observation of limit-cycle oscillations in a short-pulse free-electron laser," Phys. Rev. Lett. **70**, 3412 (1993).

[79] G. M. H. Knippels, *The short-pulse free-electron laser: manipulation of the gain medium*, Ph.D. thesis, Vrije Universiteit Amsterdam (1996).

[80] G. M. H. Knippels, A. F. G. van der Meer, R. F. X. A. M. Mols, D. Oepts, and P. W. van Amersfoort, "Formation of multiple subpulses in a free-electron laser operating in the limit-cycle mode," Phys. Rev. E **53**, 2778 (1996).

[81] G. M. H. Knippels, X. Yan, A. M. MacLeod, W. A. Gillespie, M. Yasumoto, D. Oepts, and A. F. G. van der Meer, "Generation and complete electric-field characterization of intense ultrashort tunable far-infrared laser pulses," Phys. Rev. Lett. **83**, 1578 (1999).

[82] A. M. MacLeod, X. Yan, W. A. Gillespie, G. M. H. Knippels, D. Oepts, A. F. G. van der Meer, C. W. Rella, T. I. Smith, and H. A. Schwettman, "Formation of low time-bandwidth product, single-sided exponential optical pulses in free-electron laser oscillators," Phys. Rev. E **62**, 4216 (2000).

[83] `http://www.physik.uni-kl.de/thz-stand-off-detection.html`, Last checked: 4th November 2009.

[84] S. Wohnsiedler, M. Theuer, M. Herrmann, S. Islam, J. Jonuscheit, R. Beigang, and F. Hase, "Simulation and experiment of terahertz stand-off detection," Proc. SPIE **7215**, 72 150H (2009).

[85] `http://jp.hamamatsu.com/resources/products/sys/pdf/eng/e_streakh.pdf`, Last checked: 28th October 2009.

[86] Private communication with Stephan Schartner, December 2007 - January 2008, Center of Micro- and Nanostructures, TU Vienna, Vienna, Austria.

[87] R. Kersting, R. Bratschitsch, G. Strasser, K. Unterrainer, and J. N. Heyman, "Sampling a terahertz dipole transition with subcycle time resolution," Opt. Lett. **25**, 272 (2000).

[88] T. Müller, W. Parz, G. Strasser, and K. Unterrainer, "Influence of carrier-carrier interaction on time-dependent intersubband absorption in a semiconductor quantum well," Phys. Rev. B **70**, 155 324 (2004).

[89] C. W. Luo, K. Reimann, M. Woerner, T. Elsaesser, R. Hey, and K. H. Ploog, "Phase-resolved nonlinear response of a two-dimensional electron gas under femtosecond intersubband excitation," Phys. Rev. Lett. **92**, 047 402 (2004).

[90] R. H. M. Groeneveld and D. Grischkowsky, "Picosecond time-resolved far-infrared experiments on carriers and excitons in GaAs-AlGaAs multiple quantum wells," J. Opt. Soc. Am. B **11**, 2502 (1994).

[91] J. Černe, J. Kono, M. S. Sherwin, M. Sundaram, A. C. Gossard, and G. E. W. Bauer, "Terahertz dynamics of excitons in GaAs/AlGaAs quantum Wells," Phys. Rev. Lett. **77**, 1131 (1996).

[92] R. Huber, F. Tauser, A. Brodschelm, M. Bichler, G. Abstreiter, and A. Leitenstorfer, "How many-particle interactions develop after ultrafast excitation of an electron-hole plasma," Nature **414**, 286 (2001).

[93] I. Galbraith, R. Chari, S. Pellegrini, P. J. Phillips, C. J. Dent, A. F. G. van der Meer, D. G. Clarke, A. K. Kar, G. S. Buller, C. R. Pidgeon, B. N. Murdin, J. Allam, and G. Strasser, "Excitonic signatures in the photoluminescence and terahertz absorption of a GaAs/$Al_xGa_{1-x}As$ multiple quantum well," Phys. Rev. B **71**, 073 302 (2005).

[94] B. E. Cole, J. B. Williams, B. T. King, M. S. Sherwin, and C. R. Stanley, "Coherent manipulation of semiconductor quantum bits with terahertz radiation," Nature **410**, 60 (2001).

[95] J. F. Dynes, M. D. Frogley, M. Beck, J. Faist, and C. C. Phillips, "Ac Stark splitting and quantum interference with intersubband transitions in quantum Wells," Phys. Rev. Lett. **94**, 157 403 (2005).

[96] K. B. Nordstrom, K. Johnsen, S. J. Allen, A.-P. Jauho, B. Birnir, J. Kono, T. Noda, H. Akiyama, and H. Sakaki, "Excitonic dynamical Franz-Keldysh effect," Phys. Rev. Lett. **81**, 457 (1998).

[97] A. H. Chin, J. M. Bakker, and J. Kono, "Ultrafast electroabsorption at the transition between classical and quantum response," Phys. Rev. Lett. **85**, 3293 (2000).

[98] J. B. Krieger and G. J. Iafrate, "Time evolution of Bloch electrons in a homogeneous electric field," Phys. Rev. B **33**, 5494 (1986).

[99] F. Bloch, "Über die Quantenmechanik der Elektronen in Kristallgittern," Z. Phys. **52**, 555 (1929).

[100] U. Fano, "Effects of configuration interaction on intensities and phase shifts," Phys. Rev. **124**, 1866 (1961).

[101] J. Faist, C. Sirtori, F. Capasso, S.-N. G. Chu, L. N. Pfeiffer, and K. W. West, "Tunable Fano interference in intersubband absorption," Opt. Lett. **21**, 985 (1996).

[102] J. Faist, F. Capasso, C. Sirtori, K. W. West, and L. N. Pfeiffer, "Controlling the sign of quantum interference by tunneling from quantum wells," Nature **390**, 589 (1997).

[103] S. Bar-Ad, P. Kner, M. V. Marquezini, S. Mukamel, and D. S. Chemla, "Quantum confined Fano interference," Phys. Rev. Lett. **78**, 1363 (1997).

[104] H. Schmidt, K. L. Campman, A. C. Gossard, and A. Imamoğlu, "Tunneling induced transparency: Fano interference in intersubband transitions," Appl. Phys. Lett. **70**, 3455 (1997).

[105] C. P. Holfeld, F. Löser, M. Sudzius, K. Leo, D. M. Whittaker, and K. Köhler, "Fano resonances in semiconductor superlattices," Phys. Rev. Lett. **81**, 874 (1998).

[106] H. C. Liu, C. Y. Song, Z. R. Wasilewski, J. A. Gupta, and M. Buchanan, "Fano resonance mediated by intersubband-phonon coupling," Appl. Phys. Lett. **91**, 131 121 (2007).

[107] M. Kroner, A. O. Govorov, S. Remi, B. Biedermann, S. Seidl, A. Badolato, P. M. Petroff, W. Zhang, R. Barbour, B. D. Gerardot, R. J. Warburton, and K. Karrai, "The nonlinear Fano effect," Nature **451**, 311 (2008).

[108] `http://www.diamond-materials.de/downloads/cvd_diamond_booklet.pdf`, Last checked: 28th October 2009.

[109] W. Cochran, S. J. Fray, F. A. Johnson, J. E. Quarrington, and N. Williams, "Lattice absorption in gallium arsenide," J. Appl. Phys. **32**, 2102 (1961).

[110] P. Y. Yu and M. Cardona, *Fundamentals of semiconductors* (Springer-Verlag, Berlin, 1999).

[111] R. A. Kaindl, S. Lutgen, M. Woerner, T. Elsaesser, B. Nottelmann, V. M. Axt, T. Kuhn, A. Hase, and H. Künzel, "Ultrafast dephasing of coherent intersubband polarizations in a quasi-two-dimensional electron plasma," Phys. Rev. Lett. **80**, 3575 (1998).

[112] R. A. Kaindl, K. Reimann, M. Woerner, T. Elsaesser, R. Hey, and K. H. Ploog, "Homogeneous broadening and excitation-induced dephasing of intersubband transitions in a quasi-two-dimensional electron gas," Phys. Rev. B **63**, 161 308 (2001).

[113] S. Lutgen, R. A. Kaindl, M. Woerner, T. Elsaesser, A. Hase, and H. Künzel, "Nonlinear intersubband absorption of a hot quasi-two-dimensional electron plasma studied by femtosecond infrared spectroscopy," Phys. Rev. B **54**, R17 343 (1996).

[114] P. C. M. Planken, M. C. Nuss, I. Brener, K. W. Goossen, M. S. C. Luo, S. L. Chuang, and L. Pfeiffer, "Terahertz emission in single quantum wells after coherent optical excitation of light hole and heavy hole excitons," Phys. Rev. Lett. **69**, 3800 (1992).

[115] Private communication with Daniel Golde, 2007 - 2009, Department of Physics and Materials Sciences Center, Philipps-University Marburg, Marburg, Germany.

[116] F. Jahnke, M. Kira, and S. W. Koch, "Linear and nonlinear optical properties of excitons in semiconductor quantum wells and microcavities," Z. Phys. B **104**, 559 (1997).

[117] M. Kira and S. W. Koch, "Many-body correlations and excitonic effects in semiconductor spectroscopy," Prog. Quantum Electron. **30**, 155–296 (2006).

[118] M. Kira, W. Hoyer, and S. W. Koch, "Microscopic theory of the semiconductor terahertz response," phys. stat. sol. (b) **238**, 443–450 (2003).

[119] J. T. Steiner, M. Kira, and S. W. Koch, "Optical nonlinearities and Rabi flopping of an exciton population in a semicondctor interacting with strong terahertz fields," Phys. Rev. B **77**, 165 308 (2008).

[120] M. Kira, F. Jahnke, W. Hoyer, and S. W. Koch, "Quantum theory of spontaneous emission and coherent effects in semiconductor microstructures," Prog. Quantum Electron. **23**, 189–279 (1999).

[121] H. Haug and S. W. Koch, *Quantum theory of the optical and electronic properties of semiconductors* (World Scientific, Singapore, 2004), 4th edn.

[122] M. Balkanski and R. F. Wallis, *Semiconductor physics and applications* (Oxford University Press, New York, 2000).

[123] M. Lindberg and S. W. Koch, "Effective Bloch equations for semiconductors," Phys. Rev. B **38**, 3342 (1988).

[124] M. Olszakier, E. Ehrenfreund, E. Cohen, J. Bajaj, and G. J. Sullivan, "Photoinduced intersubband absorption in undoped multi-quantum-well structures," Phys. Rev. Lett. **62**, 2997 (1989).

[125] C. Delalande, G. Bastard, J. Orgonasi, J. A. Brum, H. W. Liu, M. Voos, G. Weimann, and W. Schlapp, "Many-body effects in a modulation-doped semiconductor quantum well," Phys. Rev. Lett. **59**, 2690 (1987).

[126] J. Černe, J. Kono, T. Inoshita, M. Sherwin, M. Sundaram, and A. C. Gossard, "Near-infrared sideband generation induced by intense far-infrared radiation in GaAs quantum wells," Appl. Phys. Lett. **70**, 3543 (1997).

[127] T. Inoshita, J. Kono, and H. Sakaki, "Theory of terahertz/near-infrared optical mixing in quantum wells in strong magnetic fields," Phys. Rev. B **57**, 4604 (1998).

[128] T. Inoshita and H. Sakaki, "Mixing of terahertz and near-infrared radiation in quantum wells in strong magnetic fields," Physica B **249**, 534 (1998).

[129] C. Phillips, M. Y. Su, M. S. Sherwin, J. Ko, and L. Coldren, "Generation of first-order optical sidebands in asymmetric coupled quantum wells," Appl. Phys. Lett. **75**, 2728 (1999).

[130] M. Y. Su, C. Phillips, J. Ko, L. Coldren, and M. S. Sherwin, "Odd terahertz optical sidebands from assymetric excitonic intersubband excitation," Physica B **272**, 438 (1999).

[131] S. G. Carter, V. Ciulin, M. S. Sherwin, M. Hanson, A. Huntington, L. A. Coldren, and A. C. Gossard, "Terahertz electro-optic wavelength conversion in GaAs quantum wells: Improved efficiency and room-temperature operation," Appl. Phys. Lett. **84**, 840 (2004).

[132] D. A. B. Miller, D. S. Chemla, T. C. Damen, A. C. Gossard, W. Wiegmann, T. H. Wood, and C. A. Burrus, "Band-edge electroabsorption in quantum well structures: The quantum-confined Stark effect," Phys. Rev. Lett. **53**, 2173 (1984).

[133] M. Y. Su, S. G. Carter, M. S. Sherwin, A. Huntington, and L. A. Coldren, "Voltage-controlled wavelength conversion by terahertz electro-optic modulation in double quantum wells," Appl. Phys. Lett. **81**, 1564 (2002).

[134] M. Y. Su, S. G. Carter, M. S. Sherwin, A. Huntington, and L. A. Coldren, "Strong-field terahertz optical mixing in excitons," Phys. Rev. B **67**, 125 307 (2003).

[135] V. Ciulin, S. G. Carter, M. S. Sherwin, A. Huntington, and L. A. Coldren, "Terahertz optical mixing in biased GaAs single quantum wells," Phys. Rev. B **70**, 115 312 (2004).

[136] D. Nesset, T. Kelly, and D. Marcenac, "All-optical wavelength conversion using SOA nonlinearities," IEEE Commun. Mag. **36**, 56 (1998).

[137] M. Asobe, O. Tadanaga, H. Miyazawa, Y. Nishida, and H. Suzuki, "Multiple quasi-phase-matched LiNbO3 wavelength converter with a continuously phase-modulated domain structure," Opt. Lett. **28**, 558 (2003).

[138] M. A. Zudov, J. Kono, A. P. Mitchell, and A. H. Chin, "Time-resolved, nonperturbative, and off-resonance generation of optical terahertz sidebands from bulk GaAs," Phys. Rev. B **64**, 121 204 (2001).

[139] K. Johnsen and A.-P. Jauho, "Linear optical absorption spectra of mesoscopic structures in intense THz fields: Free-particle properties," Phys. Rev. B **57**, 8860 (1998).

[140] K. Johnsen and A.-P. Jauho, "Quasienergy spectroscopy of excitons," Phys. Rev. Lett. **83**, 1207 (1999).

[141] T. Fromherz, "Floquet states and intersubband absorption in strongly driven double quantum wells," Phys. Rev. B **56**, 4772 (1997).

[142] A. V. Maslov and D. S. Citrin, "Optical absorption and sideband generation in quantum wells driven by a terahertz electric field," Phys. Rev. B **62**, 16 686 (2000).

[143] S. S. Dhillon, C. Sirtori, S. Barbieri, A. de Rossi, M. Calligaro, H. E. Beere, and D. A. Ritchie, "THz sideband generation at telecom wavelengths in a GaAs-based quantum cascade laser," Appl. Phys. Lett. **87**, 071 101 (2005).

[144] S. S. Dhillon, C. Sirtori, J. Alton, S. Barbieri, A. de Rossi, H. E. Beere, and D. A. Ritchie, "Terahertz transfer onto a telecom optical carrier," Nature Photon. **1**, 411 (2007).

[145] http://www.lot-oriel.com/site/site_down/tt_opticalmaterials_dede01.pdf, Last checked: 28th October 2009.

[146] R. C. Miller, D. A. Kleinman, W. T. Tsang, and A. C. Gossard, "Observation of the excited level of excitons in GaAs quantum wells," Phys. Rev. B **24**, 1134 (1981).

[147] P. Dawson, K. J. Moore, G. Duggan, H. I. Ralph, and C. T. B. Foxon, "Unambiguous observation of the 2s state of the light- and heavy-hole excitons in GaAs-(AlGa)As multiple-quantum-well structures," Phys. Rev. B **34**, 6007 (1986).

[148] F. H. Pollak and M. Cardona, "Piezo-electroreflectance in Ge, GaAs and Si," Phys. Rev. **172**, 816 (1968).

[149] V. Negoita, D. W. Snoke, and K. Eberl, "Stretching quantum wells: A method for trapping free carriers in GaAs heterostructures," Appl. Phys. Lett. **75**, 2059 (1999).

[150] R. Huber, R. A. Kaindl, B. A. Schmid, and D. S. Chemla, "Broadband terahertz study of excitonic resonances in the high-density regime in GaAs/$Al_xGa_{1-x}As$ quantum wells," Phys. Rev. B **72**, 161 314 (2005).

[151] R. A. Kaindl, D. Hägele, M. A. Carnahan, and D. S. Chemla, "Transient terahertz spectroscopy of excitons and unbound carriers in quasi-two-dimensional electron-hole gas," Phys. Rev. B **79**, 045 320 (2009).

[152] J. Černe, A. G. Markelz, M. S. Sherwin, S. J. Allen, M. Sundaram, A. C. Gossard, P. C. van Son, and D. Bimberg, "Quenching of excitonic quantum-well photoluminescence by intense far-infrared radiation: Free-carrier heating," Phys. Rev. B **51**, 5253 (1995).

[153] S. Winnerl, W. Seiwerth, E. Schomburg, J. Grenzer, K. F. Renk, C. J. G. M. Langerak, A. F. G. van der Meer, D. G. Pavel'ev, Y. Koschurinov, A. A. Ignatov, B. Melzer, V. Ustinov, S. Ivanov, and P. S. Kop'ev, "Ultrafast detection and autocorrelation of picosecond THz radiation pulses with a GaAs/AlAs superlattice," Appl. Phys. Lett. **73**, 2983 (1998).

[154] S. Winnerl, "GaAs/AlAs superlattices for detection of terahertz radiation," Microelectronics Journal **31**, 389 (2000).

[155] A. F. Gibson, M. F. Kimmitt, and A. C. Walker, "Photon drag in Germanium," Appl. Phys. Lett. **17**, 75 (1970).

[156] S. Winnerl, E. Schomburg, J. Grenzer, H.-J. Regl, A. A. Ignatov, A. D. Semenov, K. F. Renk, D. G. Pavel'ev, Y. Koschurinov, B. Melzer, V. Ustinov, S. Ivanov, S. Schaposchnikov, and P. S. Kop'ev, "Quasistatic and dynamic interaction of high-frequency fields with miniband electrons in semiconductor superlattices," Phys. Rev. B **56**, 10 303 (1997).

[157] S. M. Quinlan, A. Nikroo, M. S. Sherwin, M. Sundaram, and A. C. Gossard, "Photoluminescence from $Al_xGa_{1-x}As$/GaAs quantum wells quenched by intense far-infrared radiation," Phys. Rev. B **45**, 9428 (1992).

[158] A. Arno, D. Ballarini, D. Sanvitto, E. Kozhemyakina, L. Viña, A. Lemaître, D. Bajoni, and J. Bloch, "Optically induced ultrafast quenching of the semiconductor quantum well luminescence," Appl. Phys. Lett. **92**, 061 912 (2008).

[159] L. Rota, P. Lugli, T. Elsaesser, and J. Shah, "Ultrafast thermalization of photoexcited carriers in polar semiconductors," Phys. Rev. B **47**, 4226 (1993).

[160] S. W. Koch, M. Kira, G. Khitrova, and H. M. Gibbs, "Semiconductor excitons in new light," Nature **5**, 523 (2006).

[161] G. Bastard, C. Delalande, M. H. Meynadier, P. M. Frijlink, and M. Voss, "Low-temperature exciton trapping on interface defects in semiconductor quantum wells," Phys. Rev. B **29**, 7042 (1984).

[162] K. Leo, W. W. Rühle, and K. Ploog, "Hot-carrier energy-loss rates in GaAs/$Al_xGa_{1-x}As$ quantum wells," Phys. Rev. B **38**, 1947 (1988).

[163] `http://www.ioffe.ru/SVA/NSM/Semicond/GaAs/index.html`, Last checked: 28th October 2009.

[164] C. Delalande, M. H. Meynadier, and M. Voos, "Effect of temperature on exciton trapping on interface defects in GaAs quantum wells," Phys. Rev. B **31**, 2497 (1985).

[165] A. Srivastava, R. Srivastava, J. Wang, and J. Kono, "Laser-induced above-band-gap transparency in GaAs," Phys. Rev. Lett. **93**, 157 401 (2004).

[166] A. Arno, M. D. Martin, L. Viña, A. I. Toropov, and K. S. Zhuravlev, "Interplay of exciton and electron-hole plasma recombination on the photoluminescence dynamics in bulk GaAs," Phys. Rev. B **73**, 035 205 (2006).

[167] J. S. Blakemore, "Semiconducting and other major properties of gallium arsenide," J. Appl. Phys. **53**, 123 (1982).

[168] F. Szmulowicz and G. J. Brown, "Calculation and photoresponse measurement of the bound-to-continuum infrared absorption in p-type GaAs/AlGaAs quantum wells," Phys. Rev. B **51**, 13 203 (1995).

[169] R. C. Miller, D. A. Kleinman, W. A. Nordland, and A. C. Gossard, "Luminescence studies of optically pumped quantum wells in GaAs-$Al_xGa_{1-x}As$ multilayer structures," Phys. Rev. B **22**, 863 (1980).

[170] H. Iwamura, T. Saku, and H. Okamoto, "Optical absorption of GaAs-AlGaAs superlattice under electric field," Jpn. J. Appl. Phys. **24**, 104 (1985).

[171] R. T. Collins, K. v. Klitzing, and K. Ploog, "Photocurrent spectroscopy of GaAs/$Al_xGa_{1-x}As$ quantum wells in an electric field," Phys. Rev. B **33**, 4378 (1986).

[172] Y.-C. Chang and J. N. Schulman, "Interband optical transitions in GaAs-$Ga_{1-x}Al_xAs$ and InAs-GaSb superlattices," Phys. Rev. B **31**, 2069 (1985).

[173] X. L. Huang, Y. G. Shin, E.-K. Suh, H. J. Lee, Y. G. Hwang, and Q. Huang, "Temperature dependent blue shift and broadening of intersubband absorption and photocurrent spectra in GaAs/$Al_{0.3}Ga_{0.7}As$ multiple quantum wells," J. Appl. Phys. **82**, 4394 (1997).

[174] E. E. Mendez, G. Bastard, L. L. Chang, L. Esaki, H. Morkoc, and R. Fischer, "Effect of an electric field on the luminescence of GaAs quantum wells," Phys. Rev. B **26**, 7101 (1982).

[175] D. A. B. Miller, D. S. Chemla, T. C. Damen, A. C. Gossard, W. Wiegmann, T. H. Wood, and C. A. Burrus, "Electric field dependence of optical absorption near the band gap of quantum-well structures," Phys. Rev. B **32**, 1043 (1985).

[176] R. Lewén, S. Irmscher, U. Westergren, L. Thylén, and U. Eriksson, "Segmented transmission-line electroabsorption modulators," J. Lightwave Technol. **22**, 172 (2004).

[177] W. Franz, "Einfluss eines elektrischen Feldes auf eine optische Absorptionskante," Z. Naturforsch. Teil A **13**, 484 (1958).

[178] L. V. Keldysh, "Influence of a strong electric field on the optical characteristics of non conducting crystals," Sov. Phys. JETP **34**, 788 (1958).

[179] A. P. Jauho and K. Johnsen, "Dynamical Franz-Keldysh effect," Phys. Rev. Lett. **76**, 4576 (1996).

[180] S. Hughes and D. S. Citrin, "Dynamic Franz-Keldysh effect: perturbative to nonperturbative regime," Opt. Lett. **25**, 493 (2000).

[181] C. J. Dent, B. N. Murdin, and I. Galbraith, "Phase and intensity dependence of the dynamical Franz-Keldysh effect," Phys. Rev. B **67**, 165 312 (2003).

[182] J. S. Bakos, "Ac Stark effect and multiphoton processes in atoms," Phys. Rep. **31**, 209 (1977).

[183] A. Mysyrowicz, D. Hulin, A. Antonetti, A. Migus, W. T. Masselink, and H. Morkoc, ""Dressed excitons" in a multiple quantum well structure: Evidence for an optical Stark effect with femtosecond response time," Phys. Rev. Lett. **56**, 2748 (1986).

[184] D. Fröhlich, R. Wille, W. Schlapp, and G. Weimann, "Optical quantum-confined Stark effect in GaAs quantum wells," Phys. Rev. Lett. **59**, 1748 (1987).

[185] G. B. Serapiglia, E. Paspalakis, C. Sirtori, K. L. Vodopyanov, and C. C. Phillips, "Laser-induced quantum coherence in a semiconductor quantum well," Phys. Rev. Lett. **84**, 1019 (2000).

[186] M. C. Phillips, H. Wang, I. Rumyantsev, N. H. Kwong, R. Takayama, and R. Binder, "Electromagnetically induced transparency in semiconductors via biexciton coherence," Phys. Rev. Lett. **91**, 183 602 (2003).

[187] M. D. Frogley, J. F. Dynes, M. Beck, J. Faist, and C. C. Phillips, "Gain without inversion in semiconductor nanostructures," Nature Mater. **5**, 175 (2006).

[188] A. Liu and C.-Z. Ning, "Exciton absorption in semiconductor quantum wells driven by a strong intersubband pump field," J. Opt. Soc. Am. B **17**, 433 (2000).

[189] A. V. Maslov and D. S. Citrin, "Optical absorption of THz-field-driven and dc-biased quantum wells," Phys. Rev. B **64**, 155 309 (2001).

[190] S. G. Carter, V. Birkedal, C. S. Wang, L. A. Coldren, A. V. Maslov, D. S. Citrin, and M. S. Sherwin, "Quantum coherence in an optical modulator," Science **310**, 651 (2005).

[191] S. G. Carter, *Terahertz electro-optic effects in (In)GaAs quantum wells*, Ph.D. thesis, University of California Santa Barbara (2004).

[192] X. Xu, B. Sun, P. R. Berman, D. G. Steel, A. S. Bracker, D. Gammon, and L. J. Sham, "Coherent optical spectroscopy of a strongly driven quantum dot," Science **317**, 929 (2007).

[193] M. Kroner, C. Lux, S. Seidl, A. W. Holleitner, K. Karrai, A. Badolato, P. M. Petroff, and R. J. Warburton, "Rabi splitting and ac-Stark shift of a charged exciton," Appl. Phys. Lett. **92**, 031 108 (2008).

[194] G. Jundt, L. Robledo, A. Högele, S. Fält, and A. Imamoglu, "Observation of dressed excitonic states in a single quantum dot," Phys. Rev. Lett. **100**, 177 401 (2008).

[195] A. D. Jameson, J. L. Tomaino, Y.-S. Lee, J. P. Prineas, J. T. Steiner, M. Kira, and S. W. Koch, "Transient optical response of quantum well excitons to intense narrowband terahertz pulses," Appl. Phys. Lett. **95**, 201 107 (2009).

[196] G. Bastard, *Wave mechanics applied to semiconductor heterostructures* (Halsted Press, New York, 1988).

Publications

Journals

1. D. Stehr, C. M. Morris, D. Talbayev, M. Wagner, H. C. Kim, A. J. Taylor, H. Schneider, P. M. Petroff, and M. S. Sherwin, "Ultrafast carrier capture in InGaAs quantum posts," Appl. Phys. Lett. (2009), in print

2. M. Wagner, H. Schneider, S. Winnerl, M. Helm, T. Roch, A. M. Andrews, S. Schartner, and G. Strasser, "Resonant enhancement of second order sideband generation for intra-excitonic transitions in GaAs/AlGaAs multiple quantum wells," Appl. Phys. Lett. **94**, 241105 (2009)

3. D. Golde, M. Wagner, D. Stehr, H. Schneider, M. Helm, A. M. Andrews, T. Roch, G. Strasser, M. Kira, and S.W. Koch, "Fano signatures in the intersubband terahertz response of optically excited semiconductor quantum wells," Phys. Rev. Lett. **102**, 127403 (2009)

4. D. Stehr, M. Wagner, H. Schneider, M. Helm, A. M. Andrews, T. Roch, and G. Strasser, "Two-color pump-probe studies of intraminiband relaxation in doped GaAs/AlGaAs superlattices", Appl. Phys. Lett. **92**, 051104 (2008)

5. A. Dreyhaupt, F. Peter, S. Winnerl, S. Nitsche, M. Wagner, H. Schneider, M. Helm, and K. Köhler, "Leistungsstarke Emitter und einfach handhabbare Detektoren für die Terahertz-Time-Domain-Spektroskopie," Technisches Messen **75**, 3 (2008)

6. S. Winnerl, F. Peter, S. Nitsche, A. Dreyhaupt, B. Zimmermann, M. Wagner, H. Schneider, M. Helm, and K. Köhler, "Generation and detection of THz radiation with scalable antennas based on GaAs substrates with different carrier lifetimes," IEEE Journal of Selected Topics in Quantum Electronics **14**, 449 (2008)

Refereed conference proceedings

1. M. Wagner, D. Golde, D. Stehr, H. Schneider, M. Helm, A. M. Andrews, T. Roch, G. Strasser, M. Kira, and S.W. Koch, "Fano profile in the intersubband terahertz response of photoexcited GaAs/AlGaAs quantum wells," Journal of Physics: Conference Series **193**, 012073 (2009)

2. D. Stehr, M. Wagner, H. Schneider, M. Helm, A. M. Andrews, T. Roch, and G. Strasser, "Two color pump-probe studies of intraminiband relaxation in doped

GaAs/AlGaAs superlattices," Proc. of SPIE **7214**, 72141N (2009)

3. W. Seidel, E. Cizmar, O. Drachenko, M. Helm, M. Justus, U. Lehnert, P. Michel, M. Ozerov, H. Schneider, R. Schurig, D. Stehr, M. Wagner, S. Winnerl, D. Wohlfarth, S. Zvyagin, S. C. Kehr, and L. M. Eng, "Three years of cw-operation at FELBE - experiences and applications," Proceeding of the 30th International Free Electron Laser Conference FEL 2008, 24th - 29th August 2008, Gyeongju, Korea (2008)

4. M. Wagner, D. Stehr, H. Schneider, M. Helm, A. M. Andrews, T. Roch, and G. Strasser, "Intraminiband Relaxation In Doped GaAs/AlGaAs Superlattices Studied By Two-Color Infrared Pump-Probe Experiments," 29th International Conference on the Physics of Semiconductors ICPS 2008, 27th July - 1st August 2008, Rio de Janeiro, Brazil, AIP Conference Proceedings (2008), in print

Acknowledgement

The research work described in this thesis has been carried out at the Forschungszentrum Dresden-Rossendorf in the semiconductor spectroscopy division.
Here, I would like to express my gratitude to those people who made this thesis possible (besides myself):

Many thanks go to my thesis supervisor Manfred Helm who showed large interest in my work and gave guidance and encouragement.
I'm grateful to Thomas Dekorsy for being my additional referee.
Many thanks also to Harald Schneider for fruitful discussions and support throughout the experiments. Besides, he always saw something positive in my strangest results.
I also like to thank our collaborators Maxwell Andrews, Tomas Roch, Stephan Schartner and Gottfried Strasser from the TU Vienna for growing and preparing our high-quality samples, as well as Daniel Golde and his supervisors Mackillo Kira and Stefan W. Koch from the Marburg University theory group for their theoretical support and patience.
I am very grateful to Stephan Winnerl whose experience and enthusiasm was of great value for me. His attitude also supports the friendly atmosphere of our division.
Also thanks to Dominik Stehr who is one of the most enthusiastic persons I got to know so far, and whose ideas were of some help in my thesis.
Special thanks goes to Wolfgang Seidel who is the good spirit of the FELBE facility with his profound knowledge about every screw holding together FELBE.
I am very grateful to Peter Michel and the whole FELBE team, especially to Rico Schurig.
Falk Peter, my fellow in misery, has also been a great help and support. I enjoyed very much discussions with him and also some off-work activities.
I am thankful to all my present and past colleagues I had the pleasure to work with, i.e. Jayeeta Bhattacharyya, Andreas Bollmann, Oleksiy Drachenko, Andre Dreyhaupt, Sven Friebel, Ralf Hubrich, Rainer Jacob (he probably has night shift now?), Oliver Kallauch, Sven Nitsche, Charlotte Pfau, Christiana Villas-Boas Tribuzy, Marlen Sellesk, Burkhard Zimmermann and Sabine Zybell for the enjoyable working atmosphere.
Uta Lucchesi, Joachim Wagner and Manja Kiebler did a great job with providing technical support. Sybille Kirch solved any administrative problems very effectively, thanks.
I could go on, for instance with thanking the Dussmann team for nourishing me with Saxonian potato soup, but the space is limited.
However, last but not least, I am very much indebted to my family and relatives who supported me throughout these endless years abroad in Dresden ;-).

Versicherung

Diese Arbeit entstand am Forschungszentrum Dresden-Rossendorf unter wissenschaftlicher Betreuung durch Prof. Dr. Manfred Helm, Professor im Institut für Angewandte Physik der Fakultät Mathematik und Naturwissenschaften der Technischen Universität Dresden.

Hiermit versichere ich, dass ich die vorliegende Arbeit ohne unzulässige Hilfe Dritter und ohne Benutzung anderer als der angegebenen Hilfsmittel angefertigt habe; die aus fremden Quellen direkt oder indirekt übernommenen Gedanken sind als solche kentlich gemacht. Die Arbeit wurde bisher weder im Inland noch im Ausland in gleicher oder ähnlicher Form einer anderen Prüfungsbehörde vorgelegt.

Ich erkenne die Promotionsordnung der Fakultät Mathematik und Naturwissenschaften der Technischen Universität Dresden in der aktuell gültigen Fassung vom 27.05.2009 an.

Dresden, den ..... 2009 Martin Wagner